Design and Electrochemical Performance of Sodium-Based Batteries

Qipeng Zhang

Dissertation submitted to the faculty of the Virginia Polytechnic Institute and State
University in partial fulfillment of the requirements for the degree of

Doctor of Philosophy
In
Mechanical Engineering

Rui Qiao, Chair
Zheng Li, Co-Chair
Alex Aning
Zhenhua Tian

11/22/2024
Blacksburg, Virginia

Keywords: Sodium metal battery, Sodium sulfur battery, Low concentration electrolyte,
Acoustic field, Mechanism and kinetics

Design and Electrochemical Performance of Sodium-Based Batteries

Qipeng Zhang

ABSTRACT

Low-cost, high-performance energy storage solutions are in great demand for applications such as vehicle electrification and electricity generation from renewable sources. Lithium-based batteries have emerged as strong contenders due to their high energy density and stability. However, their reliance on scarce lithium reserves and high production costs makes them impractical for many applications. Sodium-based batteries (SBBs) are gaining traction as a more affordable option, with costs of \$50 to \$100 per kWh and an abundant resource base. Despite these advantages, SBBs still face many obstacles, primarily due to limited research on sodium-based chemistries. Additionally, sodium-based batteries have inherent limitations, including lower energy capacity and reduced cycle life, which restrict their viability for long-term use. This thesis addresses several critical challenges faced by SBBs and explores new strategies for enhancing their performance and viability for large-scale applications.

First, a low-concentration, non-flammable electrolyte consisting of 0.3 M $NaPF_6$ in a mixed solvent was formulated and tested in SBBs. This electrolyte significantly improves the cyclability and performance of SBBs across a wide temperature range, with high-capacity retention at both elevated and sub-zero temperatures. Molecular simulations reveal that the improved ion-pairing underpins the exceptional performance. This development addresses major challenges in SBBs by offering a safer, more cost-effective solution for large-scale applications.

Second, sodium-sulfur (Na-S) batteries were explored to achieve high energy densities. An external acoustic field was implemented to enhance Na-S battery performance by inhibiting the shuttle effect and reducing dendrite growth, two key challenges in Na-S systems. This method offers a scalable, non-chemical solution to improve cycle life and efficiency, making Na-S batteries a more viable candidate for large-scale energy storage. This progress, along with the high theoretical capacity of Na-S batteries, helps address the limitations not resolved by the electrolyte engineering work of SBBs.

Third, the mechanisms of Na_2S_x ($x \leqslant 2$) precipitation in sodium-sulfur (Na-S) and sodium-oxygen-sulfur (Na/O_2-S) systems were investigated. The results reveal that higher-order sodium polysulfides display the lowest current density, indicating a stronger driving force is needed to initiate their reaction. In $Na/(O_2)$-S systems, the transition from high-order to low-order oxy-sulfur intermediates demands less energy compared to Na-S systems. The insights gained here help further optimize Na-S/$Na/(O_2)$-S batteries to enhance their performance and cycle life.

Together, the work in this dissertation addressed several critical needs in the development of SBBs and helped advance their commercialization.

Design and Electrochemical Performance of Sodium-Based Batteries

Qipeng Zhang

GENERAL AUDIENCE ABSTRACT

As the demand for affordable and efficient energy storage grows, especially to support electric vehicles and electricity generation from renewable sources, new types of batteries are needed. While lithium-based batteries are commonly used due to their high energy capacity, they rely on scarce and expensive lithium resources, making them impractical for large-scale applications like storing energy for electrical grids. This has led researchers to explore sodium-based batteries, which use sodium, a much more abundant and cost-effective element. However, sodium-based batteries still face challenges, such as lower energy capacity and shorter lifespan compared to their lithium counterparts.

This thesis focuses on improving sodium-based battery performance to make them a more viable option for large-scale energy storage. The first project introduces a new, safer, low-cost electrolyte that significantly enhances the performance of sodium-based batteries, even in extreme temperatures. This solution improves the battery's ability to retain its energy over multiple charging cycles, addressing some of the key issues in current sodium-based battery technology.

In the second project, the focus shifts to sodium-sulfur (Na-S) batteries, which offer the potential for higher energy storage due to sulfur's high capacity. To address common issues in Na-S batteries, such as the polysulfide shuttle effect and dendrite formation, a novel acoustic approach is explored. This method reduces the migration of polysulfides between the electrodes, which preserves capacity, and also suppresses the growth of dendrites on the sodium metal anode, improving both safety and battery lifespan. As a result, the efficiency and durability of Na-S batteries are significantly enhanced, bringing them closer to practical, large-scale applications.

Despite these advancements, some fundamental questions remain about how sodium polysulfides form and behave inside Na-S batteries. The third project focuses on understanding the precipitation and interaction of these compounds under different conditions. Gaining insight into these processes is essential for further enhancing battery performance and ensuring long-term reliability.

In conclusion, this thesis explores several innovative strategies to improve the design and performance of sodium-based batteries, which help make them more practical for large-scale energy storage applications and ultimately contribute to a more sustainable future.

Acknowledgements

I would like to express my deepest gratitude to Dr. Zheng Li for providing me with the invaluable opportunity to study, research, and work under his guidance. His unwavering support allowed me to pursue my research interests freely and develop my skills. I am also profoundly grateful to Prof. Rui Qiao, who showed exceptional understanding and kindness during challenging times and offered boundless academic support that motivated me to reach my goals. The encouragement and guidance from both Dr. Li and Prof. Qiao have been instrumental in helping me achieve all that I have accomplished.

My thanks also go to Dr. Alex Aning and Dr. Zhenhua Tian for serving on my committee. Their constructive feedback and insightful advice have been pivotal in refining my research and thesis.

I am deeply thankful to the staff of the Department of Mechanical Engineering, including Gail Coe, Miriam Snyder, Cathy Hill, and Johnny Underwood, for their support and assistance throughout my doctoral journey. I owe special gratitude to Gail Coe, who encouraged and comforted me during my lowest moments, offering emotional support and sharing her life experiences, which taught me invaluable lessons. I sincerely wish her good health and happiness every day. I would also like to thank Miriam Snyder for her steadfast support; her encouragement and thoughtful advice helped me navigate difficult times with resilience.

Furthermore, I am incredibly grateful to my friend Hao Li, who has supported me from the moment I first arrived in the United States and continued to help me navigate both my life and experiments throughout my PhD journey. I am also thankful to Teng Li, Jiali Li, Luyu Bo, Wenge Huang, Penghui Zhao, Shihui Chen, and Shijun Wei, who have been there for me in both life and research over the years. Meeting each of you has been one of the greatest fortunes of my life. In addition, I want to extend my thanks to the members of Dr. Li's and Prof. Qiao's research groups for their

support and assistance throughout my studies: Tairan Yang, Yunhao Xiao, Zihang Zhao and Xin Wang. Their help has been invaluable in many aspects of my work.

Finally, I want to express my deepest gratitude to my parents and my sister. Their unwavering love and support from beginning to end have been the foundation that has enabled me to reach this milestone.

Table of Contents

List of Figures

List of Tables

Chapter – 1 Introduction

1.1 Background and motivation

Sodium-based batteries have attracted significant attention as a sustainable and cost-effective alternative to lithium-based technologies, particularly for large-scale applications like grid storage and backup power [1-5]. These systems, which include both sodium metal and sodium-sulfur (Na-S) batteries, offer key advantages over lithium-based counterparts, particularly in terms of resource abundance and lower system costs [6-8]. Therefore, sodium-based batteries are an attractive option when cost considerations outweigh the need for high energy density [9-11].

Sodium-based batteries function in a manner similar to lithium-ion batteries, utilizing the transfer of sodium ions between the anode and cathode via an electrolyte during charging and discharging cycles as shown in **Figure 1.1** [12]. However, the larger ionic radius of sodium introduces specific challenges, especially in terms of electrolyte optimization [13-15]. Stable, efficient electrolytes are essential to enhancing the performance of sodium-based systems by ensuring high ionic conductivity and long-term chemical stability [16-19].

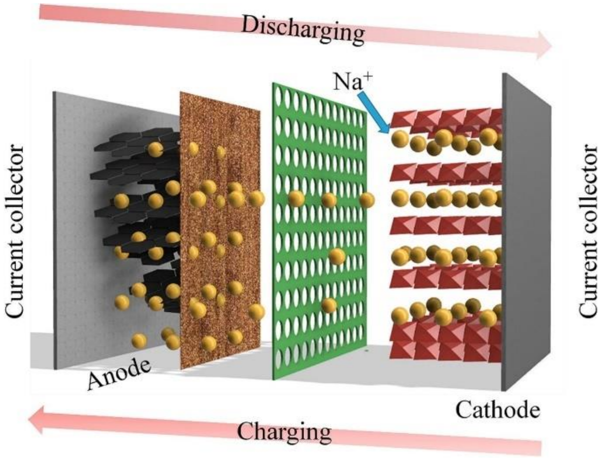

Figure 1.1 Operating mechanism of sodium-based batteries: sodium ion transport in electrolytes during charge-discharge cycles. Reproduced with permission from Ref. [13]. Copyright 2023 Elsevier.

Electrolyte stability directly influences the efficiency, safety, and lifespan of sodium-based batteries [20,21]. Sodium ions interact differently with solvents and other ions compared to the Li ions due to their larger size, often leading to reduced ionic conductivity and difficulties in forming a stable solid-electrolyte interphase (SEI) [22-24]. While various electrolyte formulations have been explored, including sodium salts like $NaPF_6$ and $NaClO_4$ in organic solvents, finding an optimized electrolyte remains a key challenge for sodium-based batteries [25-27].

While sodium-based batteries face limitations in energy density and cycle life compared to lithium-ion systems, Na-S batteries have emerged as a promising alternative, particularly for long-duration energy storage [28,29]. Na-S batteries offer higher theoretical energy density and benefit from the low cost and abundance of sulfur as a cathode material [30]. These features make sodium-sulfur batteries more attractive in large-scale energy storage applications, where cost and resource availability are critical factors [31].

High-temperature Na-S batteries (HT Na-S), operating above 300 °C, have shown potential for grid-scale storage due to their higher energy density and longer cycle life compared to room-temperature sodium-based systems (**Figure 1.2**). However, maintaining such high temperatures requires substantial energy input, which reduces overall efficiency. Additionally, prolonged exposure to heat can lead to material degradation, limiting the practical application of high-temperature Na-S batteries [32,33].

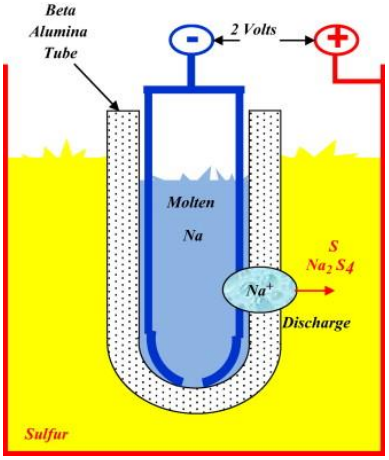

Figure 1.2 Schematic diagram of a high-temperature Na-S cell. Reproduced with permission from Ref. [33]. Copyright 2014 Elsevier.

To address these drawbacks, researchers have turned their focus to developing room-temperature sodium-sulfur batteries (RT Na-S). These systems aim to retain the high energy density and cost-effective nature of Na-S chemistry while eliminating the need for high operating temperatures [31]. RT Na-S batteries promise improved efficiency and reduced operational costs, making them more practical for many applications. However, despite these advantages, significant challenges such as the shuttle effect and dendrite formation remain barriers to their widespread use as presented in **Figure 1.3** [34,35].

The shuttle effect occurs when soluble sodium polysulfides generated during discharge migrate through the electrolyte and react with the sodium anode, leading to side reactions that degrade battery performance. This phenomenon not only reduces efficiency but also causes capacity fading, which significantly limits the battery's lifespan [36].

Dendrite formation is another major challenge. Needle-like dendrites can form on the sodium anode during charging, which can breach the separator and trigger internal short circuits, increasing the risk of safety issues like thermal runaway.

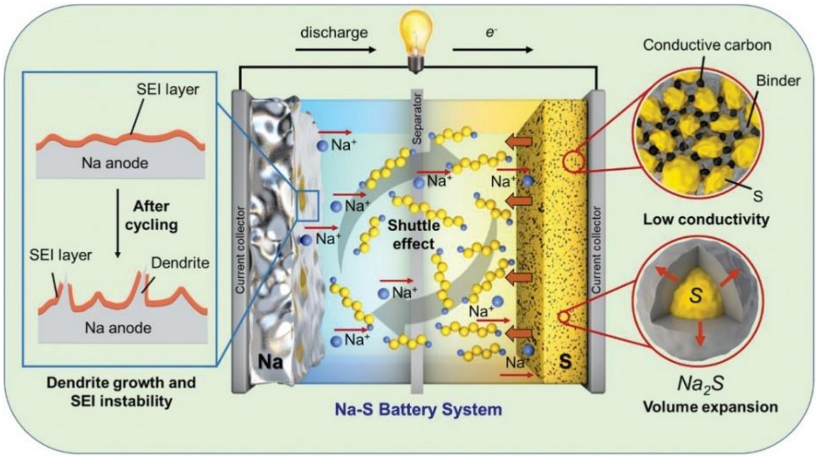

Figure 1.3 A diagram of a room-temperature sodium-sulfur cell that illustrates several critical challenges. It highlights the movement of polysulfides through the electrolyte, causing shuttling effects, while zoomed-in views reveal additional concerns. These include dendrite formation and unstable solid electrolyte interphases at the sodium anode, as well as the sulfur-based cathode's issues with volumetric changes and poor conductivity. Reproduced with permission from Ref. [35]. Copyright 2021 Wiley-VCH.

In summary, sodium-based batteries offer a sustainable and cost-effective alternative to lithium-ion technologies, especially for large-scale energy storage. However, challenges related to electrolyte stability and performance must be addressed to fully unlock their potential. Na-S batteries, while offering higher energy densities and cost benefits, are still constrained by technical issues such as the shuttle effect and dendrite formation. Addressing these challenges is critical for advancing sodium-based batteries for future energy storage applications.

1.2 Electrolytes for sodium-based batteries

The electrolyte plays a crucial role in sodium-based batteries, facilitating the movement of sodium ions between the anode and cathode throughout charge and discharge cycles [37-40]. In most systems, the electrolyte is a sodium salt dissolved in non-aqueous organic solvents. To ensure optimal battery performance, the electrolyte must meet several requirements:

1. ***Low internal resistance:*** High ionic conductivity is essential to minimize resistive heating and ensure efficient ion transport.
2. ***Chemical stability:*** The electrolyte must resist degradation, particularly in contact with highly reducing anodes, to maintain long-term performance.
3. ***Electrochemical stability:*** It should remain stable within the voltage range of the battery's anode and cathode, preventing side reactions.
4. ***Thermal properties:*** A low melting point and high boiling point ensure stability across a wide temperature range.
5. ***Safety and cost:*** The electrolyte should be non-toxic, safe, and cost-effective for large-scale applications.

Liquid electrolytes are generally favored due to their ease of transport through porous electrodes [41,42]. However, these batteries face challenges like dendrite formation, which can result in short circuits. Solid electrolytes, on the other hand, provide enhanced mechanical strength, helping to inhibit dendrite growth. Unfortunately, solid electrolytes often suffer from higher resistance and poor contact with electrodes, which can hinder ion transport [43].

To address these challenges, new formulations like super-high concentration electrolytes and ultralow concentration electrolytes are being explored. These systems are designed to enhance the stability, safety, and efficiency of sodium-based batteries, paving the way for more reliable large-scale energy storage solutions.

1.2.1 The evolution of electrolyte systems for sodium-based batteries

Electrolytes are vital for enabling ion movement while insulating the reactive cathode from direct electronic interaction with the reductive anode [44]. The future of battery innovation depends heavily on the development of advanced electrolyte systems. While solid-state electrolytes hold promise for next-generation batteries due to their ability to prevent issues like dendrite formation, liquid electrolytes still dominate, owing to their optimized interaction with electrode surfaces and minimized resistance at the electrode-electrolyte boundary [19,45,46].

Modern liquid electrolytes typically consist of salts dissolved in polar solvents, where ion dissociation is facilitated by solvation structures. These can occur in either aqueous or non-aqueous solutions. To achieve high-performance electrolytes, researchers must balance several key properties:

- Physically, an ideal electrolyte should maintain stability over a wide temperature range, exhibit low viscosity, support high ionic conductivity, and ensure thermal resilience.
- Chemically, the electrolyte must be easy to synthesize and remain inert toward both active and inactive battery components.
- Electrochemically, it needs a broad stability window, a stable and thin SEI, and compatibility with high-energy-density materials.

Historically, electrolyte research primarily focused on adjusting the composition of salts, solvents, or functional additives to improve stability and performance as demonstrated in **Figure 1.4a**.

However, attention has recently shifted toward exploring the concentration of electrolytes, breaking away from the “1 molarity (M) legacy,” where the ionic conductivity of non-aqueous systems was believed to peak around 1 M. Higher concentrations were largely overlooked due to their presumed diminishing returns. However, recent research has shown that optimizing electrolyte concentration can unlock new properties that greatly enhance battery performance.

A major breakthrough came in 1985 when McKinnon and Dahn discovered that highly concentrated solutions could prevent the co-intercalation of propylene carbonate with lithium ions into ZrS_2, which typically damaged the battery at lower concentrations [47]. This revelation challenged traditional electrolyte theories. By 1993, Angell and colleagues expanded on this idea by introducing the concept of polymer-in-salt electrolytes, where increasing salt concentrations beyond a certain threshold reversed the decline in ionic conductivity observed in more dilute solutions [48]. This opened new possibilities for concentrated electrolytes.

In the early 2000s, further advancements were made. Inaba and colleagues showed that highly concentrated electrolytes could stabilize the electrolyte-electrode interface without traditional additives [49]. By 2004, Chen and colleagues developed a room-temperature molten salt electrolyte by mixing lithium bis(trifluoromethanesulfonyl)imide (LiTFSI) with acetamide, demonstrating superior physicochemical properties that hinted at broader applications, particularly in lithium-ion batteries [50].

In 2010, Watanabe and co-workers introduced glyme-based super-concentrated electrolytes, which exhibited properties similar to room-temperature ionic liquids, with high ionic conductivity and low volatility [51]. This marked another major leap forward.

The most significant advancement came in 2013 when Hu and colleagues proposed the solvent-in-salt (SIS) electrolyte system, where the salt-to-solvent ratio exceeded 1.0 [52]. This novel system suppressed polysulfide solubility and lithium dendrite growth, making it particularly advantageous for lithium-sulfur batteries. Watanabe and co-researchers created an innovative SIS electrolyte using LiTFSI dissolved in TEGDME [53]. They discovered that when the molar ratio of salt to solvent reaches around 1:1, the electrolyte forms a structure akin to ionic liquids. This arrangement includes distinct $[Li(glyme)_1]^+$ complexes along with individual TFSI anions, which remain unassociated in the solution. Soavi et al. examined the impact of adjusting salt concentrations on the stability of intermediates and final compounds in lithium/oxygen batteries [54]. Their voltammetry analysis indicated a transformation in the Li_2O_2 formation pathway, from a surface-based process to one within the solution-when moving from traditional salt-in-solvent systems to SIS solutions. This finding implies that ultra-high concentration electrolytes can greatly improve the cycling durability of lithium/oxygen batteries. The SIS approach not only improved the stability of lithium-metal anodes but also opened new possibilities for other battery chemistries, including sodium-ion, potassium-ion, multivalent-ion, and lithium-air systems [55-57]. The application of SIS principles has led to improvements in cycle life, safety, and overall battery functionality.

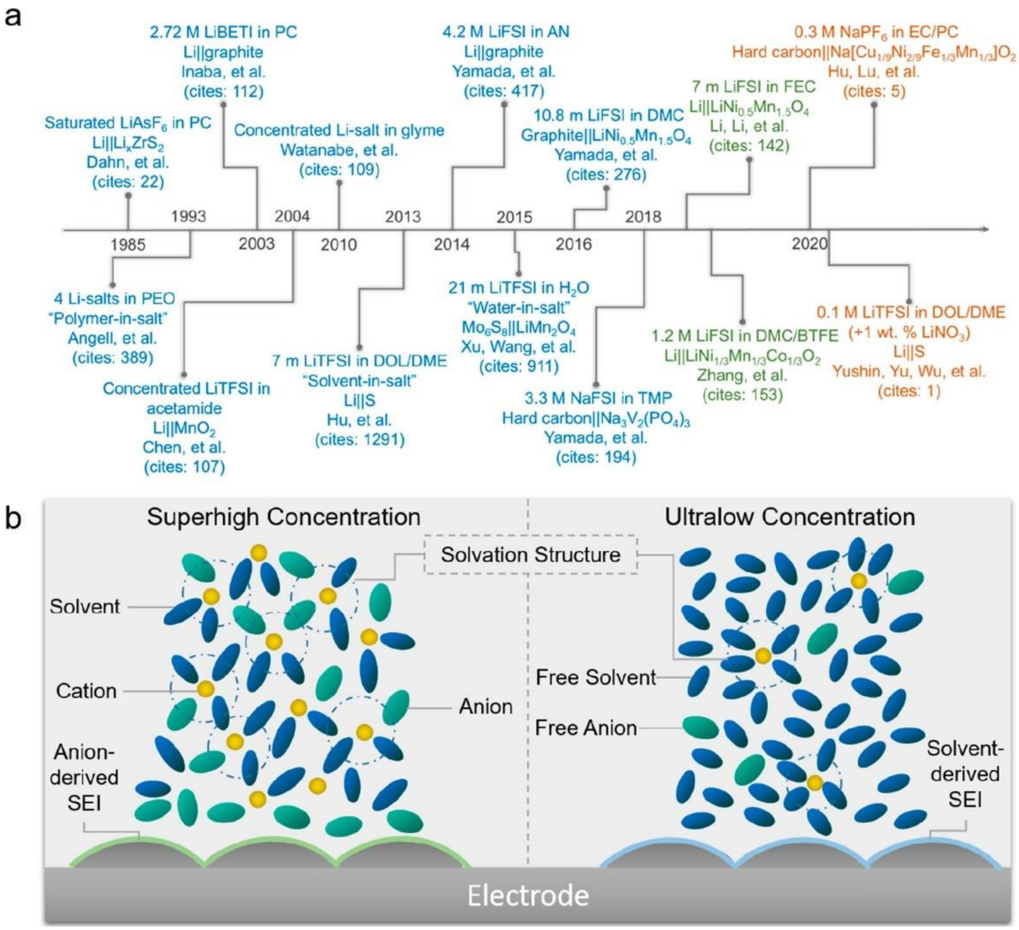

Figure 1.4 (a) Key research studies focused on electrolyte concentration in rechargeable batteries [46-52,58-65]. (b) Solvation and interfacial structures observed in both superhigh and ultralow concentration electrolytes. Reprinted (adapted) with permission from Ref. [46]. Copyright 2020 American Chemical Society.

1.2.2 Challenges and innovations in sodium-based electrolytes

Despite these advantages, the high cost associated with highly concentrated electrolytes remains a challenge, as large quantities of salts are required, limiting their commercial viability. To address this issue, Zhang and colleagues introduced the concept of localized high-concentration electrolytes (LHCEs) [59]. Xin et al. revealed that LHCE provides oxidative stability above 6 V versus Na/Na^+. Using this electrolyte, a cell with a $Na_{0.7}Li_{0.03}Mg_{0.03}Ni_{0.27}Mn_{0.6}Ti_{0.07}O_2$ cathode paired with a sodium anode retained 87.3% of its capacity after 200 cycles and achieved a high discharge rate of 84 mAh g^{-1} at 20 C with a cut-off voltage of 4.4 V [66]. In addition, Zhang et al. demonstrated that LHCE enhances the fast-charging capability of functional batteries. The selective breakdown of anions results in the formation of a stable and uniform SEI on the graphite electrode. This SEI layer effectively prevents ether solvents from co-intercalating with the graphite, thereby promoting highly reversible lithium-ion insertion and extraction [67]. LHCEs create a local environment that mimics the solvation structure of super-concentrated electrolytes, while the overall electrolyte remains in a dilute state. This approach balances performance with cost-effectiveness, preserving the benefits of high-concentration systems without their financial drawbacks.

Recent research by Wu and colleagues utilized a low-concentration electrolyte (0.1 M) to boost the lithium-sulfur conversion reaction at lower temperatures, showcasing the broad potential of this approach [68]. They also investigated a 0.2 M $LiPF_6$ electrolyte in FEC and EMC for high-voltage lithium metal batteries. This formulation significantly improved the electrochemical performance of both Li||Li symmetric cells and high-voltage $LiCoO_2$||Li batteries [69]. Meanwhile, Hu, Lu, and their teams has shown that not all systems require high-concentration electrolytes [60]. For example, ultralow-concentration electrolytes have been explored in sodium-based batteries, further reducing costs while expanding the operational temperature range. This trend reflects a broader movement toward tailoring electrolyte properties to meet the specific requirements of different battery chemistries.

In parallel, researchers are investigating the fundamental interactions within electrolytes, particularly focusing on solvation structures and interfacial interactions that directly affect battery performance (**Figure 1.4b**) [19,70-72]. Solvation structures describe how cations, anions, and solvent molecules interact, impacting electrolyte properties like viscosity, conductivity, and reactivity. These structures manifest as solvent-separated ion pairs (SSIPs), contact ion pairs (CIPs), or cation-anion aggregates (AGGs). At the same time, interfacial structures within the inner-Helmholtz layer influence the SEI’s formation and stability, which are critical to battery longevity and performance [70,73].

A particularly exciting development in this field has been the application of these electrolyte principles in aqueous systems. In 2015, Xu, Wang, and their colleagues introduced the water-in-salt (WIS) electrolyte, expanding the electrochemical stability range of water from 1.23 V to 3.0 V in aqueous lithium-ion batteries [58]. Soon after, Yamada et al. introduced a comparable system called "hydrate melt," which enhanced the stability of water-based electrolytes by incorporating a second salt at even higher concentrations [74]. These advances have sparked renewed interest in aqueous battery systems, which are known for their safety and environmental advantages [75,76]. While super-concentrated electrolytes hold great potential for improving battery performance, they are not without limitations. Continued research into electrolyte concentration has revealed new opportunities to better understand electrolyte chemistry and interfacial electrochemistry. As battery research progresses, innovations in electrolyte design will undoubtedly play a key role in shaping the next generation of high-performance batteries [77].

1.3 Advancing battery technologies: sodium-sulfur batteries

While improvements in electrolyte technology can significantly boost the performance of next-generation sodium-based batteries, sodium-based batteries still face challenges, particularly regarding their relatively low energy density, which restricts their suitability for applications demanding high energy storage capacity. In response, Na-S batteries have emerged as a viable alternative, offering several advantages such as the use of abundant, cost-effective materials and the potential for higher energy density [29,78,79]. Unlike sodium rechargeable batteries, Na-S batteries can operate efficiently at room temperature, avoiding some of the complications seen in high-temperature systems. These factors make Na-S batteries highly appealing for large-scale energy storage solutions, where affordability and sustainability are essential. However, achieving efficient and consistent charge–discharge cycling in Na-S batteries requires overcoming several obstacles.

1.3.1 Intrinsic challenges for Na-S batteries

The following sections will explore these issues and their underlying causes.

1. Sodium metal is highly reactive and oxidizes rapidly upon exposure to air, making storage and usage conditions quite challenging. The need for controlled environments complicates the practical application of Na-S batteries [80].
2. The majority of sodium-based batteries use organic electrolytes, which tend to degrade within the initial charge-discharge cycles. This degradation results in the formation of an unstable SEI on the sodium anode surface [81]. While this SEI layer can initially protect the anode by preventing further reactions with the electrolyte, uneven deposition of sodium metal can lead to dendrite formation. These dendrites not only consume more electrolyte and SEI but can also penetrate the separator, leading to internal short circuits. This issue worsens under high current or extended cycling conditions [82].
3. The larger ionic radius of sodium (1.02 Å compared to lithium's 0.76 Å) poses additional challenges in finding suitable storage materials that can facilitate the reversible insertion and extraction of sodium ions. The repeated sodiation and desodiation processes result in significant volume changes within the electrode, which can cause structural collapse. When the electrode structure breaks down, the existing SEI film also deteriorates, requiring additional electrolyte to

form a new SEI layer. The continual degradation cycle undermines long-term cycling performance in Na-ion batteries. Moreover, on the sulfur cathode side, the significant 80% volume expansion from sulfur (S) to sulfide (S^{2-}) compounds the instability of the electrode [32].

4. The large radius of sodium (Na^+) and S^{2-} reduce ion mobility and slow down electrochemical reactions, resulting in increased polarization, sluggish reaction kinetics, and lower capacity output [83].

5. During the charge-discharge process, sodium polysulfides (Na_2S_x, where $4 \leq x \leq 8$) are formed as intermediate products. These polysulfides are highly soluble in organic electrolytes, such as those based on ethers. While their solubility enhances reaction kinetics, it also triggers the polysulfide shuttle effect. Driven by concentration gradients and the electric field, dissolved polysulfides migrate through the separator toward the sodium anode, where they undergo side reactions. These side reactions create insoluble sodium sulfides (Na_2S_2 and Na_2S) on the anode, disrupting the SEI layer and further destabilizing the anode. This process is irreversible, leading to the gradual depletion of active sulfur material and severely limiting the long-term cycling stability of Na-S batteries [84].

6. Even when the battery is at rest, a slow internal redox reaction occurs due to the potential difference between the anode and cathode [85]. This leads to capacity loss over time. Furthermore, soluble polysulfides can lead to self-discharge by reacting with the sodium anode, further complicating the stability of Na-S systems.

1.3.2 Storage mechanisms of Na-S batteries

To tackle these challenges, a deep understanding of the reaction mechanisms in Na-S batteries is essential. As with lithium-sulfur (Li-S) batteries, the electrolyte is a critical factor influencing overall battery performance. The mechanisms of Na-S reactions are electrolyte dependent. For example, ether-based electrolytes allow for the dissolution of Na_2S_x intermediates, resulting in a solid-liquid-solid transformation during cycling. In contrast, ester-based electrolytes promote solid-solid reactions, as sulfur and Na_2S species are less soluble in them. Additionally, in solid-state electrolytes, the reaction pathways are simpler, eliminating many of the complications seen in liquid systems [86,87].

For instance, cyclic voltammetry (CV) and discharge curves for Na-S batteries using tetraethylene glycol dimethyl ether (TEGDME) as the electrolyte display two prominent reduction peaks at 2.20 V and 1.65 V as depicted in **Figure 1.5**. These peaks correspond to two plateaus in the discharge profile, which can be divided into four reaction regions [88,89]:

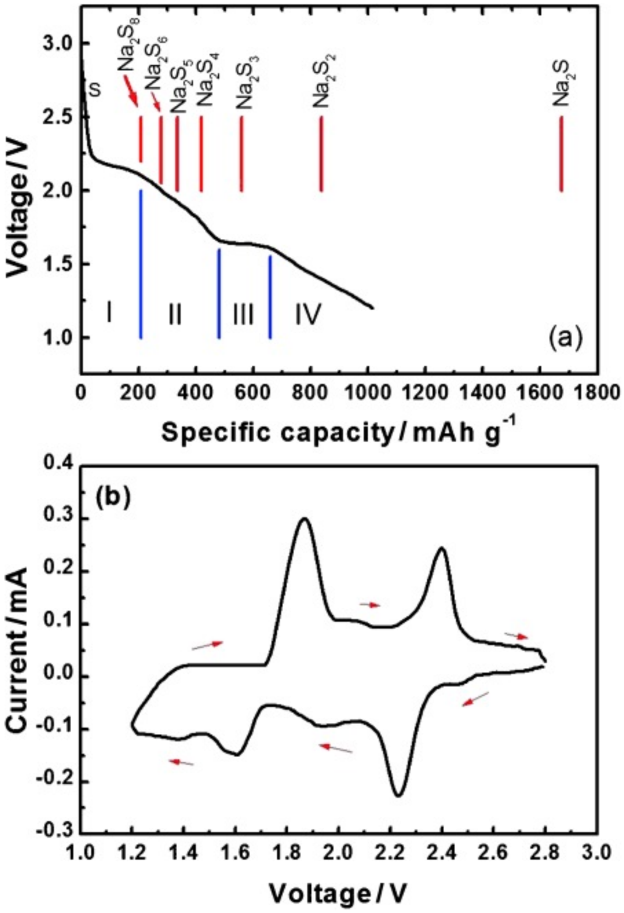

Figure 1.5 (a) Comparison between theoretical and actual discharge capacities, and (b) CV curves of Na-S cells at room temperature, recorded at a scan rate of 0.1 mV s^{-1}. Reproduced with permission from Ref. [88]. Copyright 2014 Wiley-VCH.

Region I (around 2.2 V): The high-voltage plateau signifies the conversion of solid sulfur (S_8) into dissolved Na_2S_8:

$$S_8 + 2\,Na^+ + 2\,e^- \rightarrow Na_2S_8 \tag{1-1}$$

Region II (2.2 V - 1.65 V) medium chain region reflects the conversion of long-chain polysulfides (Na_2S_8) into medium-chain polysulfides (Na_2S_4):

$$Na_2S_8 + 2\,Na^+ + 2\,e^- \rightarrow 2\,Na_2S_4 \tag{1-2}$$

Region III (1.65 V): The lower voltage plateau involves the conversion of Na_2S_4 into shorter chain polysulfides, such as Na_2S_3, Na_2S_2, and Na_2S:

$$3\,Na_2S_4 + 2\,Na^+ + 2\,e^- \rightarrow 4\,Na_2S_3 \tag{1-3}$$

$$Na_2S_4 + 2\,Na^+ + 2\,e^- \rightarrow 2\,Na_2S_2 \tag{1-4}$$

$$Na_2S_4 + 6\,Na^+ + 6\,e^- \rightarrow 4\,Na_2S \tag{1-5}$$

Region IV (1.65 V - 1.2 V): The final region corresponds to the solid-state transformation of Na_2S_2 into Na_2S:

$$Na_2S_2 + 2\,Na^+ + 2\,e^- \rightarrow 2\,Na_2S \tag{1-6}$$

Among these regions, Region II is the most complex due to the chemical equilibrium between various polysulfide species in the solution. Side reactions, including the formation of Na_2S_6 and Na_2S_5, can also occur, further complicating the electrochemical process.

Although the high solubility of Na_2S_x intermediates in ether-based electrolytes enhances reaction kinetics, it also exacerbates the polysulfide shuttle effect, reducing cycling stability. Moving forward, addressing the shuttle effect and other challenges (e.g., dendrite formation, electrolyte decomposition, and self-discharge) is essential to unlocking the full potential of Na-S batteries for large-scale energy storage applications [90-92].

The key difference between ester and ether solvents lies in their reactivity with nucleophilic S_x^{2-} species. In ester solvents, a violent nucleophilic reaction occurs between polysulfides and the solvent. However, in ester-based electrolytes, sodium polysulfides (NaPSs) exhibit lower solubility compared to ether-based electrolytes, effectively reducing the polysulfide shuttle effect. This improvement enables more efficient sulfur utilization in Na-S batteries employing ester electrolytes.

Recent studies have increasingly employed ester electrolytes in Na-S systems due to these benefits [93]. For example, Dou et al. developed a cathode material consisting of core-shell carbon spheres modified with nano-silver and loaded with sulfur, paired with an electrolyte solution of 1 M $NaClO_4$ in a blend of ethylene carbonate (EC), propylene carbonate (PC), and fluoroethylene carbonate (FEC) [94]. This combination demonstrated excellent performance and cycle stability. Na-S batteries based on ester electrolytes display two distinct peaks during the discharge process. Unlike ether-based systems, which contribute capacity through multiple reaction regions, the capacity in ester-based Na-S batteries is predominantly derived from two solid-state reactions. This more straightforward reaction mechanism makes it easier to analyze and address the issues associated with Na-S battery performance.

A notable characteristic of ester-based Na-S batteries is the high irreversible capacity below 1.4 V during the first discharge cycle, resulting from SEI formation. Furthermore, electrolyte decomposition produces a cathode-electrolyte interphase (CEI) on the sulfur cathode. In later cycles, this CEI facilitates a quasi-solid-state phase transition in sulfur particles, thereby minimizing the formation of soluble polysulfide intermediates. This simplifies the reaction process, allowing for targeted analysis and mitigation of specific performance limitations in Na-S batteries [95,96].

1.3.3 Strategies for efficient sulfur utilization in Na-S batteries

Given the similarities in working mechanisms between Li-S and Na-S batteries, researchers have drawn insights from Li-S battery research to address the challenges of Na-S batteries. One common approach involves using three-dimensional (3D) carbon materials to form composite sulfur cathodes. These 3D carbon frameworks enhance electron transport, increasing the overall reaction rate. Furthermore, the carbon structures help limit sulfur dissolution and provide some degree of adsorption for polysulfides, reducing the polysulfide shuttle effect [97-99].

In Na-S batteries, sulfur is typically encapsulated within 3D carbon frameworks using a thermal diffusion technique, also known as melt impregnation. This approach incorporates sulfur into various carbon structures, such as carbon nanotubes, hollow carbon spheres, carbon nanofibers, and porous carbon networks [100-102]. This method allows better bonding between sulfur and the carbon structure, thereby improving the electrochemical performance of the cathode. For example, Wan et al. developed a novel sulfur storage material by wrapping carbon nanotubes (CNTs) with microporous carbon tubes (MPCs) to form a concentric circular structure (S/(CNT @ MPC)) [32]. The microporous carbon structure restricts sulfur to smaller molecules (S_{2-4}), thereby limiting the formation of soluble NaPSs. This design also helps trap NaPSs within the carbon framework, reducing the polysulfide shuttle effect. The CV results showed a sharp initial redox peak due to the activation of the electrode and SEI formation. Over time, the reaction stabilized, and the battery exhibited smooth electrochemical performance. At a current density of 0.1 C (1 C = 1675 mA g^{-1}), the sulfur cathode delivered a capacity of 1610 mAh g^{-1}, with an initial efficiency of 71.3% due to electrode activation and SEI formation. After 2-3 cycles, the battery capacity stabilized around 900-800 mAh g^{-1}, demonstrating high coulombic efficiency and stability over time.

Dou et al. employed interconnected mesoporous carbon hollow nanospheres (iMCHS) as sulfur hosts using a melt-diffusion technique [103]. This technique trapped sulfur inside the hollow nanospheres, promoting strong interaction with the carbon matrix. This configuration enhanced electrochemical performance and significantly reduced the polysulfide shuttle effect. X-ray diffraction (XRD) data indicated that Na_2S formed during discharge did not revert to long-chain NaPSs upon recharging, highlighting the constrained conversion within the iMCHS structure. The Na-S battery showed impressive performance across different current densities, delivering a capacity of 390 mAh g^{-1} at 0.1 A g^{-1} and 127 mAh g^{-1} at a high current density of 5 A g^{-1}.

Xia et al. synthesized ultra-microporous carbon with pore sizes of approximately 0.5 nm using coffee grounds as the raw material [104]. Sulfur was introduced into larger pores via melt diffusion, and subsequent high-temperature treatment allowed S_{2-4} to occupy the ultra-microporous carbon structure. Theoretical calculations verified that these small pores effectively prevent NaPS formation, allowing sulfur to remain in small molecular form, with Na_2S as the main reaction product. The strong bonding between Na_2S and the carbon framework enhanced electronic conductivity, promoting faster reaction kinetics and better capacity retention. This material demonstrated outstanding cycling stability, maintaining a steady capacity across 2000 cycles at a rate of 1 C.

Moreover, research by Dou et al. demonstrated the importance of optimizing the structure and porosity of 3D carbon frameworks to enhance polysulfide retention and improve overall Na-S battery performance [105].

The above studies indicate that 3D carbon frameworks offer a promising direction for improving sulfur utilization in Na-S batteries. These structures enhance electron transport, reduce polysulfide dissolution, and provide improved electrolyte wettability. However, the non-polar adsorption capabilities of carbon are limited, making it difficult to fully bind NaPSs. Additionally, simply enhancing conductivity does not effectively accelerate NaPS conversion [106].

To address these limitations, researchers have introduced heteroatom doping into carbon frameworks. This method increases the number of active sites within the 3D carbon structure, which enhances ion transport, boosts reaction rates, and improves electrode stability. The incorporation of polar adsorption sites and heteroatoms also enhances the binding of NaPSs, mitigating the polysulfide shuttle effect. Furthermore, heteroatoms promote catalytic conversion of NaPSs, enhancing reaction kinetics and overall battery performance [107,108].

1.3.4 Electrolyte design for Na-S batteries

A standard battery consists of electrodes (cathode and anode), an electrolyte, separators, and current collectors. Battery performance relies not only on the choice of electrode materials but also significantly on the electrolyte type. Electrolytes enable ion transport and block electron flow between electrodes, preventing short circuits. In Na-S batteries, liquid electrolytes generally contain two essential components: a solvent and a sodium salt.

Common solvents include esters, ethers, and other organic compounds. Key properties are evaluated when choosing a solvent: dielectric constant, viscosity, and electron-donating capacity. A high dielectric constant promotes sodium salt ionization, strong electron-donating ability aids in salt dissolution, and low viscosity enables greater ion mobility, thereby enhancing ionic conductivity [109,110].

Sodium salts, as the solute, provide the current-carrying capacity in the electrolyte. Important factors when choosing a sodium salt include its stability within the battery system, self-discharge rate, ionic conductivity, and safety profile (non-toxicity, non-pollution). Common sodium salts used in Na-S batteries include $NaPF_6$, $NaClO_4$, and $NaCF_3SO_3$.

Currently, most Na-S batteries rely on organic electrolytes, but these come with safety concerns. Sodium dendrite formation and complex side reactions at the cathode lead to the production of NaPSs. These NaPSs dissolve in the electrolyte and eventually reach the anode, resulting in the loss of active sulfur material and reduced battery efficiency. As a result, significant research is focused on electrolyte optimization to enhance the commercial viability and safety of Na-S batteries [111,112].

1.3.5 Strategies for safe sodium anodes

Sodium metal presents unique challenges when used as an anode material due to its high reactivity. It easily reacts with electrolytes, leading to the formation of a SEI on the anode surface. This reaction, while essential for battery operation, also results in electrolyte consumption and capacity loss over time. Additionally, sodium's soft nature makes it prone to cracking, which exposes fresh sodium to the electrolyte, further accelerating degradation [35,113,114].

One of the most critical issues is the uneven deposition of sodium, which promotes the growth of dendrites-needle-like structures that can pierce the separator and cause short circuits. This poses significant safety risks, especially in large-scale applications. Furthermore, in sodium-sulfur (Na-S) batteries, the shuttle effect of sodium polysulfides (NaPSs) exacerbates anode corrosion, reducing battery performance and long-term stability [36,115].

Given these challenges, stabilizing sodium metal anodes is vital for the practical use of Na-S batteries. Several strategies have been proposed to enhance the safety and efficiency of sodium metal anodes:

1. ***Optimization of Electrolytes and Additives:*** The selection of appropriate electrolytes and additives can encourage the formation of a stable SEI layer on the sodium anode. This layer helps protect the anode from further degradation, ensuring improved long-term stability.
2. ***Anode Surface Modification:*** Pretreating the anode surface through chemical or physical modifications can create an artificial SEI layer. This engineered layer remains stable over time, reducing the sodium metal's reactivity with the electrolyte.
3. ***Designing 3D Electrode Structures:*** A 3D electrode structure can promote uniform sodium ion deposition, mitigating dendrite growth. These structures also enhance the conversion efficiency of sodium ions into sodium metal, which improves battery safety and performance.

1.4 Conclusions

This thesis focuses on solving critical challenges in sodium-based battery technology by exploring innovative approaches to improve performance and reliability. The research is divided into three primary projects, each addressing different aspects of sodium-based battery development:

Project 1: Enhancing Electrolyte Formulation for Sodium Metal Batteries

The electrolyte is one of the most crucial components in a battery, facilitating ion movement between the electrodes. In sodium metal batteries, developing an electrolyte that performs efficiently over a wide temperature range while maintaining safety and cost-effectiveness is a key challenge. This project introduces a low-concentration, non-flammable electrolyte that significantly enhances the cyclability and performance of sodium metal batteries, even under extreme temperature conditions. Molecular dynamics (MD) simulations show that improved ion-pairing mechanisms contribute to better sodium ion transport, resulting in improved battery performance. Despite these advancements, sodium metal batteries still face limitations in energy density and cycle life, particularly in high-demand applications like grid storage.

Project 2: Advancing Na-S Batteries

To address the limitations of energy density and cycle life in sodium metal batteries, this project focuses on the development of Na-S batteries. Na-S batteries offer higher theoretical capacity due to sulfur's energy density. However, the polysulfide shuttle effect and dendrite formation are two significant challenges that hinder the commercial viability of Na-S batteries. The polysulfide shuttle occurs when sodium polysulfides migrate between the electrodes, causing capacity loss over time. Meanwhile, dendrite growth on the sodium metal anode increases the risk of short circuits. This project introduces the innovative use of acoustic waves to suppress dendrite growth and mitigate the shuttle effect, significantly improving the safety and efficiency of Na-S batteries. These advancements bring Na-S technology closer to large-scale application in energy storage systems.

Project 3: Investigating Sodium Polysulfide Behavior

The third project addresses fundamental questions regarding the behavior of sodium polysulfides in Na-S and sodium-oxygen-sulfur (Na/O_2-S) systems. A key focus is understanding the mechanisms behind the precipitation of sodium sulfides (Na_2S_x, $x \leq 2$) and how these processes are influenced by operating conditions such as voltage and solvent composition. By gaining a deeper understanding of the nucleation and growth of sodium polysulfides, this project provides crucial insights into optimizing battery designs for improved performance and longevity.

Chapter 2 - Low-Concentration Electrolyte Design for Wide-Temperature Operation in Sodium Metal Batteries

2.1 Abstract

Sodium metal batteries (SMBs) are cost-effective and environmentally sustainable alternative to lithium batteries. However, at present, limitations such as poor compatibility, low coulombic efficiency (CE), and high electrolyte cost hinder their widespread application. Herein, we propose a non-flammable, low-concentration electrolyte composed of 0.3 M $NaPF_6$ in propylene carbonate (PC), fluoroethylene carbonate (FEC), and 1,1,2,2-tetrafluoroethyl 2,2,3,3-tetrafluoropropyl ether (TTE). This low-concentration electrolyte not only reduces cost but also delivers rapid ion diffusion and superior wetting properties. While the Na||$FePO_4$ system with this electrolyte demonstrates slightly reduced performance at room temperature compared to standard-concentration formulations (S-PFT), it excels at both high (55 °C) and low (-20 °C) temperatures, showcasing its balanced performance. At 0.5 C (charge) / 1 C (discharge), capacity retention reaches 92.8% at room temperature and 98.5% at elevated temperature, with CE values surpassing 99% and 99.63%, respectively, and significant performance sustained at -20 °C at 0.2 C. This electrolyte development thus offers a well-rounded, economically viable path to high-performance SMBs for diverse environmental applications.

2.2 Introduction

Electric vehicles and electric grids powered by renewable, but typically intermittent energy sources demand low-cost, high-performance electrochemical energy storage technologies. Due to their high energy density and stability, lithium metal batteries (LMBs) currently hold a leading position in meeting this demand. However, LMBs are expensive and largely infeasible for grid-scale energy storage applications due to a lack of lithium (approximately 0.0065% in the earth's crust). Hence, it is critical to develop alternative battery technologies. Sodium metal batteries (SMBs) are gaining popularity due to their low cost (\$50-100 kWh^{-1}), and abundant sodium (around 0.048% in the earth's crust) [116-118].

The performance of SMBs, however, is still far from ideal in large part due to limited research in sodium-based chemistry [3,119,120]. Current research on SMB focuses on electrolyte and electrode materials, as well as interactions between electrode and electrolyte [12,17,121]. In particular, electrolytes in SMBs are a crucial element that influences the electrochemical window, energy density, and properties of the electrode/electrolyte interfaces. However, the mainstream organic electrolytes for SMBs suffer from flammability, low thermodynamic stability, and toxicity. Indeed, it remains a great challenge to create SMB electrolytes that are non-flammable, thermodynamically stable, and eco-friendly.

In developing SMB electrolytes, much effort has been dedicated to introducing flame retardants, inert diluents, and ionic liquids to address the limitations of existing electrolytes [70,122,123]. For instance, Chang et al. developed a 0.5 M NaTFSI-incorporated MBP-ionic liquid electrolyte to replace conventional organic electrolyte, and at a rate of 1 C, the Na||$NaFePO_4$ cell demonstrated steady cycling performance with 65% capacity retention [124]. Zhang et al. proposed a non-flammable electrolyte containing NaFSI-triethyl phosphate (TEP)/1,1,2,2-tetrafluoroethyl-2,2,3,3-tetrafluoropropyl ether (TTE) (1:1.5:2 in mole), in which the Na||$NaCu_{1/9}Ni_{2/9}Fe_{1/3}Mn_{1/3}O_2$ (Na-CNFM) with a coulomb efficiency (CE) of 99.8-99.9% over 100 cycles at 0.2 C [70]. These studies effectively tackle some key limitations of standard electrolytes, but they are generally restricted to room temperature, although an ideal SMB electrolyte should work in a wide temperature range. As such, new strategies are needed in the development of SMB electrolytes.

Previous works on wide-temperature SMBs generally focused on applying standard or high-concentration salts to improve the wide-temperature performance. Wu et al. designed sodium bis(trifluoromethylsulfonyl)imide (NaTFSI) in N-methyl-N-propylpyrrolidiniumbis(fluorosulfonyl)imide ($[Py_{13}][FSI]$) and 1,2-bis (1,1,2,2-tetrafluoroethoxy) ethane (TFEE) (1:3:1 by molar ratio, ~1.15 M). These dedicated electrolytes showed outstanding long-term cycling performance with a capacity retention of 95.5% at 5 C after 2000 cycles at 25 °C, CE of ~ 99% after 240 cycles at 60 °C, and specific capacity of 132 mAh g^{-1} achieved by the NFM||Na cell at -20 °C [125]. Similarly, Chou et al. introduced succinonitrile (SN)-based electrolyte containing $NaClO_4$/SN/1,3,2-dioxathiolane-2,2-dioxide (~2 M), which delivered a capacity retention of 82.8% after 800 cycles (25 °C) and 86.3% after 100 cycles (60 °C) [126]. However, given that the Stokes radius and de-solvation energy of Na^+ are less than those of Li^+. We hypothesize that it is possible to maintain acceptable even better performance from SMBs with low-concentration electrolytes even at wide temperatures.

To verify the above hypothesis, we report an electrolyte consisting of 0.3 M (hereafter refer to as L-PFT)/1.0 M (as reference group, S-PFT) $NaPF_6$ dissolved in a mixture of propylene carbonate (PC), Fluoroethylene carbonate (FEC), and 1,1,2,2-tetrafluoroethyl 2,2,3,3-tetrafluoropropyl ether (TTE) (3:3:4 by volume). This well-designed electrolyte exhibits non-flammability, high compatibility with both Na metal anode and cathode as well as better electrochemical performance. Benefiting from this electrolyte, the as-developed Na||$FePO_4$ battery delivered a capacity retention of 94.8% at 0.5 C (charge) /1 C (discharge) with a very high CE of 99.88% over 350 cycles for S-PFT. The reduced conductivity of L-PFT still affords acceptable capacity retention and CE, which are 2% and 0.46% lower than those of S-PFT. The cells with L-PFT showed capacity retention of 90.8% even at a high rate of 2 C after 500 cycles. Surprisingly, the cell performs with L-PFT at temperatures of 55 °C better than S-PFT due to $NaPF_6$ decomposition. The problem of thermodynamic stability is thus the main one to take into account at high temperatures compared to the room temperature. Furthermore, the low viscosity, rapid diffusion rate, and improved wetting performance of the battery with L-PFT allow for significant performance at low temperatures (-20 °C). The present electrolyte design, in our opinion, offers a fresh approach to improve the viability of SBM technology, particularly concerning its coulomb efficiency, capacity performance, and compatibility.

2.3 Experimental section

2.3.1 Electrolytes preparation

Electrolyte was prepared by stirring propylene carbonate (PC, Alfa Aesar), Fluoroethylene carbonate (FEC, Alfa Aesar) and 1,1,2,2-Tetrafluoroethyl 2,2,3,3-Tetrafluoropropyl Ether (TTE, Fisher Scientific) by a volume ratio of 3:3:4, along with different amount of sodium hexafluorophosphate ($NaPF_6$, 99+%, Alfa Aesar) for 1 day. The total $NaPF_6$ in the electrolyte were 0.3 M (labeled as L-PFT) and 1.0 M (S-PFT). 1.0 M $NaPF_6$ in PC was also prepared. The electrolyte was dried on molecular sieves for 7 days. The $NaPF_6$ salt was dried at 100 °C for 12 hours. All electrolyte preparation and cell assembly steps were performed inside an argon-purged glove box (O_2 and H_2O < 0.1 ppm).

2.3.2 Preparation of materials

Nitronium tetrafluoroborate (NO_2BF_4, Sigma) in acetonitrile was used to chemically de-lithiate $LiFePO_4$ to produce $FePO_4$. 0.85 g of NO_2BF_4 were dissolved in 50 mL of acetonitrile before being mixed with 0.5 g of $LiFePO_4$ (MTI Corporation). The mixture is continuously bubbled with argon for 24 hours at room temperature, then centrifuged and repeatedly washed with acetonitrile and distilled water. The finished product is dried in a vacuum at 80 °C for 12 hours.

2.3.3 Cell assembly and electrochemical testing

The cathode consists of $FePO_4$, carbon nanotubes, and polyvinylidene fluoride (PVDF) binder with a mass ratio of 8:1:1 in N-methyl-2-pyrrolidone (NMP). Then homogeneous slurry was cast onto the aluminum foil. All cathodes were dried at 80 °C in a vacuum for 12 hours. The average active material mass loading is ~1.7 mg cm^{-2}. Electrochemical performances of the electrolytes were tested in $FePO_4$||Na, assembled with $FePO_4$, Na metal and glass microfiber filters (GF/D, Whatman) with 80 μL electrolyte.

The $FePO_4$||Na cells were galvanostatic cycled between 1.5 and 4.0 V on a LAND test system (Wuhan LAND Electronics Co., Ltd.) at room temperature and repeated for each electrolyte. The first three cycles were carried out at 0.1 C (1 C = 154 mA g^{-1}) before long term cycling at 0.5 C, 1 C (charge with 0.5 C) and 2 C. Rate cycle performance was measured at 0.1, 0.2, 0.5, 1, 2, 5 and 10 C. Na-Hard carbon||$FePO_4$ was cycled within a voltage range of 1.5-4 V at 0.5 C after formation under 0.1 C for 3 cycles (1 C = 154 mA g^{-1}).

Na||Na symmetric cells were tested at a current density of 1.0 mA cm^{-2} with a fixed areal capacity of 1.0 mAh cm^{-2}. Cyclic voltammetry (CV) tests with voltages ranging from 1.5 V to 3.8 V for the $FePO_4$ are performed under various scan rates.

2.3.4 Microscopy characterization

Electrolyte viscosities and densities were assessed using a Discover HR-30 rheometer with a UV option. Conductivity measurements were performed with a HI2020-01 Edge Laboratory conductivity meter. The electrolyte wetting behavior was evaluated through contact angle analysis using a Biolin Scientific Theta Flow instrument. To analyze the crystal structure of $FePO_4$ electrodes pre- and post-cycling, X-ray diffraction (XRD) was conducted on a Rigaku SmartLab system with Cu Kα radiation. The CEI composition was characterized by X-ray photoelectron spectroscopy (XPS, PHI Quantera SXM). Raman spectroscopy (WITec alpha500) provided insights into the electrolyte's solvation structure.

2.3.5 MD simulations

To study the effect of salt concentration and temperature on solvation structure in electrolytes, six different systems were built: 0.3 M $NaPF_6$ in PC/FEC/TTE = 3:3:4 in vol% at (1) 253K, (2) 300K, (3) 328K; 1M $NaPF_6$ in PC/FEC/TTE = 3:3:4 in vol% at (4) 253K, (5) 300K, (6) 328K. The simulation system is composed of Na^+ ions, PF_6^- ions, PC, FEC, and TTE solvents. Each simulation box measures $50\times50\times50$ $Å^3$ and is subsequently amorphously packed with solvent and salt using Packmol [127]. Beginning with a random configuration, an initial 5 ns equilibration was performed in the NPT ensemble to stabilize the system at 1 bar pressure and 300 K temperature, using a 1 ps time constant. This was followed by an annealing phase to ensure full melting of the systems and prevent local configuration constraints. The systems were heated from 300 K to 400 K over 2 ns, held steady at 400 K for another 2 ns, and then gradually cooled to the target temperature over a further 2 ns. A final NVT simulation was conducted at the target temperature for 55 ns, with statistical data collected from the last 50 ns of the run.

The salts and solvents were described using OPLS-AA force fields [128]. The Lorentz-Berthelot rule (arithmetic and geometric mean for Lennard-Jones parameters σ and ε, respectively) was used in all MD simulations [129]. To account for ion polarizability without incurring excessive computational cost, the computational charges were scaled by 0.8 as is widely practiced in ionic liquids simulations [130,131]. The atomic partial charges and force field parameters for TTE solvent are obtained from Saito et al [129].

Simulations were performed using Gromacs 2021 code [132,133]. Ion temperature is maintained at the target temperature using the velocity rescaling thermostat with a time constant of 0.1 ps. A time step of 2 fs is used to march the system. The electrostatic interactions are calculated using the Particle Mesh Ewald (PME) method. In the PME method, an FFT spacing of 0.12 nm is taken for the k-space part of the electrostatic calculation and a cutoff scheme (cutoff length: 1.2 nm) is used for the real-space part of the electrostatic calculations. A cut-off length of 1.2nm is employed for the non-electrostatic interactions (Lennard-Jones, LJ). The periodic boundary conditions are applied to all xyz directions.

2.4 Results and discussion

2.4.1 Design and reveal solvation structures in two electrolytes

Figure 2.1 illustrates the design strategy for our electrolyte. By varying the ratio of different salts, we modulate the interactions between Na ions and solvents, which, in turn, influence the electrolyte's physical properties and interfacial behavior, thereby affecting its electrochemical performance. Specifically, $NaPF_6$ sodium salts were selected for their outstanding electrical conductivity and strong electrochemical stability. Propylene carbonate (PC) is employed as a solvent for dissolving sodium salts, known for its good conductivity. Indeed, 1.0 M $NaPF_6$ in PC is a SMB electrolyte. However, this electrolyte is associated with elevated interfacial impedance at Na metal anodes and accompanied by the continuous growth of electrolyte/electrode interphase. Recent studies have identified fluoroethylene carbonate (FEC) as a cosolvent (or additive), where its preferential defluorination generates an interphase rich in NaF, significantly enhancing the stability of metallic Na [73,134,135]. Despite these improvements, the electrolyte composed of 1.0 M $NaPF_6$ in FEC/PC still exhibits substantial flammability, as demonstrated in **Figure 2.2a**, posing significant safety concerns for practical applications.

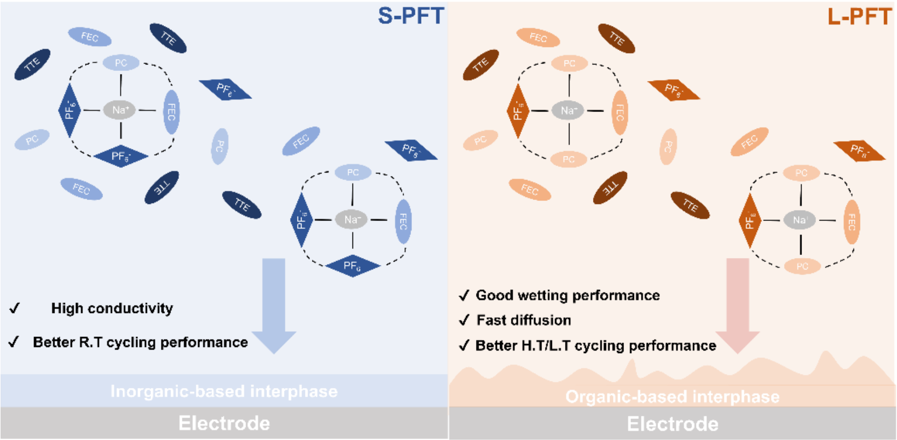

Figure 2.1 0.3 M (L-PFT) and 1.0 M (S-PFT) $NaPF_6$ in PC: FEC: TTE (3:3:4 vol%) mixed electrolytes design principle.

To address the issue of thermal stability, we introduced 1,1,2,2-tetrafluoroethyl 2,2,3,3-tetrafluoropropyl ether (TTE), a highly fluorinated ether. Recognizing that the inclusion of TTE may impact initial conductivity, a balanced approach was employed. To optimize both thermal stability and conductivity, we developed an electrolyte formulation of 1.0 M $NaPF_6$ in a PC: FEC: TTE mixture with a volumetric ratio of 3:3:4, designated as S-PFT. This formulation demonstrates high conductivity, an inorganic-derived interphase, and nonflammability, as depicted in **Figure 2.2b**. In comparison to S-PFT, the L-PFT electrolyte, with a reduced salt concentration of 0.3 M, exhibits faster sodium ion diffusion, an organic-based interphase, and improved wetting performance, allowing L-PFT to maintain competitive performance characteristics while enhancing the overall safety profile of the electrolyte.

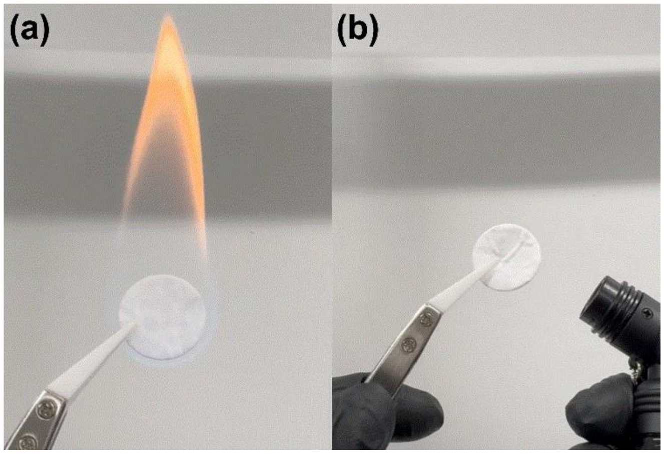

Figure 2.2 Combustion experiment of FEC/PC-based electrolyte (a) and PC/FEC/TTE (3:3:4 vol%) mixed electrolyte (b).

Electrolytes formulated with various solvents, sodium salts, and salt concentrations can result in substantial alterations in the Na^+ solvation structure. These changes can influence the interfacial composition and impact the plating/stripping behavior, thereby significantly affecting the overall electrochemical performance. To elucidate the solvation structure of the designed electrolytes, we conducted Raman spectroscopy experiments, as shown in **Figures 2.3**. The peak observed in the 710-730 cm^{-1} region, a distinct feature in this spectral range, was analyzed to identify the different states of the C=O breathing bond on the carbonate ring in propylene carbonate (PC) and fluoroethylene carbonate (FEC) [136,137]. Upon introducing $NaPF_6$ salt into these solvents, the peak shifted to a higher wavenumber, indicating an interaction between the salt and solvent molecules. Additionally, a new peak emerges at 742 cm^{-1}, which corresponds to the coordinated PF_6^- within the electrolyte [138]. In contrast, when $NaPF_6$ was utilized as the solute in TTE, no significant peak shift was observed, suggesting a negligible interaction between Na^+ and TTE.

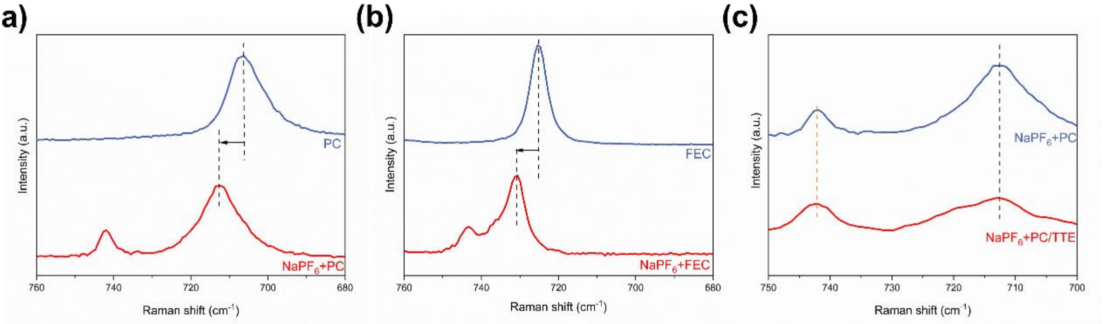

Figure 2.3 Raman spectra of PC (a), FEC (b), and TTE (c) solvent.

The above observation is further corroborated by the Raman spectra of mixed solvents with varying $NaPF_6$ concentrations, where distinct peak blueshifts were detected as the salt concentration increased to 0.3 M (**Figure 2.4**). At a high salt concentration of 1.0 M, the peak at 731 cm^{-1}, associated with solvent-separated ion pairs (SSIP) and contact ion pairs (CIP), exhibited a further blueshift, reflecting the formation of these ion pairs in different proportions. Notably, the L-PFT electrolyte exhibited a higher proportion of SSIP relative to CIP compared to S-PFT, alongside a reduced fraction of coordinated PF_6^- (742 cm^{-1}). These comparative results indicate that the interaction between PF_6^- and Na^+ diminishes progressively from S-PFT to L-PFT, with the strongest interaction observed in S-PFT. The relative distance (d) between PF_6^- and Na^+, where a greater distance signifies a weaker interaction, is used here as a qualitative measure of the PF_6^-/Na^+ interaction strength. This analysis is supported by variations in the chemical bonds within the electrolyte components, as reflected in the Raman spectra. Consequently, the relative distances between PF_6^- and Na^+ follow the sequence: S-PFT (d_1) < L-PFT (d_2).

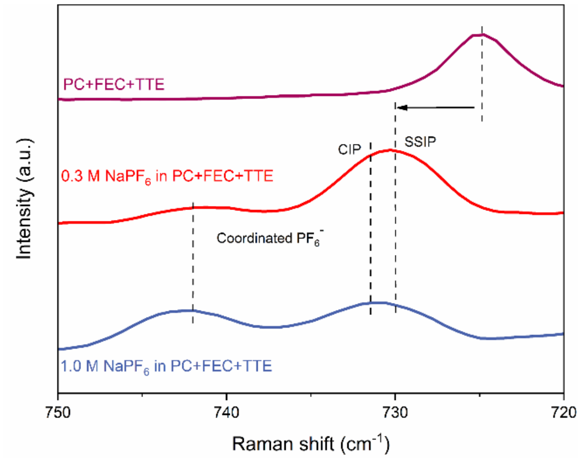

Figure 2.4 Raman spectra of pure, 0.3 M, and 1.0 M mixed electrolyte.

To further ascertain the solvation structure inferred from the above measurements, molecular dynamics (MD) simulations (**Figure 2.5**) were performed for L-PFT and S-PFT electrolytes.

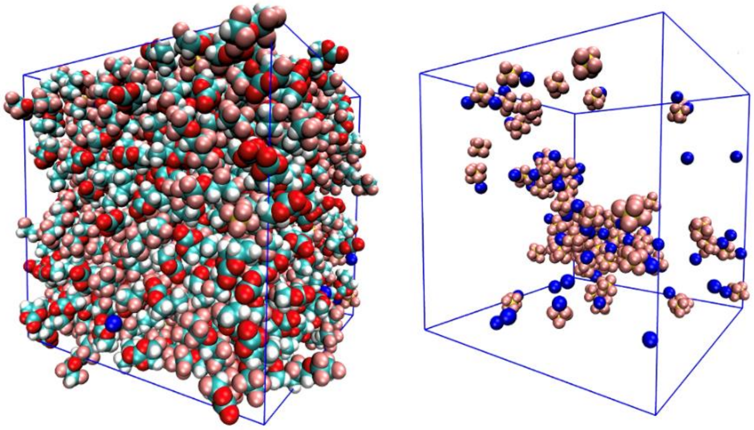

Figure 2.5 A snapshot of the MD system (a) with solvents and (b) without solvents for clarity. In (a) and (b), C, O, H, P, F, and Na are colored in cyan, red, white, tan, pink, and blue, respectively.

Figure 2.6b shows that, in L-PFT, PC, FEC, PF_6- participate in Na^+'s first solvation shell, while TTE does not, which is consistent with the previous study [70]. In L-PFT, PC and FEC solvents dominate Na^+ ion's solvation shell: the total coordination number by solvent is 6.1 (3.5 PC and 2.6 FEC) and there is a small coordination contribution from PF_6- (1.6 F atoms). In S-PFT (see **Figure 2.6d**), the total number of coordination solvent molecules decreases from 6.1 to 3.6, with 2 PC and 1.6 FEC, while the coordination by anions' F atoms in anions increases from 1.6 to 4.6. This trend indicates that, as the concentration of $NaPF_6$ increases, PF_6 anions are more engaged in the solvation sheath and solvents are gradually depleted.

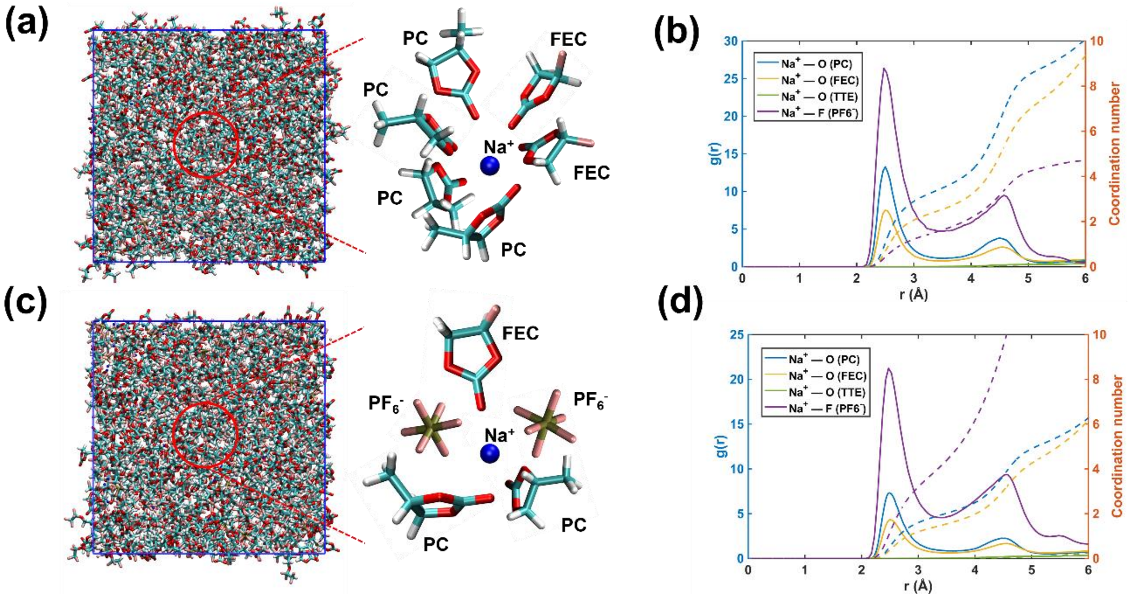

Figure 2.6 Snapshots of 0.3 M (a) and 1.0 M (c) electrolytes, along with their representative solvation structures. Radial distribution functions Na atoms in 0.3 M (b) and 1.0 M electrolytes (d). The dashed lines are the integrated radial distribution function for the coordination number of O and F around Na^+ (dashed lines).

From MD trajectories, we can also delineate the molecular state of Na^+ ions in L-PFT and S-PFT. Ions in an electrolyte can be categorized into three populations with different solvation states:

SSIPs, CIPs, and AGG [139,140]. As shown in **Figure 2.7**, in L-PFT, the majority (57.9%) of Na^+ ions are dissociated (SSIP); in S-PFT, the fraction of SSIP Na^+ ions decrease to 38.1% while that of AGG increases from 18.6% to 39.8%. Physically, increased concentration leads to stronger screening of electrostatic repulsion between cations or anions and thus allows them to come closer to form AGG. The MD simulations further indicate that the efficient assembly of a PF_6 anion-based structure in S-PFT promotes the formation of an inorganic-rich interphase, attributed to an increased ratio of CIPs and AGG. In contrast, L-PFT forms solvent-derived structures, aligning well with the trends observed through Raman spectroscopy. This concordance between MD simulation results and experimental Raman data supports the validity of the proposed solvation structures.

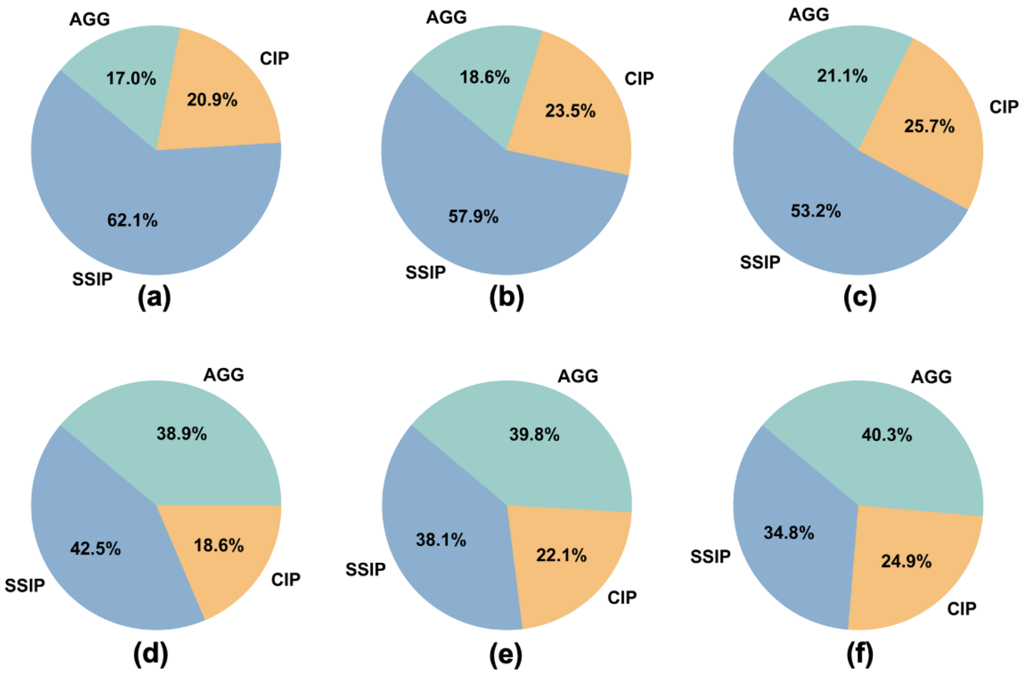

Figure 2.7 The population of SSIP, CIP, and AGG species in L-PFT electrolyte at 253 K (a), 300 K (b), 328 K (c), and in S-PFT electrolyte at 253 K (d), 300 K (e), 328 K (f).

2.4.2 Performance of designed electrolyte at room temperature

Figure 2.8 presents the X-ray diffraction (XRD) patterns of pure $LiFePO_4$ and chemically de-lithiated $FePO_4$. XRD patterns are indexed to the orthorhombic (*pnma*) crystal system and exhibit excellent agreement with previously reported data in the literature [141]. The absence of any detectable impurities, including residual lithium, in the $FePO_4$ samples is confirmed by the XRD patterns. This indicates the high purity of the synthesized materials and validates the effectiveness of the de-lithiation process.

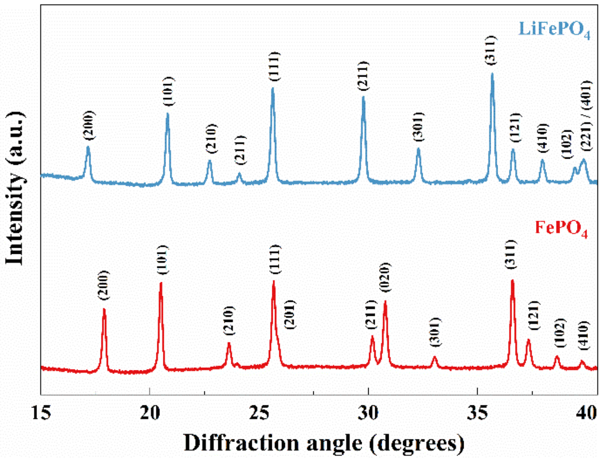

Figure 2.8 XRD patterns of pristine $LiFePO_4$ and $FePO_4$ obtained from chemical de-lithiation of $LiFePO_4$.

We assembled Na||$FePO_4$ cells to evaluate the impact of the designed electrolytes on cycling behavior with $FePO_4$. As illustrated in **Figure 2.9**, the initial discharge capacity of the cell with S-PFT electrolyte is 144.6 mAh g^{-1}. Furthermore, S-PFT demonstrates remarkable cyclability, with a capacity retention of 94.8% and an average coulombic efficiency (CE) of 99.88% after 350 cycles at a charge rate of 0.5 C and a discharge rate of 1.0 C.

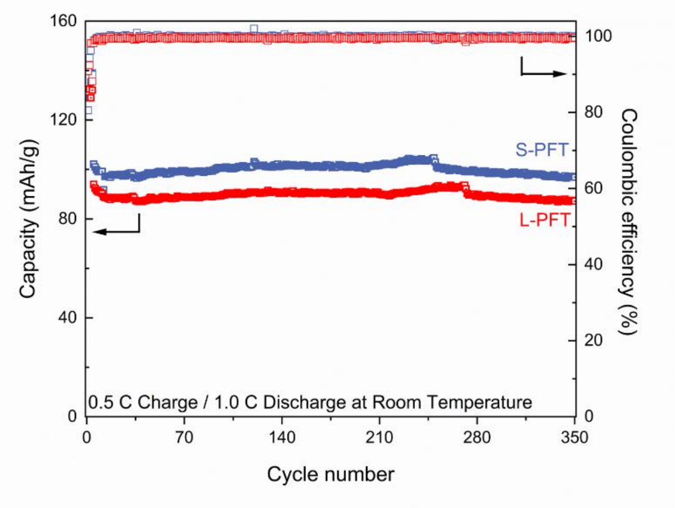

Figure 2.9 Cycling performance of the Na||$FePO_4$ cells with two electrolytes at 0.5 C charge/1.0 C discharge.

However, as illustrated in **Figure 2.10**, although L-PFT exhibits a lower viscosity (3.09 mPa·s) compared to S-PFT (5.83 mPa·s), and superior wetting properties, as indicated by its smaller contact angle of 17.9° at 0.3 M concentration (versus 27.69° for S-PFT at 1.0 M concentration, **Figure 2.11**), there is a marginal decline in its overall electrochemical performance. This reduction in performance can be attributed to the slightly lower conductivity of L-PFT (3.83 mS cm^{-1}) compared to S-PFT (5.26 mS cm^{-1}). Despite this, the enhanced wetting properties and lower viscosity of L-PFT could contribute to better electrolyte penetration and ion transport, which may partially offset the impact of reduced conductivity on long-term cycling stability.

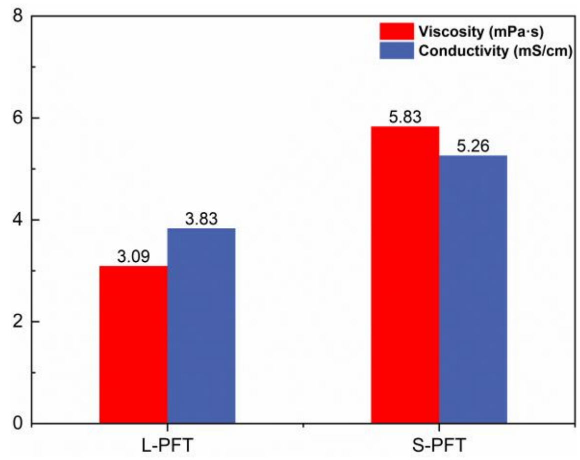

Figure 2.10 Comparison for viscosity and conductivity of L-PFT and S-PFT at room temperature.

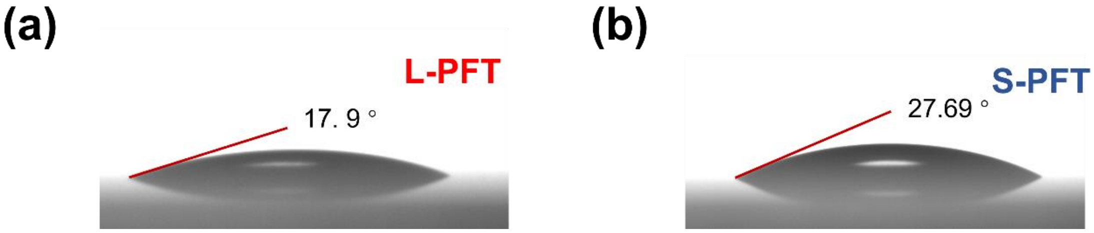

Figure 2.11 Contact angle of L-PFT (a) and S-PFT (b).

Furthermore, we further tested the diffusion coefficient of L-PFT and S-PFT to evaluate kinetics, which reflects the Na^+ transportability by CV at various scanning rates. In **Figure 2.12**, the linear association between the peak currents and the square root of scanning rates suggested a diffusion-dominated process. Related calculation is based on the following equation:

$$I_p = (2.69 \times 10^5)\, n^{1.5}\, A\, D^{0.5}\, C\, v^{0.5} \qquad (2\text{-}1)$$

where A is area, C is bulk phase concentration, D is Na^+ diffusion coefficient, v is scanning rate, n is valence state (n=1 for sodium ion), and I_p is peak current. n, A, and C are consistent among them. Thus, the question could be summarized as follows:

$$\frac{I_p}{v^{0.5}}\, (slope) = constant \times D^{0.5} \qquad (2\text{-}2)$$

The slope value of the fitting line ($\frac{I_p}{v^{0.5}}$) for the same type of cathode represents the level of the; the greater the slope, the quicker the Na$^+$ diffuses. Whether it is oxidation or reduction, as demonstrated, cells with L-PFT exhibit a bigger slope than cells with S-PFT, which suggests that L-PFT exhibit higher D_{Na}^{+} than S-PFT.

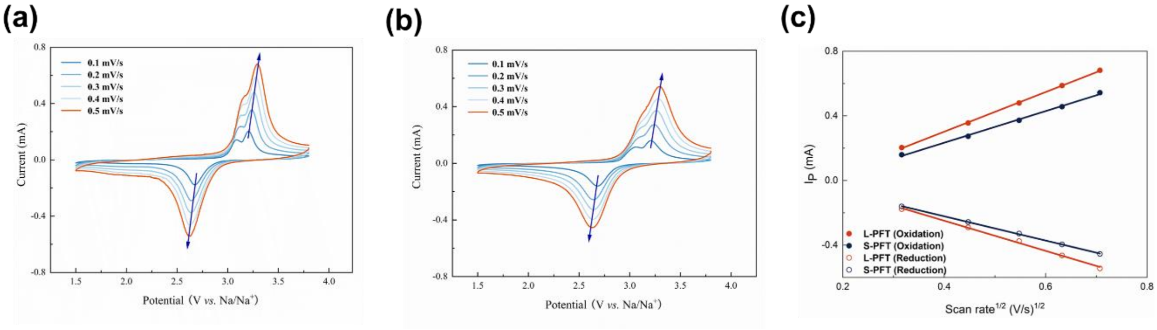

Figure 2.12 Cyclic voltammetry curves of cell with L-PFT (a) and S-PFT (b) at different scan rates. (b) Comparison for diffusion coefficient of L-PFT and S-PFT.

Although the reduction of sodium salt in L-PFT results in decreased conductivity, which negatively impacts its electrochemical performance, this is somewhat compensated by its faster diffusion rate relative to S-PFT. Therefore, L-PFT experiences a reduction in capacity retention and Coulombic efficiency (CE) by approximately 2% and 0.46%, respectively. Despite these slight decreases, L-PFT still outperforms traditional PC-based electrolytes, which suffer near-total capacity loss after only 150 cycles. Furthermore, L-PFT exceeds the performance of several other electrolytes reported in the literature, as highlighted in **Figure 2.13** and **Table 2.1**. These results indicate that L-PFT maintains superior long-term cycling stability and electrolyte efficiency, solidifying its potential as a more reliable alternative for advanced battery applications.

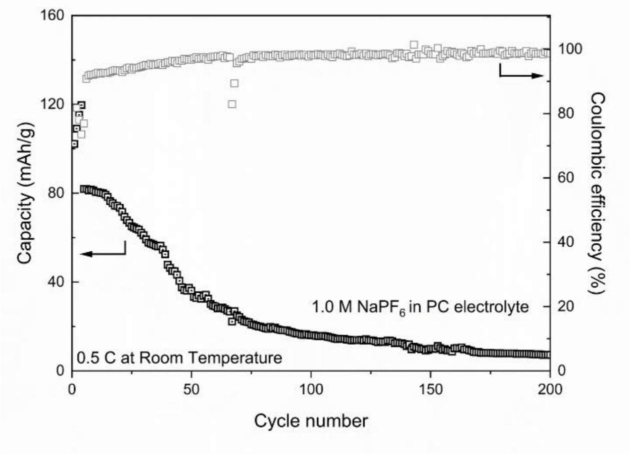

Figure 2.13 Cycling performance of the Na||FePO$_4$ cells with 1.0 M NaPF$_6$ in PC.

Table 2.1 Comparison of performance between representative reported SMBs and this work at room temperature.

Electrolyte	Current density mA g^{-1}	Retention	Capacity (mAh g^{-1})	Ref.
1 M NaClO$_4$ in PC+2% FEC	15.5	~ 54%	83	[142]
1M NaPF$_6$ in EC/DEC=1:1 vol%	15.4	90%	100	[143]
1M NaClO$_4$ in EC/DMC=1:1 vol%	15.4	90%	/	[141]
1M NaClO$_4$ in PC/FEC=98:2 vol%	7.7	88%	110	[144]
1M NaPF$_6$ in EC/DEC=1:1 vol%	20	94%	142	[145]
1M NaClO$_4$ in EC/DMC 1:1 vol%	50	/	~ 60	[146]

1M $NaPF_6$ in EC/PC=1:1 vol%	30	~87%	~ 120	[147]
1 M $NaClO_4$ in PC	20	61.1	/	[148]
1M $NaClO_4$ in EC/DEC=1:1 vol% +5 vol% FEC	20	/	~ 60	[149]
0.3 M $NaPF_6$ in PC/EC=1:1 vol%	30	/	~119 (1 st)	[60]
0.3 M $NaPF_6$ in MFE/DEC/FEC=5:4:1 vol%	10	~80%	~122	[150]
L-PFT	77 (Charge) /154 (Discharge)	92.8%	87.2	This work

The rate capability of the cells was also evaluated at different C-rates (**Figure 2.14a**). While S-PFT exhibited the best performance with high C-rates, L-PFT delivered acceptable performance. The voltage profile of Na||$FePO_4$ cells with L-PFT demonstrates stable discharge capacities of 135.5, 123.7, 109.9, 98.3, 84.7, 65.0, and 47.3 mAh g^{-1} at rates of 0.1 C, 0.2 C, 0.5 C, 1.0 C, 2.0 C, 5.0 C, and 10 C, respectively. Two voltage plateaus of the voltage profile at approximately 3.2 V and 3.25 V are observed during the charge process (**Figure 2.14b**), corresponding to the two-phase reaction from $NaFePO_4$ to $Na_{2/3}FePO_4$ and the solid solution reaction from $Na_{2/3}FePO_4$ to $FePO_4$, respectively [143,151]. During discharge process, a single plateau at 2.7 V is consistent with the results obtained from cyclic voltammetry testing (**Figure 2.12**).

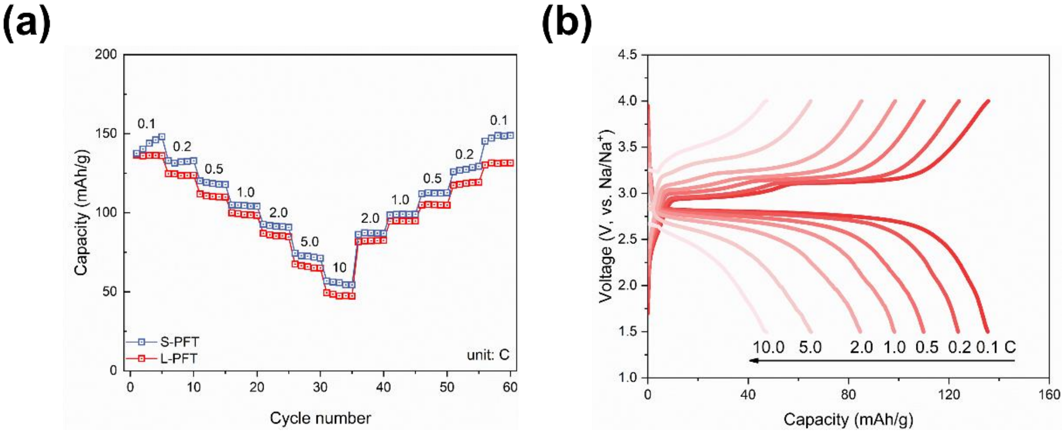

Figure 2.14 Rate performance of batteries (a) corresponding to voltage profiles with 0.3 M electrolyte (b).

It is noteworthy that the hysteresis between the charge-discharge voltage plateaus of $NaFePO_4$ is larger than that observed for $LiFePO_4$ (**Figure 2.15**), likely due to the higher energy difference during phase transitions, slower intercalation kinetics, and greater charge transfer resistance for Na^+ ions compared to Li ions. Additionally, L-PFT cells also maintained a capacity retention of 90.8% after 500 cycles at a 2 C rate, indicating that L-PFT can support long-term, high-rate cycling (**Figure 2.16**).

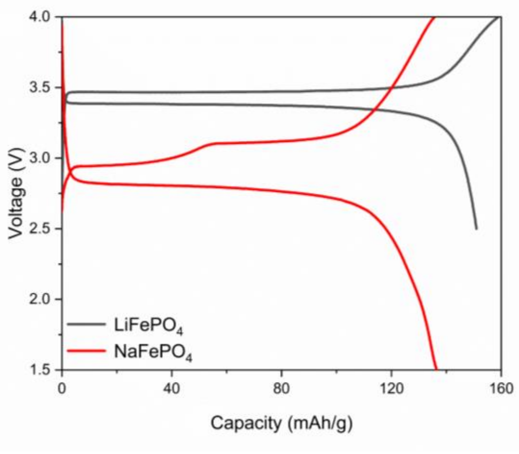

Figure 2.15 Comparison of the voltage curves between $LiFePO_4$ and $NaFePO_4$.

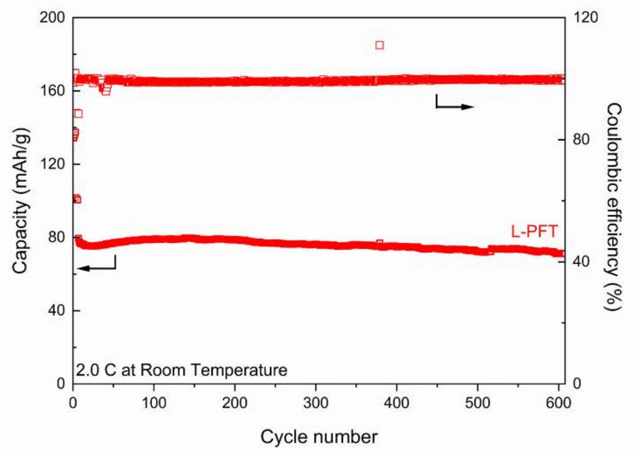

Figure 2.16 Electrochemical behavior of Na||$FePO_4$ cells with L-PFT at 2 C.

Electrode interphase evolution was investigated using electrochemical impedance spectroscopy (EIS) after extended cycling (**Figure 2.17**). The electrolyte resistance (R_s) was derived from the intercept of the high-frequency response with the real axis. Semi-circles observed at mid-to-high frequencies represent the charge transfer resistance (R_{ct}) in the electrode-electrolyte interphases and the interfacial resistance ($R_{interphase}$) of the passivation surface layer, with the total cell resistance defined as $R_{cell} = R_{ct} + R_{interphase}$ [152]. Notably, the S-PFT cell exhibited an R_s of 7.89 Ω and an R_{cell} of 152.14 Ω, whereas the L-PFT cell showed higher values, with R_s at 8.78 Ω and R_{cell} at 201.72 Ω.

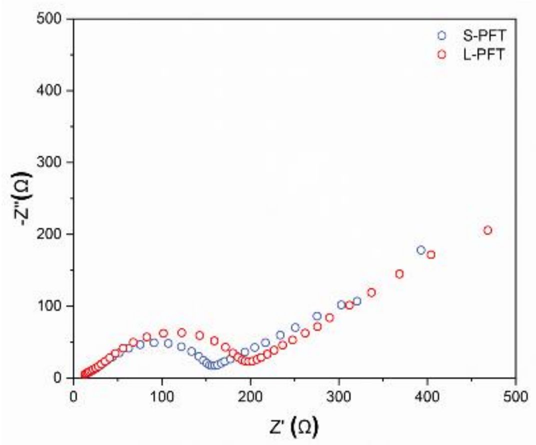

Figure 2.17 EIS results for L-PFT (0.3 M) and S-PFT (1.0 M) after long cycles.

X-ray photoelectron spectroscopy (XPS) was employed to further investigate the differences in interphase composition as shown in **Figure 2.18**. The C 1s spectrum reveals a C-C peak at 284.8 eV, indicative of conductive carbon, and a C-F peak at 291.2 eV, associated with FEC, indicating partial decomposition of FEC and its participation in interphase formation. The C–O (286.8 eV) and C=O (287.2 eV) peak in the C 1s spectrum, alongside the C=O (531.4 eV) and C–O (533.1 eV) peaks in the O 1s spectrum, are attributed to the decomposition of PC and FEC. The O 1s peak at 536.5 eV corresponds to the decomposition of $NaPF_6$, resulting in PO_xF_y species [153]. The F 1s and Na 1s spectra indicate the presence of Na-F, which is essential for interphase formation. In L-PFT cells, the peak intensities for organic components (C and O-based elements) are higher, while those for inorganic components (e.g., Na-F) are lower. In contrast, MD simulations indicate that in S-PFT cells, an elevated salt concentration results in a 22.1% increase in the CIP ratio and a 39.8% increase in the AGG ratio. This enhancement promotes greater coordination between PF_6^- and Na^+ ions, facilitating the formation of an anion-derived interphase. This configuration lowers the de-solvation energy of sodium ions and enhances Na^+ transfer through the interphase, due to the low Na^+ diffusion barrier of inorganic components, thereby improving cycling performance. These findings are consistent with the results from MD simulations, cyclic performance, and EIS measurements.

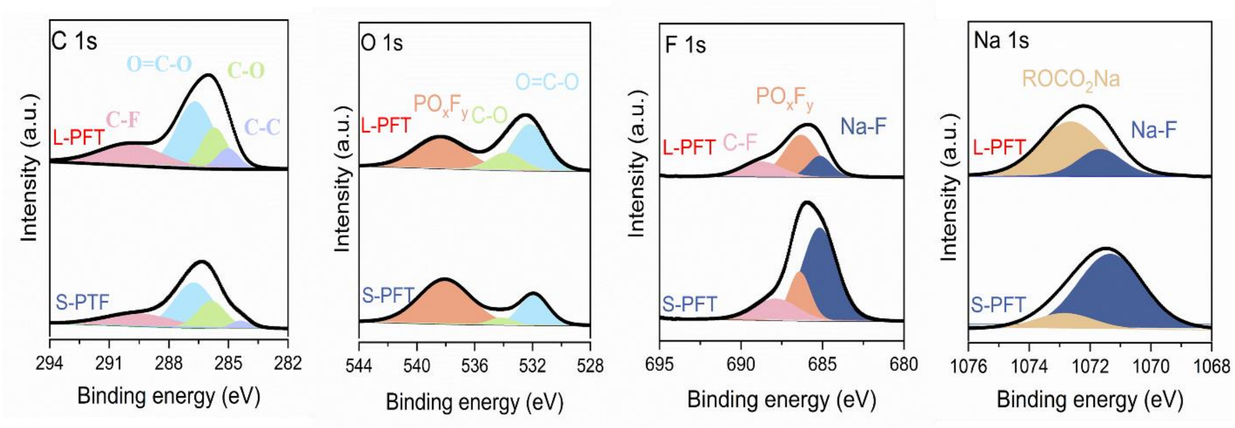

Figure 2.18 XPS spectra of cycled batteries: C 1s, O 1s, F 1s and Na 1s.

Further evidence of interphase differences was obtained by testing Na||Na symmetric cells at a current density of 1.0 mA cm^{-2} and an areal capacity of 1.0 mAh cm^{-2} (**Figure 2.19**). For the S-PFT electrolyte, the voltage hysteresis remained constant at ~70 mV after 1000 hours, attributable to the formation of an inorganic-based interphase. In contrast, L-PFT exhibited an initial overpotential of ~170 mV, which stabilized at ~100 mV after 1500 hours, with minimal fluctuations. This behavior is attributed to the formation of a flexible interphase with a low shear modulus, which can accommodate sodium metal expansion. Consequently, even when the solvent-dominated interphase is less effective at preventing dendritic growth, the voltage hysteresis remains relatively stable compared to S-PFT.

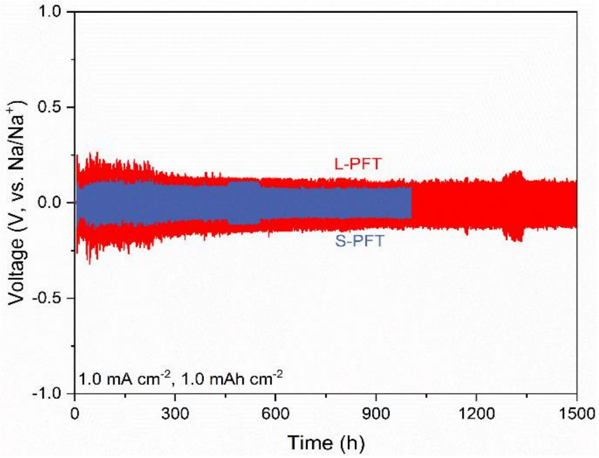

Figure 2.19 Na||Na symmetric cells using L-PFT and S-PFT electrolytes at 1.0 mA cm^{-2} with a cut-off capacity of 1.0 mAh cm^{-2}.

To demonstrate the practical applicability of L-PFT, a full cell with hard carbon pre-embedded with limited sodium was assembled, replacing sodium metal. As shown in **Figures 2.20**, a pre-cycle at 0.1 C was conducted to optimize the electrode/electrolyte interphase before long-term cycling at 0.5 C. The full cell exhibited a reversible discharge capacity of ~75 mAh g^{-1} at 0.5 C after 150 cycles. These results suggest that L-PFT is a promising electrolyte for the development of high-performance SMBs.

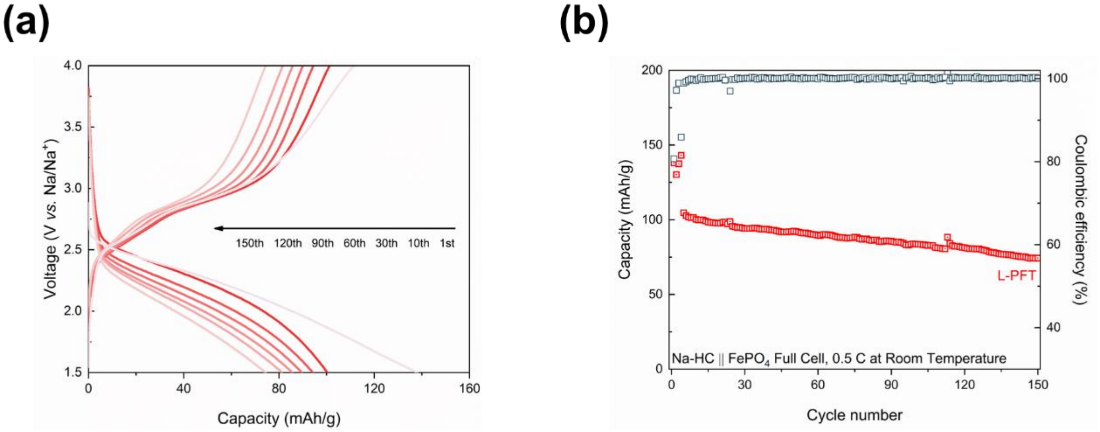

Figure 2.20 (a) Voltage profiles of Na-HC||$FePO_4$ full cells with L-PFT. (b) Cycling performance of the full cell at 0.5 C.

2.4.3 Performance of the designed electrolyte at high temperature (55 °C)

The high-temperature applicability of the designed electrolyte was investigated. **Figure 2.21a** shows a high initial coulombic efficiency using the L-PFT of ~ 72% at 55 °C, which is greater than the S-PFT (~ 68%). This result implies that there is less active Na$^+$ loss and electrolyte disintegration to generate the solid electrolyte interphase for L-PFT at the initial stage.

Furthermore, cycling instability of the S-PFT-based SMB is aggravated at high temperature (average Columbic efficiency ~ 99.24%), and the capacity retention is just 69.4% after 200 cycles at 0.5 C charge/1.0 C discharge in **Figure 2.21b**. Instead, the L-PFT can support a higher CE of 99.63% and a very stable long cycling (capacity retention ~98.5%), indicating good performance at high-temperature for L-PFT.

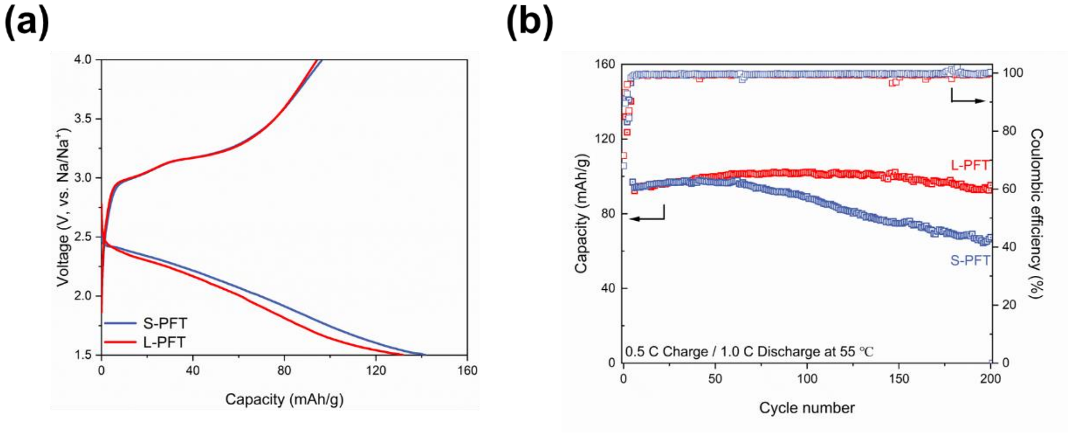

Figure 2.21 (a) Comparison for the initial cycle of L-PFT and S-PFT. (b) Cycling performance of the Na||$FePO_4$ cells with two electrolytes at 0.5 C charge/1.0 C discharge.

XPS measurements were performed to further investigate the composition change of electrode surfaces as shown in **Figure 2.22**. Although the proportion of inorganic components (Na-F) in both L-PFT and S-LFT increased significantly compared to room temperature, the increase in S-LFT was more obvious. It is generally known that during the battery cycle, HF (mainly from $NaPF_6$ decomposition) will be produced at high temperatures, which will impair battery stability [153-155]. This also explains why the capacity of a cell with L-PFT battery deteriorates at high operating temperature. EIS measurements following cycles of high temperatures are performed (see **Figure 2.23**). The S-PFT cell displays R_s (33.98 Ω). This resistance is marginally greater than that at room temperature, which can be related to the breakdown of sodium salt at elevated temperatures.

Moreover, the constant breakdown of sodium salt raises the percentage of inorganic substances in the interphase, making it more prone to breakage. Repetitive breakdown and regeneration will cause the interphase's thickness to grow, consuming electrolytes and raising the interphase's impedance until it reaches 305.1 Ω (R_{cell}). In contrast, the degradation of sodium salt is limited when compared to L-PFT, and thus the impedance change is not as significant when compared to room temperature impedance (274.9 Ω). These results suggest thermodynamic stability issue is the key factor to be considered when the SMBs are at a high operating temperature.

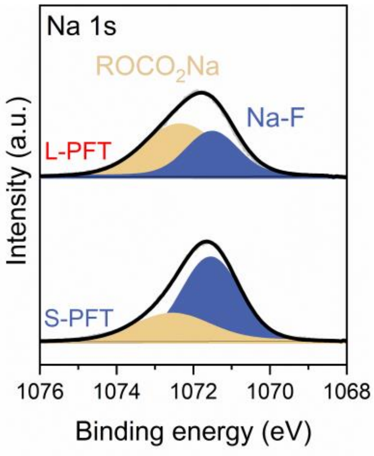

Figure 2.22 XPS spectra of cycled batteries: Na 1s.

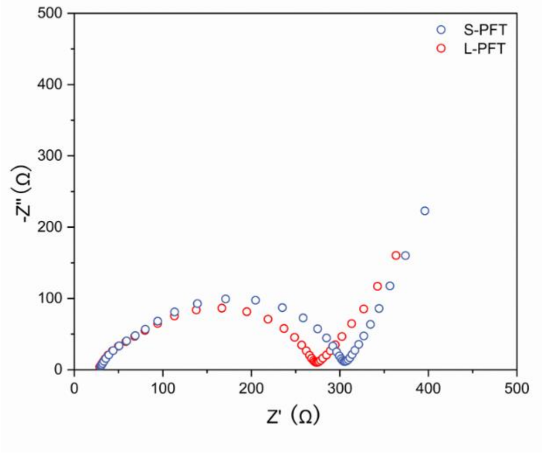

Figure 2.23 EIS results for S-PFT and L-PFT after long cycles.

2.4.4 Electrolyte performance at low temperature (-20 °C)

Given the low viscosity and high diffusion rate and better wetting performance of the proposed L-PFT electrolyte, we expect SMB based on this electrolyte to perform well at low temperatures. The expectation was supported by our test of Na||$FePO_4$ system at -20 ℃. As shown in **Figure. 2.24**, the the L-PFT battery performs well at low temperatures: it has an average CE of ~ 99% within 300 cycles at 0.2 C. However, the S-PFT battery demonstrated a somewhat steady capacity of around 65 mAh g^{-1} in the initial 200 cycles. Following this, the capacity drastically decreased after 300 cycles. There exist several reasons for this decrease in capacity.

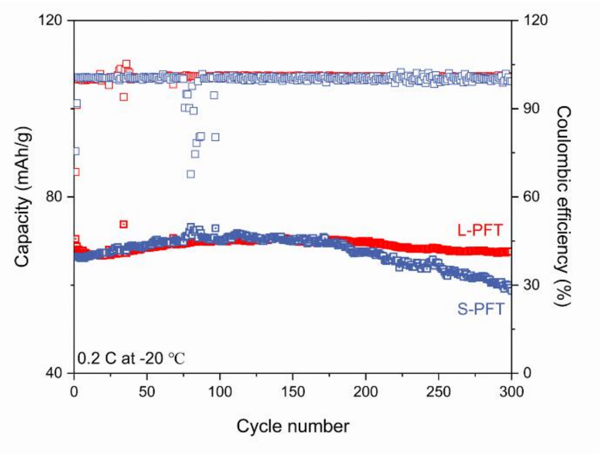

Figure 2.24 Cycling performance of the Na||$FePO_4$ cells with two electrolytes at 0.2 C.

Firstly, while charging and discharging at low temperatures, sodium metal may easily precipitate on its surface. The precipitate will then react with the electrolyte to thicken the interphase film, hence raising the interface film's resistance [156,157]. Beyond the resistance temperature change in the interphase, there will also be a noticeable rise in the charge transfer impedance [158]. The EIS test demonstrates that the internal resistance rises above and that R_s is significantly greater at low temperatures than it is at room/high temperatures (see **Figure 2.25**). Moreover, scanning electron microscopy (SEM) was utilized to examine the morphology of the $FePO_4$ cathode after cycling. As depicted in **Figure 2.26**, the surface of the $FePO_4$ cathode with S-PFT exhibited a porous and loose structure, which may contribute to increased resistance. In contrast, the cathode material in batteries with L-PFT demonstrated a relatively flat and densely packed surface morphology.

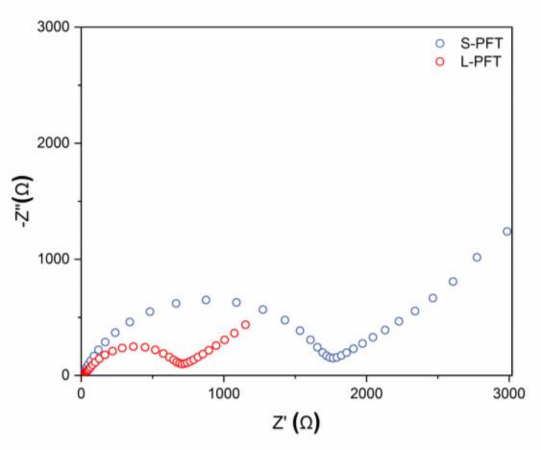

Figure 2.25 EIS results for S-PFT and L-PFT after long cycles.

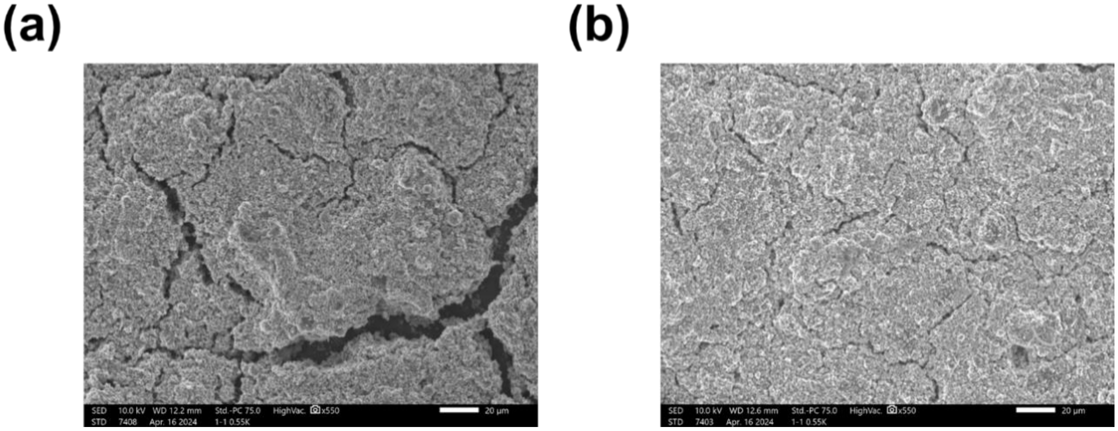

Figure 2.26 SEM images of the batteries with S-PFT (a) and L-PFT (b) morphology after cycling.

Additionally, when compared to the ratio at room temperature, we discovered that the SSIP ratio rose for both L-PFT and S-PFT, suggesting that the organic solvent phase is more tightly bound to sodium ions than the anion is (**Figure 2.27**). Notably, MD results reveal that the SSIP ratio is highest in L-PFT, reaching 62.1%, compared to 42.5% observed in S-PFT. This ratio promotes the formation of an organic interphase, which lessens the metal expansion effect caused by the rise in sodium metal.

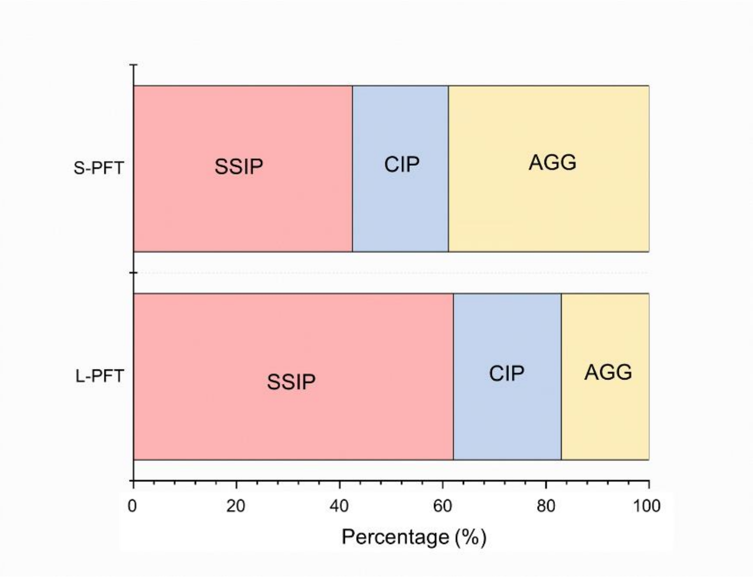

Figure 2.27 Comparison for ratio of SSIP, CIP, and AGG for L-PFT and S-PFT.

Secondly, lattice shrinkage of the $FePO_4$ also contributes to the capacity decay observed, particularly at low temperatures. To investigate this, we used XRD to examine the cathodes after charging, as shown in **Figure 2.28**. The results reveal the presence of the $NaFePO_4$ phase in both the S-PFT and L-PFT electrolytes, with a higher fraction observed in S-PFT. This finding suggests that lattice shrinkage of the cathode material under low-temperature conditions hinders the complete extraction of Na^+ ions during charging. Consequently, some sodium ions remain trapped in the cathode, further exacerbating the observed capacity decay. This behavior is more evident when Na-HC is used in place of sodium metal in full battery tests, as shown in **Figure 2.29**. Specifically, Na-HC||$FePO_4$ full cells with the S-PFT electrolyte exhibit poor capacity retention of only ~27% after 300 cycles. Moreover, a higher fraction of the $NaFePO_4$ phase is observed in full cells compared to half cells when using S-PFT. This indicates that the combination of Na-HC and the cathode material under low-temperature conditions exacerbates issues such as sodium ion trapping and incomplete extraction of Na^+ ions. These findings highlight the limitations of the electrolyte in supporting stable cycling, particularly in full-cell configurations.

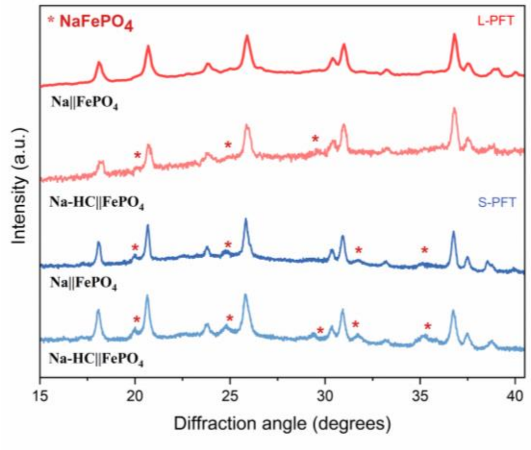

Figure 2.28 XRD patterns of Na||$FePO_4$ and Na-HC||$FePO_4$ with two electrolytes after long cycles at low temperature.

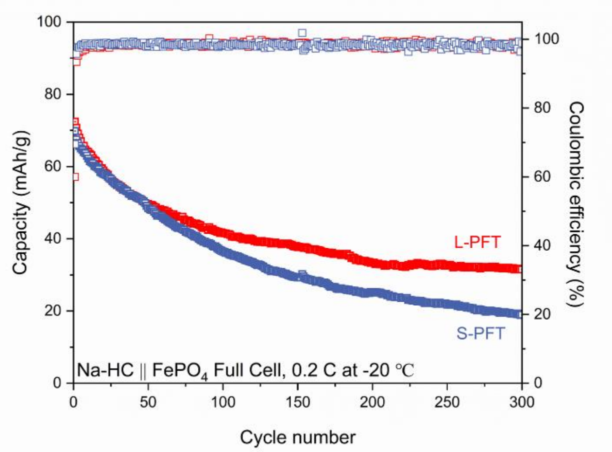

Figure 2.29 Cycling performance of the full cell at 0.2 C at low temperature.

Lastly, the reduction in conductivity, coupled with the increase in viscosity, is associated with capacity decay (**Figure 2.30**). The conductivity decreases from 3.83 mS cm^{-1} at room temperature to 2.84 mS cm^{-1} for L-PFT (3.61 mS cm^{-1} @ S-PFT). The increase in intermolecular force causes viscosity to climb to 6.72 mPa·s for L-PFT. However, S-PFT has double the viscosity of L-PFT, measuring 12.72 mPa·s. These findings imply that when an SMB functions at a low temperature, the most important component to take into account is the physical and kinetic characteristics of the electrolyte itself.

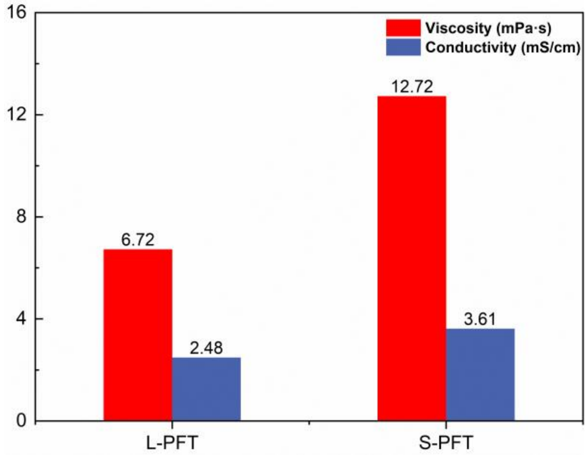

Figure 2.30 Comparison for viscosity and conductivity of L-PFT and S-PFT at low temperature.

2.5 Conclusion

In summary, our study demonstrates that sodium metal batteries (SMBs) can operate effectively with specifically designed low-concentration electrolytes, offering several unexpected advantages. In Na||$FePO_4$ cells, minimal capacity fading of approximately 0.02% per cycle was observed over 350 cycles at a 0.5 C charge/1 C discharge rate with L-PFT. Additionally, cells using L-PFT outperformed those with S-PFT at elevated temperatures (55 °C), exhibiting a higher Coulombic efficiency of 99.63% and stable long-term cycling with a capacity retention of around 98.5%. Moreover, the low viscosity, rapid ion diffusion, and enhanced wetting properties of L-PFT contributed to superior performance at low temperatures (-20 °C). These findings underscore the potential for developing high-performance SMBs through the strategic design of low-concentration electrolytes, which significantly reduce costs while maintaining robust performance across diverse temperatures.

Chapter 3 - Inhibiting Shuttle Effect and Dendrite Growth in Sodium-Sulfur Batteries Enabled by Applying External Acoustic Field

Disclosure

The major part of this chapter has been published by American Chemical Society: Qipeng Zhang, Luyu Bo, Hao Li, Liang Shen, Jiali Li, Teng Li, Yunhao Xiao, Zhenhua Tian, and Zheng Li. " Inhibiting Shuttle Effect and Dendrite Growth in Sodium-Sulfur Batteries Enabled by Applying External Acoustic Field" *Nano Lett*. 2024, **24**, 10711.

3.1 Abstract

Although electrolytes play a crucial role in enhancing the electrochemical performance and stability of sodium-based batteries, the energy density remains insufficient. To address this limitation, sodium-sulfur batteries have been explored, with sulfur selected as the active material due to its high theoretical capacity and potential to significantly improve energy density. Sodium-sulfur batteries offer several advantages, including the abundance and low cost of sodium and sulfur, as well as their environmental friendliness. Additionally, the high theoretical energy density and the ability of sulfur to undergo multi-electron redox reactions make sodium-sulfur batteries a promising candidate for large-scale energy storage However, the sodium polysulfide shuttle effect and dendritic growth pose significant challenges to its practical application. In this study, we apply diverse disciplinary backgrounds to introduce a novel method to stimulate polarized $BaTiO_3$ (BTO) nanoparticles on the separator. This approach generates more charges due to the piezoelectric effect under stronger driving forces produced by applying a controllable acoustic field at the outer edge of the cell. The acoustically stimulated BTO attracts more polysulfides, thus reducing the shuttling effect from cathode to anode and ultimately enhancing the battery performance. Meanwhile, the acoustic waves create additional streaming flows, improving the uniformity of the sodium ion dispersion, enhancing sodium ion transport, and reducing the possibility of sodium dendrite development. We believe that this work offers a new strategy for developing high-performance Na-S batteries.

3.2 Introduction

The battery industry is pursuing new energy-storage technologies beyond standard lithium-ion systems to cut costs, enhance energy density for electric vehicles, and advance renewable energy storage capabilities [159]. In the past decade, extensive research has centered on advancing Li-S batteries, motivated by sulfur's abundance and the high theoretical capacity of 1675 mAh g^{-1}. These features make Li-S batteries a strong contender for use in electric vehicles [160,161]. However, Na-S batteries are the "dream technology" in terms of sustainability and economics because of their similar chemistry, comparative cost (\$50-100 kWh^{-1}), and the abundance of sodium compared to lithium [4,83,116,117].

High-temperature sodium-sulfur batteries (HT Na-S), which utilize molten electrodes and a β-alumina solid electrolyte, have been developed for large-scale energy storage systems. However, these batteries' working temperature (300-350 °C) significantly exceeds the melting points of sodium (98 °C) and sulfur (115 °C), which raises operation and maintenance expenses as well as safety issues [32]. These drawbacks have driven interest in exploring room temperature sodium sulfur batteries (RT Na-S) for safer operation [162]. A high theoretical specific energy of 1274 Wh kg^{-1} for RT Na-S has been reported since 2006 [163]. However, some technical issues, such as self-discharge, limited cycle life, and low active material usage rate, hinder its growth. In addition, the poor compatibility between sulfur cathode and electrolytes results in the high solubility of sodium polysulfide intermediates (NaPSs), particularly in ether-based electrolytes. As a result, sodium polysulfides shuttle to the sodium anode, leading to the loss of active substances, deterioration of interface, rapid capacity decay, and low Coulombic efficiency (CE) [32,85,164]. At the anode, on the other hand, the inhomogeneous growth and deposition of sodium dendrites pose significant safety issues, low CE, and poor cycle life [115,165]. These challenges have greatly limited the practical applications of RT Na-S batteries.

To address these challenges, researchers have discovered compositing carbon-based hosts with sulfur and electrolyte modification [166-169]. For instance, Pint et al. constructed a microporous confinement cathode using the processing of sucrose [170]. The polysulfide shuttle on the cathode was reduced by the restraint method, which delivered more than 300 mAh g^{-1} at 1 C. Wang et al. formulated “cocktail optimized” electrolyte system that combined carbonate electrolytes, highly concentrated sodium salt, and indium triiodide as an additive [162]. This tailored electrolyte in the Na-S batteries exhibited outstanding performances with a specific capacity of 1170 mAh g^{-1} at 0.1 C.

In addition to the methods mentioned above, since the strong bonding affinity between anions/cations and polysulfides effectively inhibits the shuttle effects, it has been demonstrated that filling metal materials- such as oxides, sulfides, nitrides, and carbides - as well as their heterostructures composited with separator or cathode, can serve as polysulfide traps [171-173]. Among these materials, the improved additive $BaTiO_3$ (BTO) has gained increasing interest due to its potential to capture more polysulfides through ferroelectric effects [174,175]. Wei et al. proposed a composite C/S cathode incorporating ferroelectric BTO materials, suggesting that BTO spontaneously polarizes under the action of an internal electric field. This polarization carried an electric charge on the surface that can absorb polar polysulfides. The cell has a discharge capacity of 835 mAh g^{-1} after 100 cycles, which is higher than its C/S equivalent without BTO [176]. Chen et al. demonstrated that using a defective ferroelectric B-BTO as a multipurpose sulfur immobilizer improves Li-S battery performance. The shuttle effect is both electrostatically and chemically constrained due to the inherent ferroelectricity of B-BTO and the chemical interactions between B-BTO and polysulfide molecules [177]. The shuttle effect can be mitigated more effectively by leveraging the spontaneous polarization of BTO induced by ferroelectric action. This approach is particularly effective in Li-S systems with additives such as $LiNO_3$, however, it remains inadequate for Na-S systems, where the uncontrollable shuttle effect of sodium polysulfide is further exacerbated by the significantly higher solubility of higher-order NaPSs compared to the lithium polysulfide system during the multistep reaction process. This increased solubility of sodium polysulfide leads to a reduced cycling life [178,179]. Additionally, sodium dendrites exhibit lower chemical stability compared to lithium dendrites, making it more difficult to find solutions to these combined issues.

Beyond the ferroelectric properties of BTO, the asymmetric crystal structure of BTO leads to a change in the distribution of positive and negative charges within the crystal when subjected to external mechanical stress, known as the piezoelectric effect. This change can be modified based on the intensity of the applied driving force. Consequently, the BTO's piezoelectric action generates more polarization than the previously discussed ferroelectric effect. Based on this principle, it is feasible to apply an externally controllable field to the battery, inducing BTO to generate additional charges under stronger driving forces through the piezoelectric effect. This approach can attract more sodium polysulfides, thereby enhancing the electrochemical performance of the system using a common ether electrolyte without the additives.

In this chapter, building on diverse disciplinary expertise, we propose the use of BTO nanoparticles coated onto commercially available glass fiber (GF) separators by a straightforward drop-coating procedure. To make the effect more obvious, we pre-polarize the BTO. When exposed to an external acoustic field, the driving force stimulates the polarized BTO, resulting in an increased charge accumulation on the surface of the BTO nanoparticles due to the piezoelectric effect. This process enables BTO to absorb more sodium polysulfides and lessen the shuttling effect, enhancing the capacity of the Na-S battery to reach 300 mAh g^{-1} after 50 cycles compared to zero without acoustic waves. Additionally, to our surprise, the sodium metal anode was further stabilized by applying an external acoustic field compared with the base one by testing symmetric Na-Na cell and long cycle Na-Cu cell. Finite element simulation indicates that the mechanical waves generated cause the electrolyte flow, improving sodium ion diffusion and lowering the likelihood of sodium dendrite formation in the sodium ion consumption region, thus stabilizing battery performance.

3.3 Experimental section

3.3.1 Preparation of the BTO-contained separator

To prepare the BTO-contained separator, 1 g $BaTiO_3$ (BTO) nanoparticles (US Research Nanomaterials, Inc) was dispersed in 20 mL N-methyl-2-pyrrolidone (NMP) using a high-speed mixer at room temperature for 12 h. The BTO dispersion was then dropped in the glass fiber membrane separators (Whatman GF/A) and dried under vacuum overnight. The loading amount of the BTO particles was ~ 0.6 mg cm^{-2}.

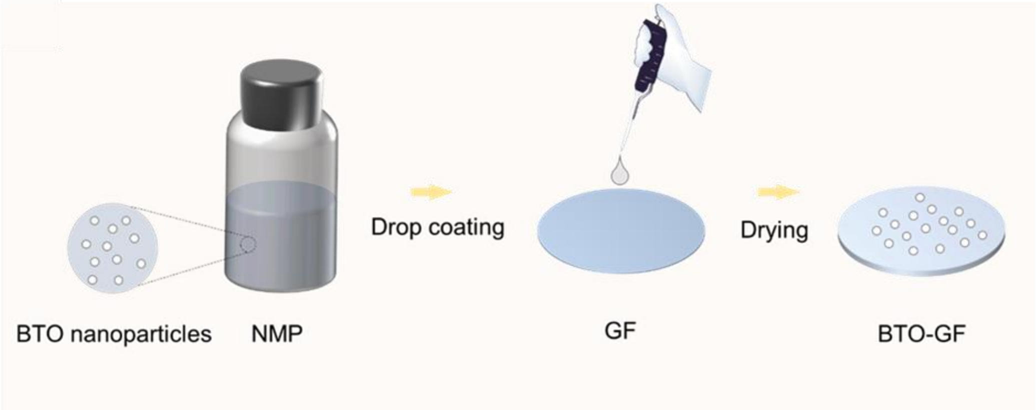

Figure 3.1 Schematic illustration on the preparation procedure of the BTO-coated separator by a drop coating process.

3.3.2 Preparation of the cathode

The sulfur/carbon (S/C) composite was prepared following a melt-diffusion strategy through mixing sulfur powder and mesoporous carbon powder (CMK-3, Xfnano, Inc.) in the weight ratio of 3:1, followed by heating the S/C mixture in a sealed vessel at 155 °C for 12 h under vacuum. The battery electrode slurry consists of S/C composite, Super P, and polyvinylidene fluoride (PVDF) binder with a mass ratio of 8:1:1 in NMP solvent. Then homogeneous slurry was cast onto the aluminum foil. All of the cathodes were dried at 60 °C in a vacuum for 12 h. The sulfur mass loading was about 1.0 mg cm^{-2}.

3.3.3 Cell assembly and electrochemical testing

Electrochemical tests were performed using CR2032-type coin cell with sodium metal as the anode, BTO-contained membrane as the separator, the S/C composite as the cathodes, and 1.0 M bis(trifluoromethane)sulfonimide sodium salt (NaTFSI, Alfa Aesar) in tetraethylene glycol dimethyl ether/1,3-dioxolane (TEGDME/DOL, 1:1 vol %) as the electrolyte. TEGDME and DOL were dried by 3 Å molecular sieves for over two weeks. Each cell contained 80 µL of electrolyte. The Na-S cells were galvanostatic cycled between 1.0 and 2.8 V on a LAND test system (Wuhan LAND Electronics Co., Ltd.) at room temperature (~ 26 °C). The cells were cycled at 0.1 C (1 C = 1675 mA g^{-1}). For Na-S cells with acoustic field, we apply two parallel transducers to the cell case, which form stable acoustic field.

Na-Na symmetric cells were tested at a current density of 0.1 mA cm^{-2} with a fixed areal capacity of 0.1 mAh cm^{-2}. The coulombic efficiencies of Na depositing/stripping were investigated via Na-Cu coin cells in corresponding electrolytes at a current density of 0.1 mA cm^{-2} with a fixed areal capacity of 0.1 mAh cm^{-2} using the method described by Zhang et al. [180] Plating a specific amount of Na metal onto a Cu substrate which is initially devoid of Na (represented by Q_p), Na metal is then stripped from the Cu substrate until a cut-off voltage of + 1 V (shown by Q_s). The average CE over n cycles can be calculated as:

$$CE_{avg} = \frac{1}{n} \sum \frac{Q_s}{Q_p} \tag{3-1}$$

EIS measurements were performed Bio-Logic SP-150 potentiostat. All Na-S cells were measured using a 5-mV amplitude over the frequency ranging from 100 kHz to 10 mHz.

3.3.4 NaPSs permeability tests

A volume of 5 mL of electrolyte was contained in an H-cell, and 5 mL of the NaPSs solution was contained in the other side. The NaPSs solution was prepared by adding S and sodium sulfide (Alfa Aesar) in electrolyte. A divider that was placed in between the two bottles served as their connection. The 24-hour monitoring of NaPSs migration.

3.3.5 Material characterization

Structural characterization of BTO and BTO-contained separator were conducted by a Rigaku SmartLab XRD instrument using Cu Kα radiation. SEM were performed on a FEI Quanta 600 FEG environmental scanning electron microscope. To examine the elemental composition and distribution on the separator surface, EDX mapping images were also obtained. The composition of the interphase layer was examined using X-ray photoelectron spectroscopy (XPS, PHI Quantera SXM).

3.3.6 Finite element simulation

Simulations were performed using the finite element method (FEM)-based software, COMSOL Multiphysics. Our model was established according to the 3D schematic of the device containing a battery, a silica glass, and an acoustic transducer. The piezoelectric module was applied to the separator (i.e., containing BTO), and the fluid domain (i.e., electrolyte) was simulated with the pressure acoustics module. The circular region (radius, 11.5 mm) at the bottom of the silica glass was set to the “boundary load” condition, and the remaining boundaries were set to the “free load” condition. Then, the model was solved through COMSOL’s frequency domain analysis to obtain the displacement on the battery’s surface, the electrical potential on the surface of the separator, and the pressure in the fluid domain.

In order to simulate the streaming pattern in the fluid domain, the laminar flow physics module was used. The body force stemming from acoustic pressure was calculated based on the simulated acoustic pressure. The no-slipping condition was set to all boundaries surrounding the fluid domain. Then, the model was solved by a “stationary” solver to obtain the streaming velocity in the electrolyte [181,182].

3.4 Results and discussion

3.4.1 Comparison of piezoelectric and ferroelectric effects

To examine the differences between piezoelectric and ferroelectric effects, we investigated two distinct crystal systems of BTO under an applied disturbance (**Figure 3.2**). For the cubic phase of polarized-BTO, where the material only exhibits piezoelectric behavior, the polarization generated is solely a result of the piezoelectric effect. Upon applying a disturbance, the resulting polarization leads to a measured amplitude of approximately 10.8 mV. This amplitude directly corresponds to the material's response due to piezoelectricity, given the absence of ferroelectricity in the cubic crystal structure.

In contrast, the tetragonal phase exhibits both piezoelectric and ferroelectric properties. In this case, the polarization is a superposition of both effects, which results in an amplitude of about 11.6 mV. This increase in amplitude reflects the combined contributions of both piezoelectric and ferroelectric phenomena in the tetragonal system.

The comparison of these two amplitudes highlights a key observation: the polarization produced by piezoelectricity in the polarized BTO is significantly larger than that produced by ferroelectricity. This suggests that, although ferroelectricity contributes to the overall polarization in the tetragonal phase, the piezoelectric effect remains the dominant mechanism, especially when comparing the cubic and tetragonal phases of BTO.

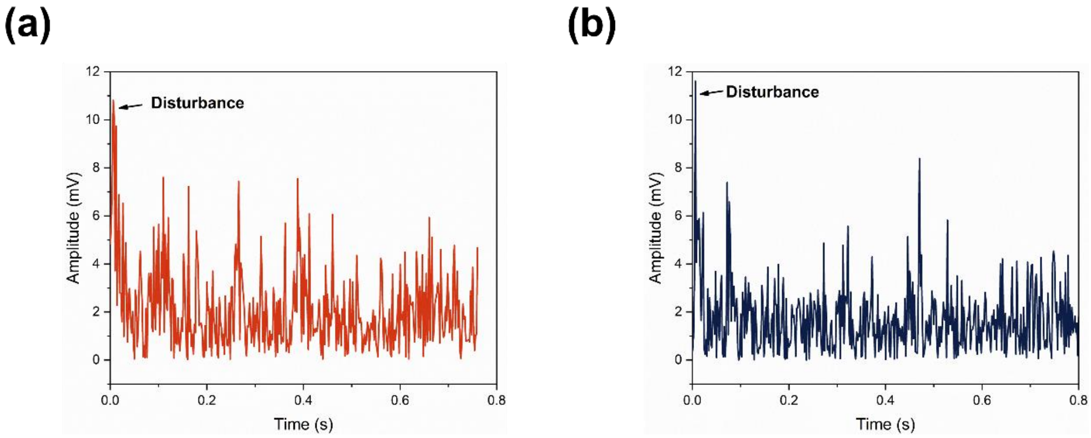

Figure 3.2 Comparative analysis of BTO nanoparticle polarization. (a) Cubic and (b) Tetragonal.

3.4.2 The effect of acoustic waves on the stability of Na-S battery

Figure 3.3a depicts the X-ray diffraction (XRD) patterns of pure BTO, GF, and the polarized BTO-coated separator (referred to as BTO-GF). A broad band around 25° is observed, corresponding to the GF. The cubic (*Pm3m*) crystal system in which the XRD pattern for pure BTO is indexed in good accordance with those described in the literature [183]. After the dropping and pre-polarized process, no detectable impurities or new peaks were detected in the BTO-GF samples, indicating that the crystal system of BTO remains unchanged during this process. Additional SEM analysis of the BTO-GF after the dropping display a 2-μm thick GF with a homogeneous distribution of BTO nanocrystals (**Figure 3.3b**).

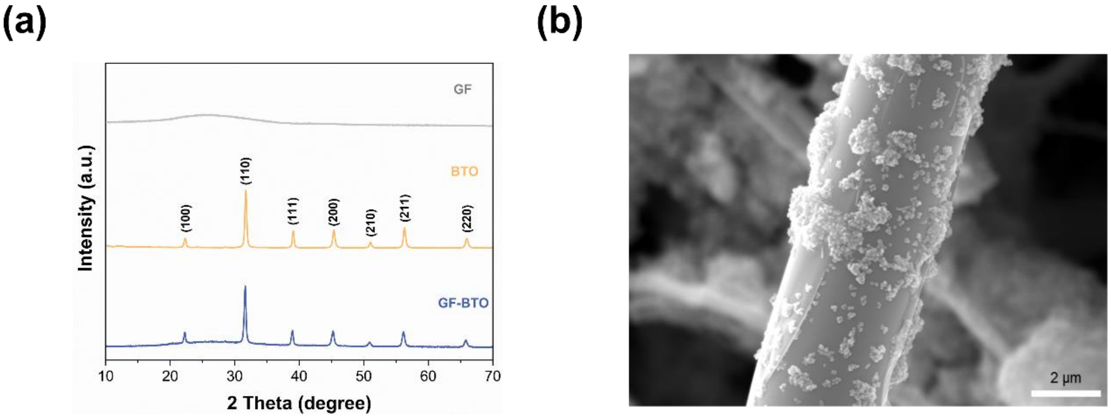

Figure 3.3 (a) XRD pattern of GF, BTO, and GF-BTO. (b) SEM images of the BTO-GF.

To verify the impact of acoustic waves on mitigating the NaPSs shuttling issue and enhancing battery stability, Na-S cells were assembled and cycled both with and without acoustic field. We created a small-sized acoustic device to oscillate the battery. The device was made by a transducer and attached to the anodal with a glass slide. The transducer could generate the 22 kHz sine wave, and the duty cycle was 50% (**Figure 3.4a**). The vibration's amplitude at this frequency is 0.5408 nm, which agrees with the computation (**Figure 3.4b-c**).

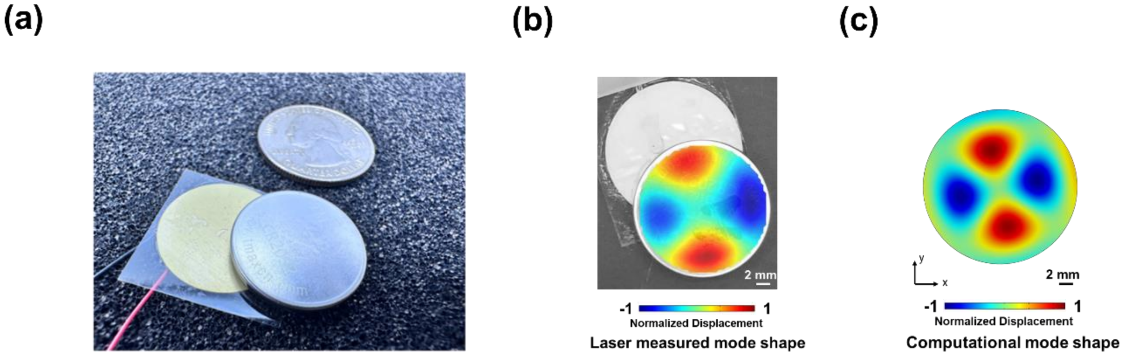

Figure 3.4 (a) Photo of the test setup with a piezoelectric transducer and a battery bonded on a glass wafer. (b) Laser measured mode shape of battery. (c) Computational mode shape of battery.

The results of Na-S battery are shown in **Figure 3.5**, where two voltage plateaus are observed during the discharge process for both types of cells. The higher voltage plateau, around 2.2 V, corresponds to the solid-liquid transformation from S to long-chain polysulfide Na_2S_8. The lower plateau, at approximately 1.6 V, represents the conversion from soluble Na_2S_4 to insoluble Na_2S_x ($x \leq 3$), a typical "solid-liquid-solid" conversion [89]. For the charge curve, however, they are quite different. An undesirable lengthy charging platform at about 2.2 V is noticed after the acoustic field is turned off. This is a sign of a significant NaPSs shuttling that leads to low reversibility and capacity deterioration [184]. Therefore, the cell without acoustic field displays poor discharge capacity dropping rapidly to almost zero after 10 cycles. In contrast, the cell with acoustic waves exhibits a complete charging curve, with two platforms at ~ 1.8 V and 2.2 V, corresponding to the conversion from lower-order to higher-order polysulfide, consistent with previously reported literature [89]. The battery delivers a capacity of around 300 mAh g^{-1} after 50 cycles in the absence of additives, demonstrating a significant reduction in the shuttling effect and a clear improvement in both longevity and reversible capacity.

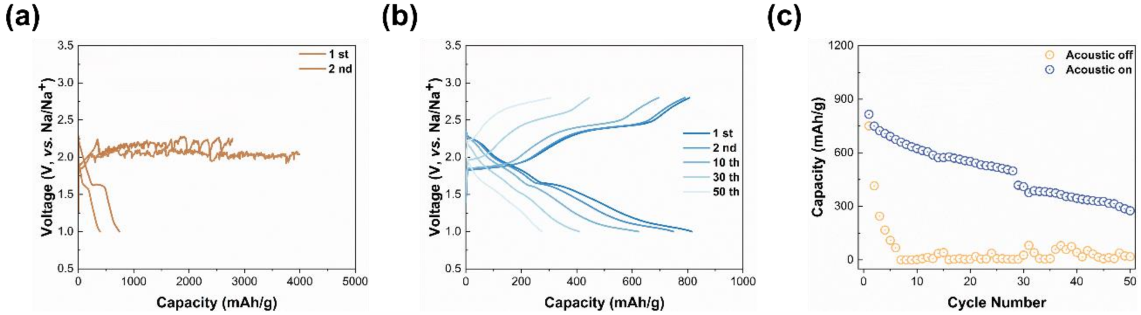

Figure 3.5 (a) Voltage profiles of Na-S cells without acoustic field. (b) Voltage profiles of Na-S cells with acoustic field. (c) Cycling performance of the Na-S cells w/o acoustic field.

Additionally, XPS and EIS measurements were provided more evidence of decreased capacity from different perspectives, as shown in **Figure 3.6** and **Figure 3.7**. In the XPS testing, the Na-F peak at 683.2 eV, a crucial composition of the interphase layer, was observed under both battery conditions in the F 1s spectrum [123]. However, a new peak corresponding to the TFSI anion signal at 687.8 eV emerged in the absence of an external acoustic field [184]. This is likely due to the decomposition of sodium salts after numerous cycles, resulting in a reduction in capacity. Contrarily, the interphase layer composition under the application of an acoustic field revealed only one peak, showing that the external acoustic field could increase stability during cycling. Furthermore, the EIS measurements of cells with the acoustic field show lower interfacial resistance, with R_f and R_{ct} values of 254.6 Ω and 768.1 Ω, respectively, compared to the cell without acoustic field, which exhibit R_f and R_{ct} values of 436.9 Ω and 1637 Ω after 50 cycles.

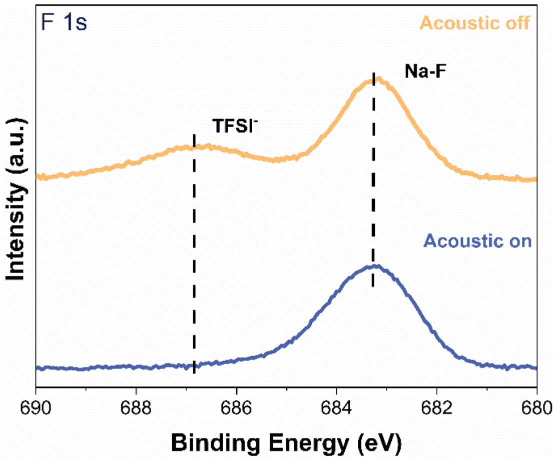

Figure 3.6 XPS spectra of cycled cell with and without acoustic field.

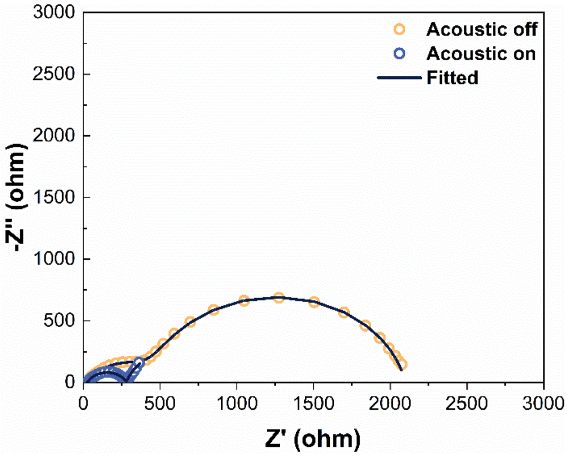

Figure 3.7 Electrochemical impedance spectroscopy (EIS) of Na-S cells with/without acoustic field after 50 cycles.

SEM characterization and corresponding elemental mapping of BTO-GF and based-batteries after 50 cycles were tested to provide further evidence supporting the previously discussed results. As shown in **Figure 3.8**, when the acoustic field is turned off, only a minor portion of sodium polysulfide is captured, indicating that the shuttling effect cannot be fully suppressed. However, as the electrochemical reaction proceeds, most sodium polysulfides are trapped on the glass fiber separator, suggesting that more sodium polysulfides are attracted to the BTO in the presence of an acoustic field.

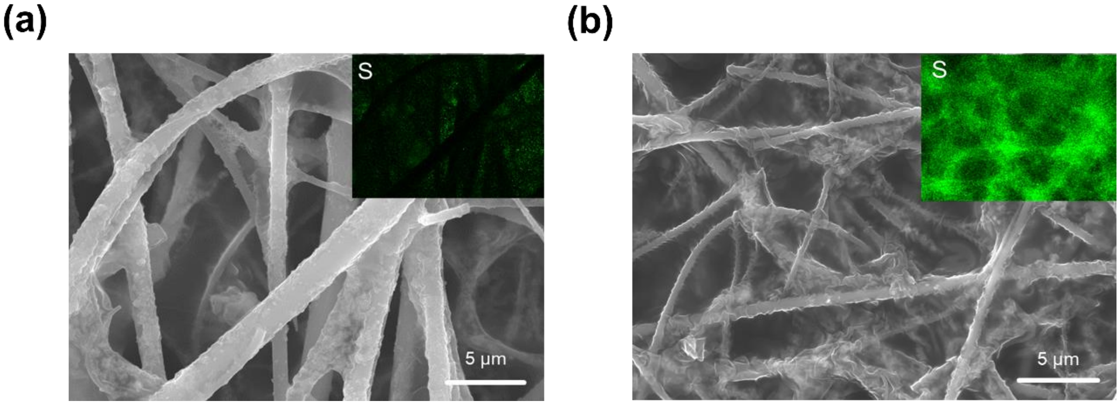

Figure 3.8 (a) SEM image of the cells without acoustic wave. (b) SEM image of the cells with acoustic wave.

Furthermore, the color changes observed in the sodium metal anode corroborate the SEM findings. We observe that when the acoustic field is turned off, the majority of sodium polysulfides are deposited on the surface of the sodium metal through the glass fiber separator, leaving only a small amount on the separator itself. This deposition turns the surface of the sodium metal yellow, as shown in **Figure 3.9**. In contrast, the sodium metal in the battery exposed to the acoustic field retains a dull white color. This suggests that the acoustic field effectively inhibits the diffusion of sodium polysulfides to the anode side, as a significant amount of polysulfides are trapped within the BTO-GF separator.

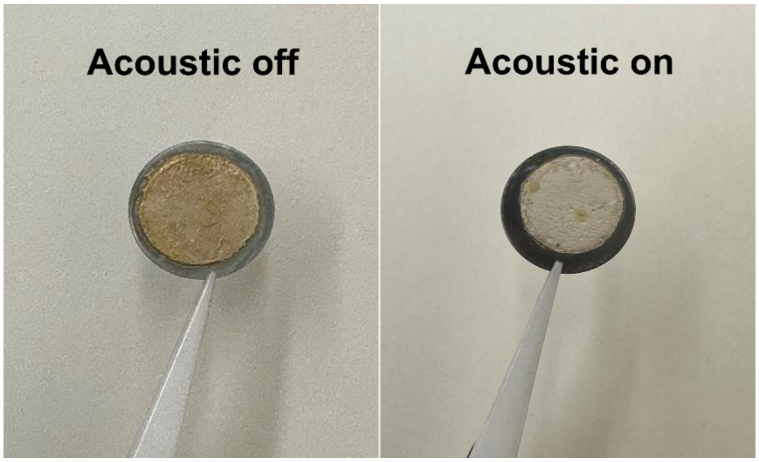

Figure 3.9 Photo images comparing the sodium anodes without (left) and with (right) acoustic field.

To directly identify the diffusion of soluble NaPSs in the presence or absence of an acoustic field, the permeability of NaPSs through a BTO-modified glass fiber separator was monitored by tracking color changes, as illustrated in **Figure 3.10**. In the container without an acoustic field, significant migration of NaPSs to the opposite side is observed. After one hour, sodium polysulfide diffuses across the container and settles at the bottom. By 24 hours, the NaPSs have fully migrated to the other side. In contrast, under an acoustic field, no NaPSs migration is detected within the first hour. Only partial transfer of NaPSs is observed between 2 to 6 hours. Only approximately half of the NaPSs have migrated to the opposite side after 24 hours. This shows that the container with an acoustic field effectively inhibits NaPSs diffusion.

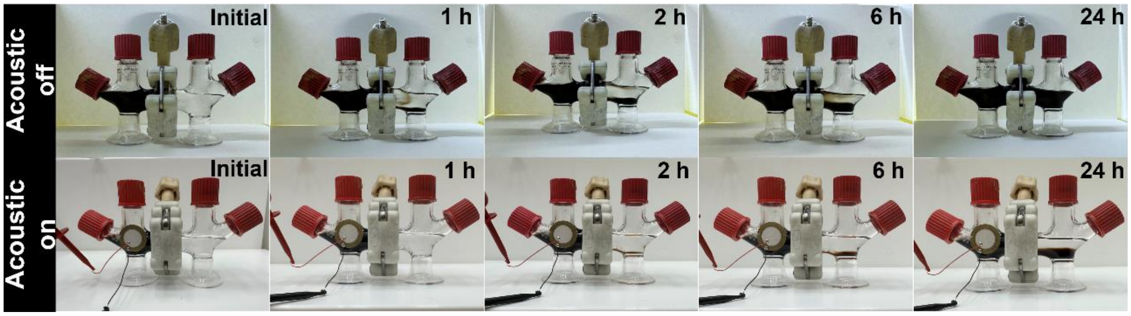

Figure 3.10 Visual observation of NaPSs diffusion for battery w/o acoustic field.

In addition, visual observation of NaPSs diffusion in the acoustic field using a GF without BTO was also conducted, as shown in **Figure 3.11**. Upon initial activation of the acoustic field, no migration of sodium polysulfide is observed. However, after one hour, NaPSs begins to diffuse to the opposite side and settle at the bottom. By the two-hour mark, approximately half of the NaPSs have migrated to the other side, and by ten hours, complete transition is achieved. This rate of transition is notably quicker than in scenarios where BTO is present, highlighting that the acoustic field alone cannot halt the diffusion of sodium polysulfide.

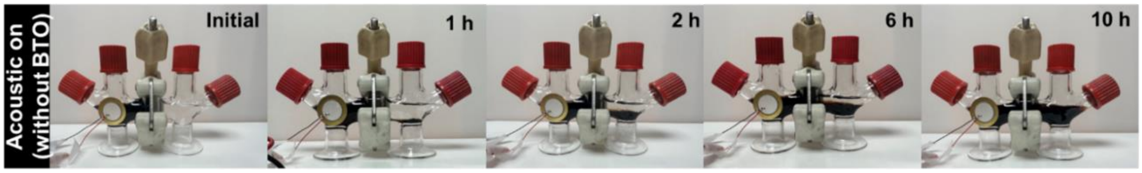

Figure 3.11 Visual observation of NaPSs diffusion for battery in the acoustic field using GF without BTO.

Finite element simulation was employed to comprehend why the majority of NaPSs are inhibited in the presence of an external acoustic field. The cathode and anode were located on either side of the separator and the electrolyte (**Figure 3.12a**). An effort was made to match the vibrometer readings by modeling the boundaries at the acoustic transducer region as required displacement. With this model, we obtained the battery's deformations at various eigenfrequencies by providing an oscillating excitation signal to the transducer. Our findings are consistent with the experiment (**Figure 3.12b**). Although the polarized BTO has a piezoelectric effect in the absence of an acoustic field, it is unable to produce a larger field force due to the formation of a weak composite field as shown in **Figure 3.12c**. In contrast, when present in an external acoustic field, BTO nanoparticles are more polarized under stronger driving forces produced by coupled field, leading to the generation of more charges on the surface, which makes more NaPSs readily are adsorbed, thus suppressing the shuttle effect and eventually enhancing performance as shown in **Figure 3.12d**.

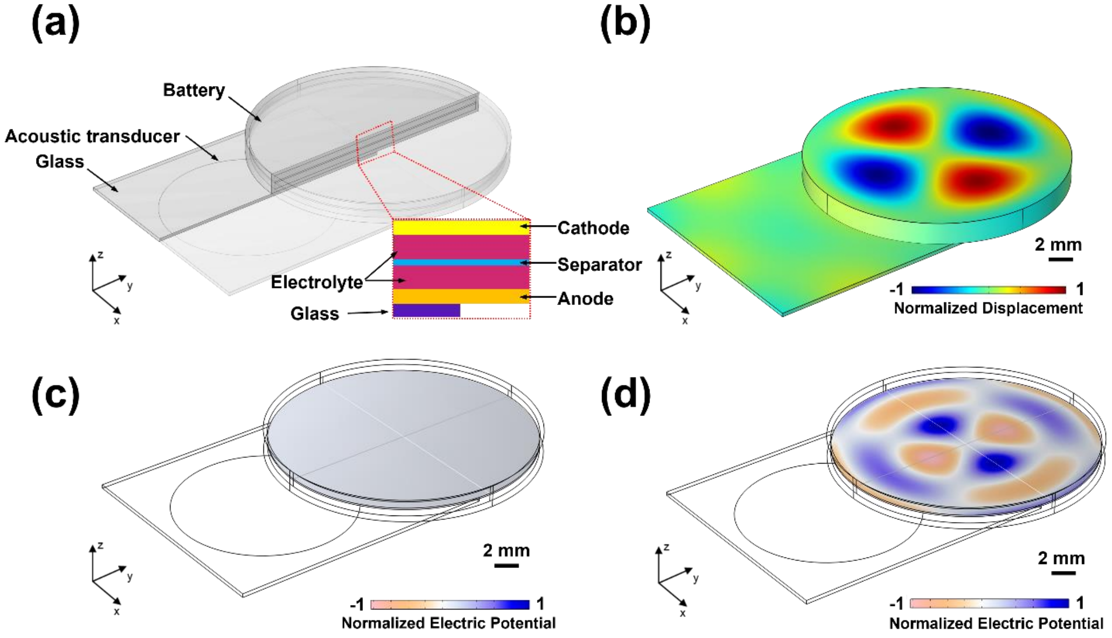

Figure 3.12 (a) 3D skematic of the battery model for finite element simulations. (b) Simulated mode shape of a cell. (c) Simulated electric fields for cases without acoustic wave. (d) Simulated electric fields for cases with acoustic wave.

3.4.3 Suppressing dendrite growth for sodium metal anode.

While exploring the effect of the acoustic field on the sulfur cathode, a preliminary evaluation was also conducted to assess the impact of acoustic waves on the sodium metal anode. Although the research is not yet comprehensive, some initial observations are worth discussing. The average Na plating/stripping coulombic efficiencies of Na-Cu and longer cycle life of Na-Na symmetric cells were evaluated on the impact of acoustic field on Na anode. As demonstrated in **Figure 3.13a**, drastic side reactions on the sodium anode surface result in a low average coulombic efficiency (CE_{avg}) of 61.57% in the absence of acoustic waves and additives. In contrast, when the acoustic field was applied, the CE_{avg} improved to 76.84%, suggesting that the acoustic field enhances sodium plating/stripping behavior. Furthermore, the Na ion nucleation overpotentials were assessed (**Figure 3.13b**). Without the acoustic field, the nucleation overpotential was 158.1 mV. In contrast, a much lower nucleation overpotential of 67.6 mV was observed with the acoustic field, further indicating the improved sodium plating/stripping.

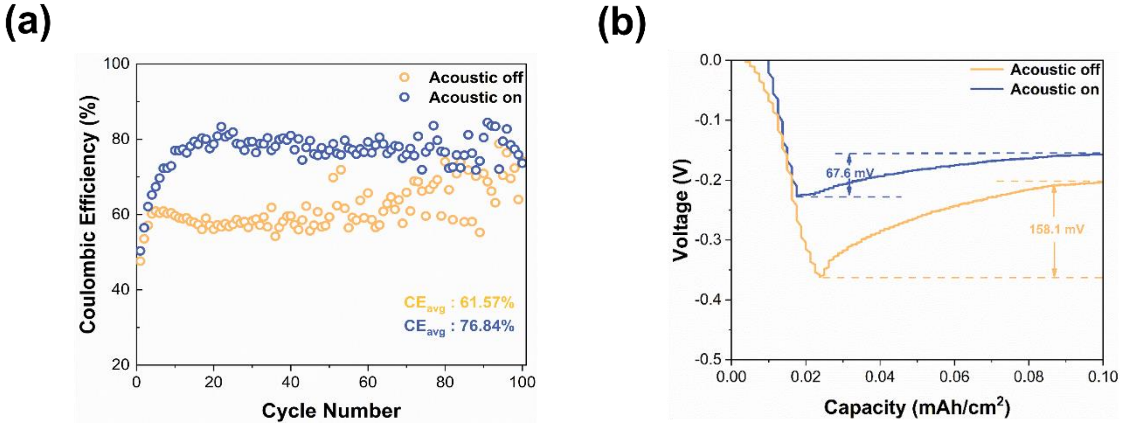

Figure 3.13 (a) Na-Cu cells using BTO-GF w/o acoustic field. (b) Comparison of the nucleation overpotentials for Na-Cu cells batteries w/o acoustic field.

The long-term cycling performance of Na-Na cells was tested to further evaluate the reversibility of sodium plating and stripping at a current density of 0.1 mA cm^{-2} and an areal capacity of 0.1 mAh cm^{-2} (**Figure 3.14a**). Cells without the acoustic field exhibit generally gradual increase in overpotentials with cycling time, reaching the cut-off voltage of 250 mV at 250 h, which is lower than those with cells using regular glass fiber separators (**Figure 3.14b**). This difference may be attributed to the inherent piezoelectric properties of BTO, as the field generated by BTO can inhibit dendrites growth [185]. In contrast, the voltage hysteresis of the cell with an acoustic field is further reduced and stabilized at around 110 mV without noticeable variations.

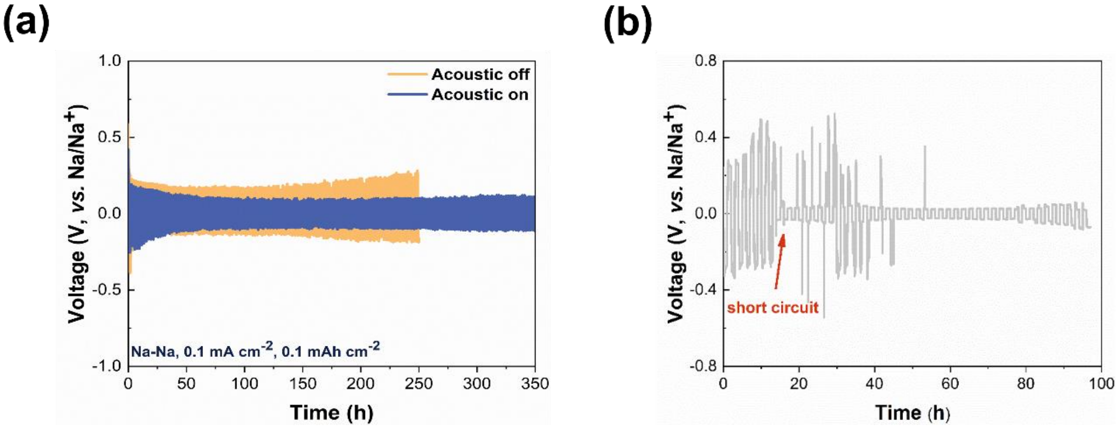

Figure 3.14 (a) Voltage profiles of Na-Na symmetric cells w/o acoustic field. (b) Voltage profiles of Na-Na symmetric cells using regular GF.

We also employed finite element simulation to provide an explanation by which the external acoustic field influences the stability of sodium. In the absence of an acoustic field, inadequate diffusion leads to the uneven distribution of sodium ions within the anode, resulting in the irregular formation of sodium dendrites. These dendrites generate a strong electric field, which attracts additional sodium ions with each cycle, further accelerating their growth, as seen in **Figure 3.15** [186].

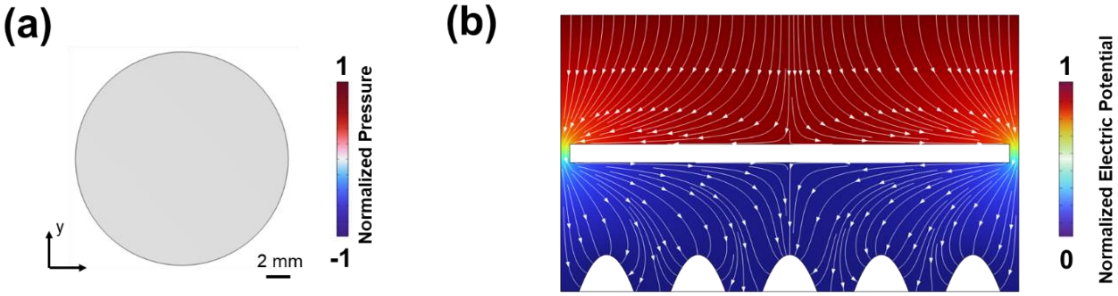

Figure 3.15 (a) Simulation result for the battery when acoustic waves are off. (b) Simulated electric field distribution in a region near the sodium dendrite when acoustic waves are off.

However, the addition of an acoustic field can create an additional flow field, which provides an extra drive force (**Figures 3.16**), causing the electrolyte to flow. In order to simulate the acoustic streaming, the continuity and the Navier-Stokes equations are used, expressed as follows [187,188]:

$$\rho_0 \nabla \cdot \mathbf{v} = 0 \tag{3-2}$$

$$\rho_0 (\mathbf{v} \cdot \nabla)\mathbf{v} = -\nabla p + \mu \nabla^2 \mathbf{v} + \left(\mu_b + \frac{1}{3}\mu\right) \nabla(\nabla \cdot \mathbf{v}) - \mathbf{F} \tag{3-3}$$

where ρ_0 is electrolyte density, $\boldsymbol{v}$ is streaming velocity, p is pressure, μ, μ_b are shear and bulk dynamic viscosities, respectively, and $\boldsymbol{F}$ is the body force, which can be expressed as [189]:

$$\mathbf{F} = -\frac{\Gamma_{\mathrm{f}} \omega}{2 c_{\mathrm{f}}^2} \operatorname{Re}\left(p_1^* \mathbf{v}_1\right) \tag{3-4}$$

where Γ_f is damping coefficient, ω is angular frequency, c_f is the sound speed, p_1 represents acoustic pressure, and $\boldsymbol{v}_1$ is the acoustic velocity. Numerical simulations were performed using the commercial finite element software COMSOL Multiphysics. The flow rate obtained based on our simulation is around 300 μm s^{-1}, which is often higher than the electrolyte flow rate in the porous electrode [190]. The presence of flow rate enables more effective transport of sodium ions within the designated depletion zone, thereby slowing the formation of sodium dendrites.

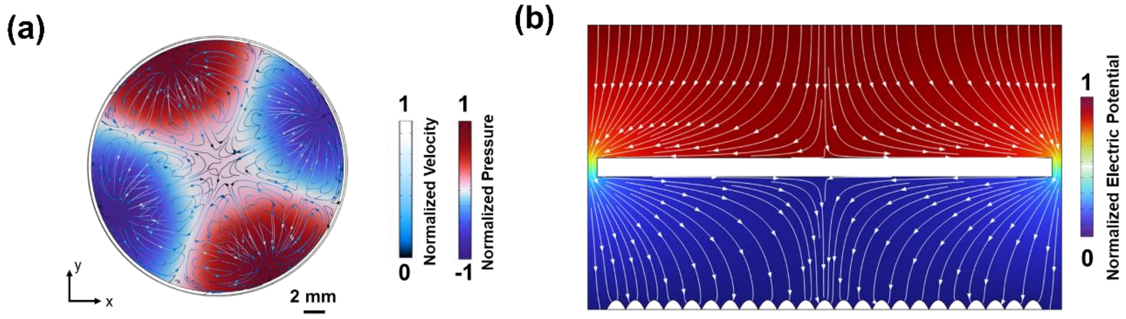

Figure 3.16 (a) Simulation results of velocity and pressure in the electrolyte with an acoustic wave. (b) Simulation results for electric field distribution of sodium dendrite with an acoustic wave.

3.5 Conclusion

In conclusion, an interdisciplinary method to control the shuttle effect of NaPSs by applying an external acoustic field to both sides of the battery case is proposed. Additional surface charges are generated when BTO nanoparticles are exposed to an external acoustic field, where these nanoparticles become more polarized under the stronger driving force created by coupled fields due to the piezoelectric effect. This increased surface charges attract more sodium polysulfides, thus mitigating the shuttle effect. Sodium polysulfide transfer visualization experiments, along with comprehensive electrochemical characterizations, and finite element simulations, provide strong evidence for the method's validity and effectiveness. Furthermore, the enhanced streaming flows generated by the acoustic field promote a uniform distribution of sodium ions, reducing the risk likelihood of sodium dendrite formation. This dendrite growth inhibition was demonstrated through long-term stability tests, including Na-Na symmetric batteries and Na-Cu cells. The application of acoustic fields significantly improves the performance and cycle life of various battery systems. Given these beneficial effects advantages, we believe that this technology offers a novel approach to producing high-performance Na-S batteries.

Chapter 4 - Mechanism and Kinetics of Na_2S_x (x≤ 2) Precipitation in Sodium - Sulfur and Sodium/(Oxygen)-Sulfur Batteries

Disclosure

The major part of this chapter has been published by The Electrochemical Society: Qipeng Zhang, Tairan Yang, and Zheng Li. " Mechanism and Kinetics of Na_2S_x (x≤2) Precipitation in Sodium - Sulfur and Sodium/(Oxygen)-Sulfur Batteries. " *J. Electrochem. Soc*. 2024, **171**, 010503.

4.1 Abstract

In the previous chapter, an innovative approach using acoustic fields was introduced to enhance the performance of sodium-sulfur batteries. However, despite these improvements, the basic mechanism and kinetics have not been involved yet, especially in discharge product growth, which affects electrochemical performance. Meanwhile, additional redox activities (in the presence of oxygen) could simultaneously suppress sodium polysulfide shuttling and enhance energy density. However, the kinetic study of the intermediate has not been explored. In this project, we discussed

the deposition of low-order sodium polysulfide (Na_2S_x, $x \leqslant 2$) in different potentials and type of glyme-solvents in Na-S and Na/(O_2)-S system. The results show that the morphology of deposition Na_2S_x ($x \leqslant 2$) is affected by interfacial energy barrier controlled by overpotentials and the radius of sodium ions, which produced the precipitation of particle shape rather than film. Potentiostatic experiments show the kinetics are elevated in the presence of oxygen. In addition, exchange current density of different sodium polysulfides were studied. The high-order sodium polysulfide has a lower exchange current density than that of low-order sodium polysulfide in Na-S system, requiring greater driving force, while transformation of the intermediate from high-order oxy-sulfur to low-order oxy-sulfur species require less impulse in Na/(O_2)-S systems. This study provides a new idea to understand the deposition mechanism and kinetics of Na_2S_x ($x \leqslant 2$) in Na-S and Na/(O_2)-S system, guiding the selection of suitable solvents and potentials

4.2 Introduction

Affordable, high-energy-density electrochemical storage technology is essential for advancing electric vehicles and modernizing power grids [2]. The development of Li-S batteries with a lithium-metal anode and a sulfur cathode has received a lot of attention over the past ten years because of their high theoretical capacity of 1675 mAh g^{-1}. However, due to a paucity of lithium resources (the earth's crust only contains about 0.0065% of it), Li-S batteries are prohibitively expensive and especially impractical for grid-scale energy storage applications [191-193]. Therefore, it is urgent to explore and develop a new alternative battery system. RT Na-S batteries are garnering more attention due to their low price (\$50-100 kWh^{-1}), abundant source of elements (sodium have elements of 2.7%), and same theoretical capacity (1675 mAh g^{-1} when Na-S battery is fully converted to Na_2S) [35,194]. RT Na-S and Li-S batteries are chemically similar, but not identical. Both of them mainly undergo multi-step reactions between metal anode and S cathode, which is a typical multi-platform phenomenon in discharge profile. However, the discharge behaviors are actually different, which might be due to the inherent differences between sodium and lithium. With a larger ionic radius than lithium, sodium ions exhibit slower reaction kinetics, especially in solid-phase conversion processes, alongside a significant volume expansion (260% from S to Na_2S). Furthermore, high-order sodium polysulfide discharge products display increased solubility in liquid electrolytes [195].

Therefore, in the past decades, people have been trying to find electrode and electrolytes suitable for sodium ion embedding and have successfully developed many new Na-based materials and solvents, achieving high energy-density. For instance, Jiang et al. developed sulfur-doped disordered carbon. The advantageous inclusion of sulfur into the carbon structure may offer more reaction sites for Na^+ accommodation. This design enabled the Na-S batteries to deliver strong performance, retaining a specific capacity of 271 mAh g^{-1} at 1 A g^{-1} over the course of 1000 cycles [169]. Li et al. proposed a new hybrid strategy using oxygen in sodium sulfur system, which alter the underlying reaction pathway, achieving a high discharge capacity of over 1400 mAh g^{-1} [196]. Although these mentioned RT Na-S batteries show better electrochemical performance, Na_2S_x ($x \leqslant 2$) growth in RT Na-S battery has not been systematically elucidated [197].

Herein, the kinetics and morphology of electrodeposition of Na_2S_x ($x \leqslant 2$) on carbon surface with three glyme-based polysulfide solutions in Na-S and Na/(O_2)-S batteries were studied. For Na-S system, the deposition mechanism of Na_2S_x ($x \leqslant 2$) was determined by kinetic analysis and direct observation of the morphology of Na_2S_x ($x \leqslant 2$) in different deposition time. The results reveal that the morphology of electrodeposited Na_2S_x (with $x \leqslant 2$) is determined by the density of nucleation and the relative rates of nucleation and growth. These parameters can be manipulated by selecting appropriate overpotential and solvent in the Na-S system, leading to the formation of particulate structures instead of a film. However, the deposition of discharge products is solvent sensitive but seems to be less sensitive to overpotential in system Na/(O_2)-S system. In addition, the exchange current densities of different high-order polysulfide compounds were also evaluated. The results show that the exchange current density of high-order sodium polysulfide solution is lower than that of low-order sodium polysulfide solution for system in the absence of oxygen, which means that the driving force required is larger. Meanwhile, we found, compared with the Na-S system, when the high-order goes to the low-order sodium polysulfide, less drive is needed in Na/(O_2)-S. This work provides a way to understand the deposition of Na_2S_x ($x \leqslant 2$).

4.3 Experimental section

4.3.1 Preparation of materials

Sodium polysulfide (Na_2S_x, $4 \leqslant x \leqslant 8$) solution was prepared by stirring 0.5 M sodium trifluoromethanesulfonate ($NaSO_3CF_3$, Alfa Aesar) in Diglyme, Triglyme, and Tetraglyme electrolyte first, and then 1.5 M sodium sulfide (Na_2S, 99%, Alfa Aesar) and 4.5, 6.0, 7.5, 9.0, 10.5 M sulfur (Alfa Aesar), respectively were added into electrolytes at 60 °C for 8 h. The total sulfur concentration in the polysulfide solution was 1.5 M. The electrolyte was dried on molecular sieves for 7 d. The $NaSO_3CF_3$ salt was dried under vacuum at 120 °C for 8 h.

4.3.2 Potentiostatic experiments

Graphite felt with a diameter of 14 mm and thickness of 1-1.5 mm was used as a working electrode. Na polysulfide (nominal Na_2S_6) solution of 40 uL was uniformly dropped on the graphite felt. The sulfur loading was calculated to be around 1.25 gm cm^{-2}. Na metal was used as a counter/reference electrode, and glass microfiber filters (GF/D, Whatman) were used to separate the electrode. All Na-S cell were performed in CR2032-type coin cells in an argon-filled glovebox (O_2 < 0.1 ppm, H_2O < 0.1 ppm). For the Na/(O_2)-S cell, the coin cell with 4 side holes was assembled and tested in the oxygen-filled box. The cells were first discharged galvanostatically. Subsequently, a potentiostatic experiment was carried out where the potential was held at different voltages (1.64, 1.66, 1.67, and 1.68 V) for the reduction of polysulfides.

4.3.3 Electrochemical impedance spectroscopy Measurements

EIS measurements were performed Bio-Logic SP-150 potentiostat. All sodium polysulfide solution was taken with in Tetraglyme with 0.5 M $NaSO_3CF_3$ supporting electrolyte. Na-S cells were measured using a 5-mV amplitude over the frequency ranging from 100 kHz to 10 mHz.

4.3.4 Exchange current density measurements

In the galvanostatic polarization test, a specified current was applied to the H-cell using a 3 mm glassy carbon working electrode (CH Instruments, Inc.), and the potential was averaged over a 30-minute constant-current step. For the Na/(O_2)-S cell configuration, experiments were performed within an oxygen-filled chamber.

4.3.5 Microscopy characterization

SEM of the graphite felt was carried out using JSM-IT500HR SEM (JEOL, Peabody, MA, USA).

4.4 Results and discussion

4.4.1 Synthesis and characterization of Na_2S_8, Na_2S_7, and Na_2S_5 polysulfides

The characterization of sodium polysulfides (Na_2S_8, Na_2S_7, and Na_2S_5) presents significant challenges due to their toxicity and deliquescence. These properties complicate handling and measurement, particularly with conventional analytical instruments. To overcome these issues, sodium polysulfides were dissolved in tetraglyme (TEGDME) electrolyte for Raman spectroscopy analysis. As shown in **Figure 4.1**, the Raman spectrum of Na_2S_5 exhibits a weak but distinctive peak at approximately 427 cm^{-1}, attributed to the presence of the S_5^{2-} species [198]. This distinct feature allows for differentiation from other polysulfide species, which show variations in their spectral signatures.

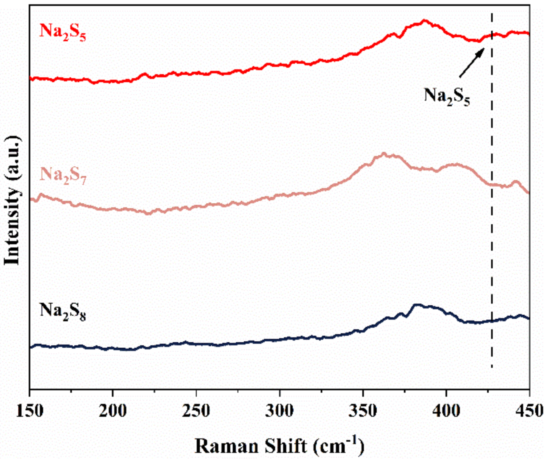

Figure 4.1 Raman testing for Na_2S_5, Na_2S_7, and Na_2S_8 in TEGDME electrolyte.

Further analysis of the Raman spectra (**Figure 4.2**) reveals that as the sulfur content increases, a new characteristic peak emerges around 490 cm^{-1} for Na_2S_7 [199]. This peak is indicative of the formation of the S_7^{2-} species, highlighting a structural transition with increasing sulfur concentration. In contrast, Na_2S_8 does not exhibit any distinctive peaks in this region, suggesting a different bonding environment or molecular structure. Additionally, the Raman signal for Na_2S_8 shifts slightly to higher wavenumbers compared to Na_2S_7, further supporting the notion that the molecular structures of Na_2S_7 and Na_2S_8 differ significantly despite both containing high sulfur content.

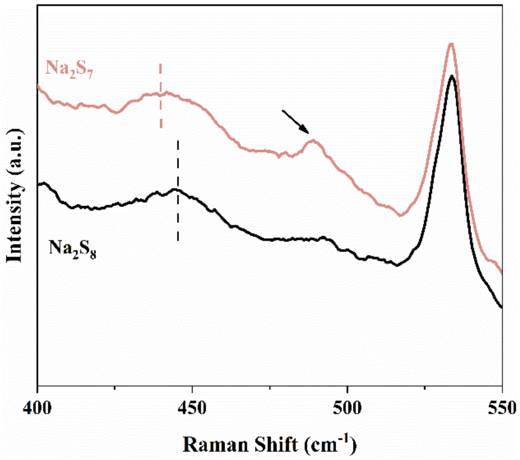

Figure 4.2 Raman testing for Na_2S_7 and Na_2S_8 in TEGDME electrolyte.

Open-circuit voltage (OCV) measurements provide further insight into the electrochemical behavior of Na_2S_7 and Na_2S_8 electrolytes. As shown in **Figure 4.3**, the OCV of Na_2S_8 is initially higher, changing from 2.28 V to 2.27 V over a period of 1500 seconds, which is greater than the OCV observed for Na_2S_7 under the same conditions. This difference in OCV highlights the distinct electrochemical properties of these polysulfides and underscores the importance of further exploring their behaviors in practical applications.

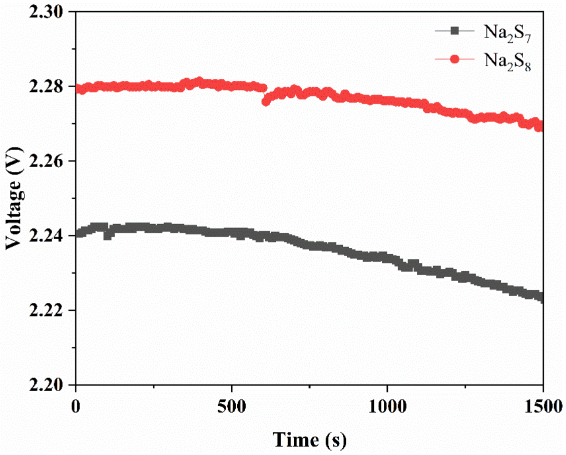

Figure 4.3 Comparison of OCV for Na_2S_7 and Na_2S_8.

4.4.2 Mechanism and kinetics in Na-S systems

In the potentiostatic experiment, a constant driving force (i.e., overpotential) is provided and the time evolution of sulfur reduction is monitored by constant current so that the potential is kept below the equilibrium potential (determined at 1.805 V in the electrolytic cell, **Figure 4.4**). Starting solutions consisted of 1.5 M Na_2S_6 as the sulfur source, dissolved in three different solvents (diglyme, triglyme, and tetraglyme respectively) with 0.5 M sodium trifluoromethanesulfonate ($NaSO_3CF_3$) as a supporting sodium salt (glyme-based ether solvents are typically used in electrolytes, which provide the exceptional reversibility in Na-S batteries). When the Na-S battery is discharged, several polysulfides can coexist in the electrolyte in a balanced and reduced state. To distinguish the electrodeposition of Na_2S_x ($x \leqslant 2$) from the reduction of Na_2S_4 or higher order sodium polysulfides (i.e., Na_2S_6) in solution, each cell is first discharged with a constant current at a C/24 rate to a potential of 1.7 V. Subsequently, a potentiostatic experiment was carried out where the potential was held at different voltage (between 1.64 and 1.68 V *vs.* Na/Na^+) for the reduction of polysulfides.

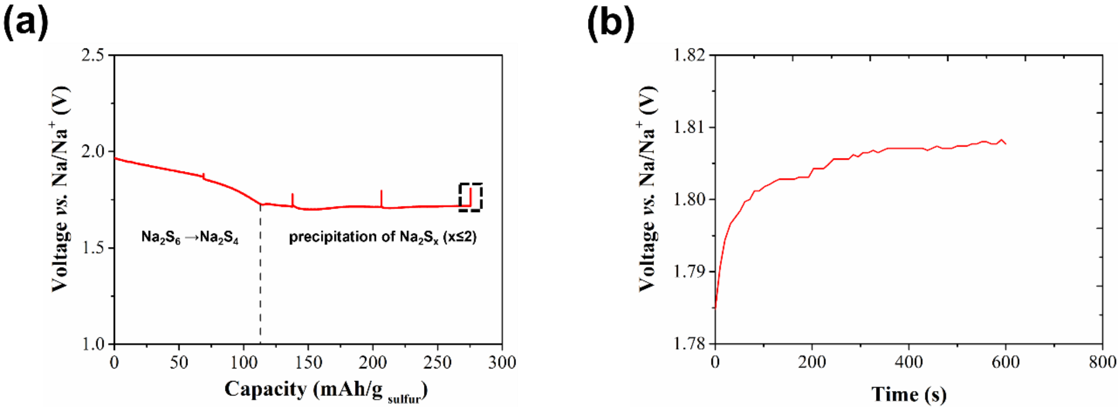

Figure 4.4 (a) GITT profile for a Na_2S_6 electrode solution in tetraglyme, showing C/24 current pulses with 10-minute relaxation intervals. (b) Expanded view of the initial relaxation phase at the start of the precipitation plateau (indicated by the black circle in (a)).

The evolution of polysulfides reduction over time is recorded via the current flow and the change of voltage and current is shown in **Figure 4.5a**. Using tetraglyme electrolyte for example, during the initial galvanostatic discharge process, the voltage was observed to decrease monotonically due to the gradual conversion of higher-order polysulfide (Na_2S_x, $x \geq 4$) into Na_2S_4 in the solution. The potentiostatic discharge began at around 12000 s and the current decreased significantly at the beginning. This was attributed to the reduction of the remaining higher-order sodium polysulfides (Na_2S_x, $x \geq 4$). Following that was a current peak which was due to the nucleation of Na_2S_x ($x \leq 2$) and its growth to impingement [200]. The curve (in red) is well fitted as the sum of two exponential functions, representing the reduction of Na_2S_6 and Na_2S_4 (blue and red, respectively), and a peak resulting from the electrodeposition of Na_2S_x ($x \leq 2$) in **Figure 4.5b**. Since the equilibrium potential for the reduction of Na_2S_6 is higher than that of Na_2S_4, there is a greater overpotential for the reduction of the former species, and hence a greater initial current. Besides, the reduction current of the former species fades rapidly due to the relatively lower concentration, and then the current asymptotically approaches zero, which is attributed to the deposition of Na_2S_x ($x \leq 2$) practically ceases.

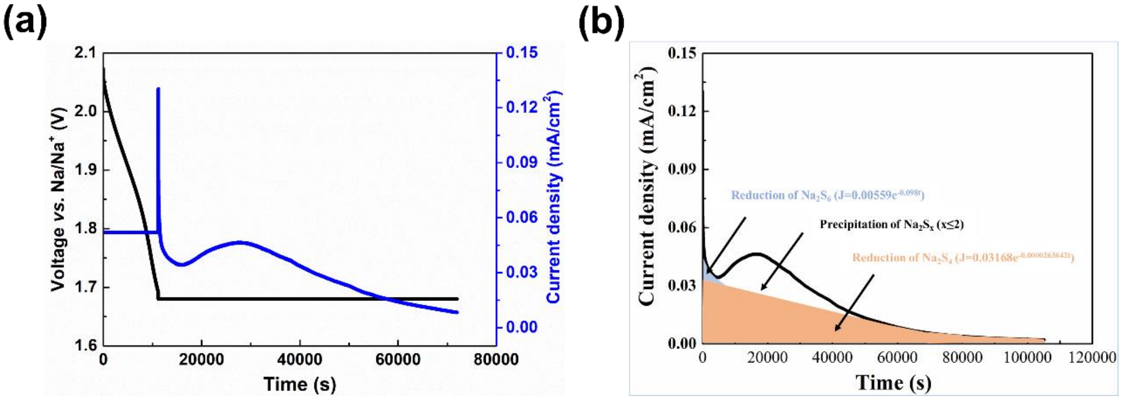

Figure 4.5 (a) Voltage and current density vs time for the baseline Na-S cell, which was galvanostatically discharged to 1.70 V first and then potentiostatically discharged at 1.68 V. (b) Fitting of current vs time curve. The curve was fitted as the sum of two exponential functions, representing the reduction of Na_2S_6 and Na_2S_4 (blue and orange, respectively).

Next, based on the phase transition theory, is carried out and reveals the behavior characteristics of two-dimensional island nucleation and growth (precipitation) process. The sum of two exponential functions was first used as the background fitting of the current-time curve, and the peaks are isolated by the subtraction of the exponential functions (**Figure 4.6a**). The current peak value is sigmoidal cumulative distribution function (**Figure 4.6b**), and its distribution obeys Avrami form (Equation 4-1) [201]:

$$Y(t) = 1 - exp(-\pi A K^2 t^n / 3) \tag{4-1}$$

where Y is the fraction of the material that has been transformed, n is the Avrami exponent, and A and k are the nucleation and growth rates, respectively. Both AK^2 and n are related to the dimensionality of growth [202]. Fitting the data with the equation 4-1 (**Figure 4.7**) gives an Avrami exponent is 2.998 (close to 3), which is consistent with progressive nucleation [203].

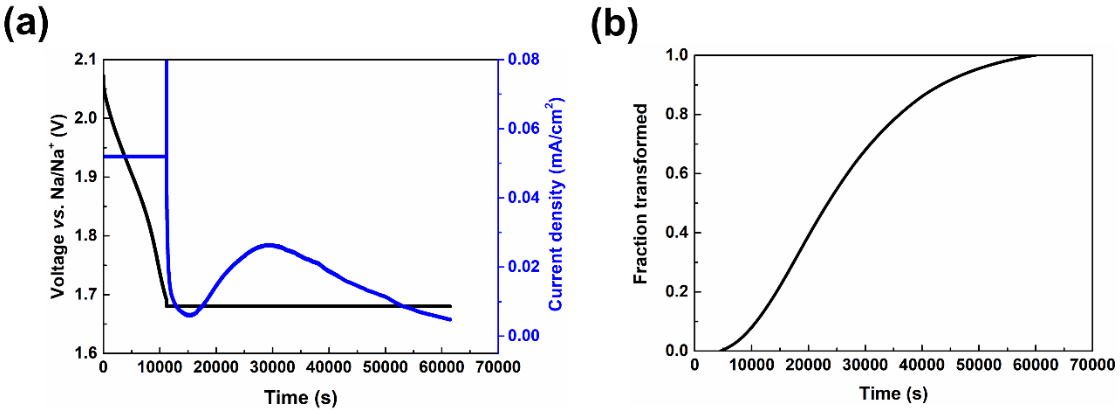

Figure 4.6 (a) Time-dependent voltage and current density profile for a baseline Na-S cell, initially discharged galvanostatically to 1.70 V, followed by a potentiostatic discharge at 1.68 V. (b) Time evolution of the transformation during the potentiostatic current peak (highlighted in red in (a)).

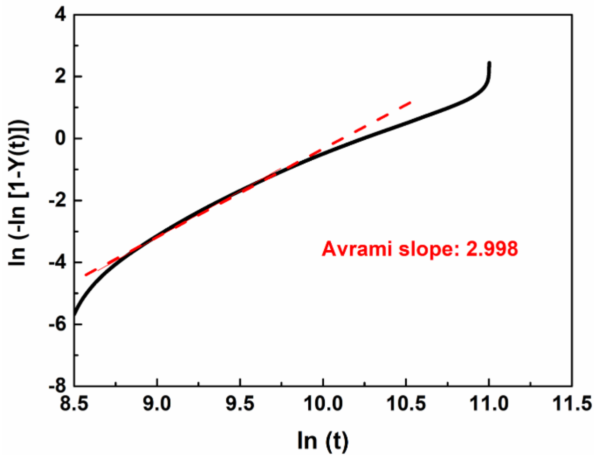

Figure 4.7 Avrami plot resulting from the Figure 4.6b.

Direct imaging by scanning electron microscopy (SEM) confirmed the dimension and deposition morphology inferred from kinetic analysis. **Figure 4.8** shows the potentiostatic deposition curve measured, as well as the image of the pristine carbon fiber. Morphology of Na_2S_x ($x \leq 2$) precipitation at times of 0, 1, 2, and 3 h, respectively, In the first 1 h, the discharge products are relatively small and evenly distributed due to small overpotential. With the increase of deposition time, the overpotential increases continuously, resulting in higher surface energy barrier to absorb S_4^{2-} and the formation of new nuclei. Thus, the growth of Na_2S_x ($x\leq2$) is restricted. When the deposition time is 2 or 3 hours, deposition of Na_2S_x ($x\leq2$) mainly grows, accompanied by other new nuclei. Chiang's group studied morphology of Li_2S electrodeposited on carbon-based materials by glyme-based non-aqueous polysulfide solution [204]. They discovered that the electrodeposited Li_2S has the shape of a thin 2D film. Unlike the deposition of lithium sulfide, the radius of sodium ion is much larger than that of lithium ion, and the insufficient surface area also makes the deposition of deposition of Na_2S_x ($x\leq2$) not as uniform as that of lithium sulfide [205,206]. Thus, the precipitation of particle shape to the Na_2S_x ($x\leq2$) rather than film.

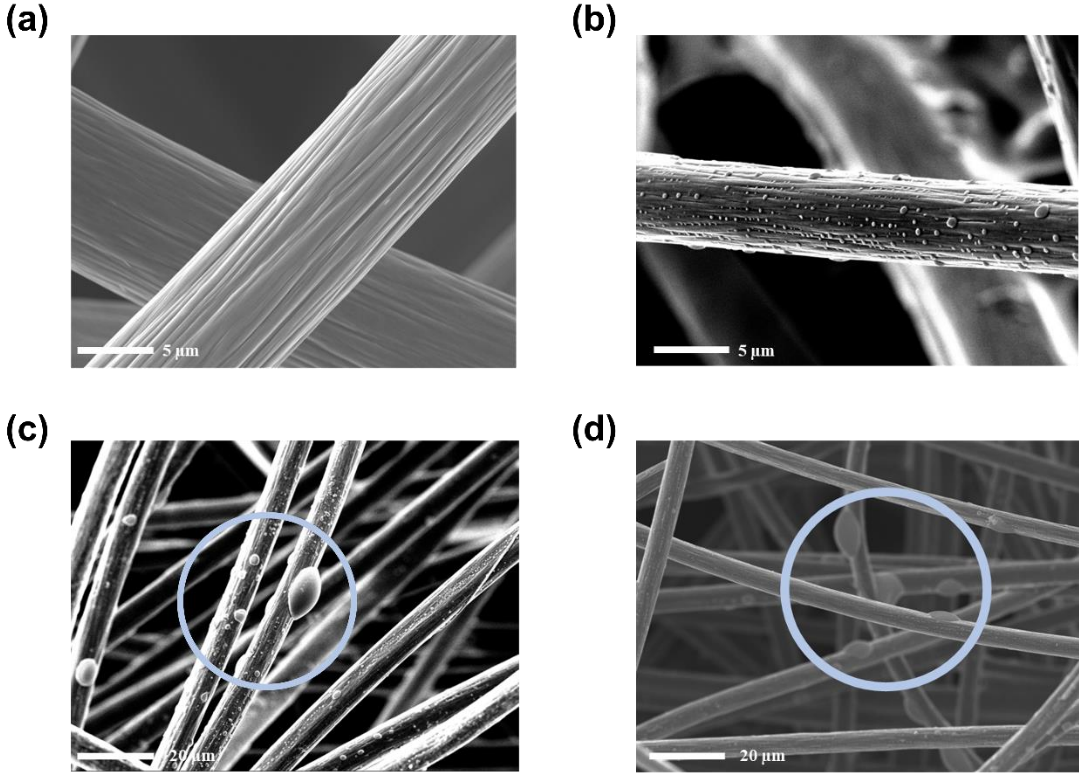

Figure 4.8 (a) SEM image of fresh graphite felt. SEM images taken following (b) 1 hour, (c) 2 hours, and (d) 3 hours of processing.

It is also worth noting that the incomplete Na_2S_x ($x \leq 2$) transformation also affects the precipitation, but this is mainly limited by the kinetics of the surface reaction. Meanwhile, additional experiments were performed to verify that the chemical transformation of Na_2S_x ($x \leq 2$) must be limited by the kinetics of the surface reaction, rather than by the supply of sulfur or mass transfer to the growth interface. Cyclical voltammetry was used on graphite felt to see if mass transport might be constrained. In the 19000 s experiment, where the diffusion length is more than 1mm, the diffusion coefficient of Na_2S_x is 9.37 10^{-7} cm^2 s^{-1}, as shown in **Figure 4.9**. Mass migration of the polysulfide to the deposition site cannot be prevented if the distance between electrode fibers is about 20 μm (**Figure 4.10**).

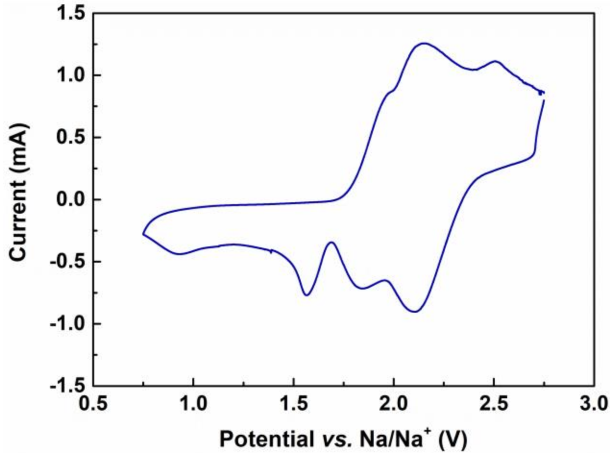

Figure 4.9 Cyclic voltammetry using a graphite felt electrode. The peak current is used to determine the diffusion coefficient of sodium polysulfides.

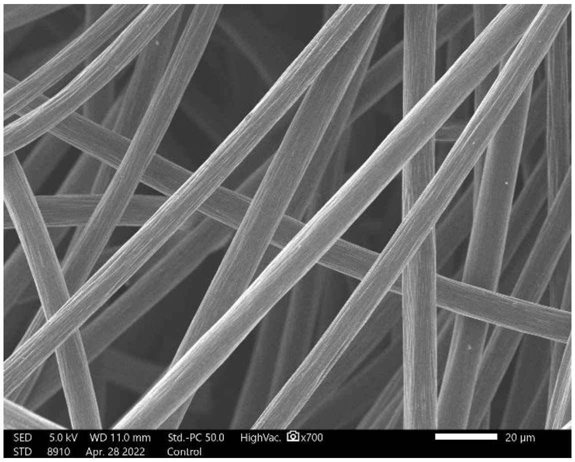

Figure 4.10 SEM image of graphite felt.

Based on the above morphological and kinetic observations, we proposed the possible growth mechanism of Na_2S_x ($x \leq 2$), as shown in **Figure 4.11**. We think the first Na_2S_x ($x \leq 2$) particle deposition was characterized by relatively tiny and homogeneous particles because of the initial nucleation density and minimal overpotential. However, the interfacial energy barrier starts to rise as the amount of precipitation rises. More new places cannot be discovered to continue to deposit and expand since the surface area is constrained and the sodium ion itself is huge. Therefore, particles make up the majority of the Na_2S_x ($x \leq 2$) deposition. Additionally, because Na_2S_x ($x \leq 2$) has a very low conductivity, it is difficult for the reaction to proceed when it is deposited on the graphite felt surface. As a result, the final current decreases until it almost reaches zero.

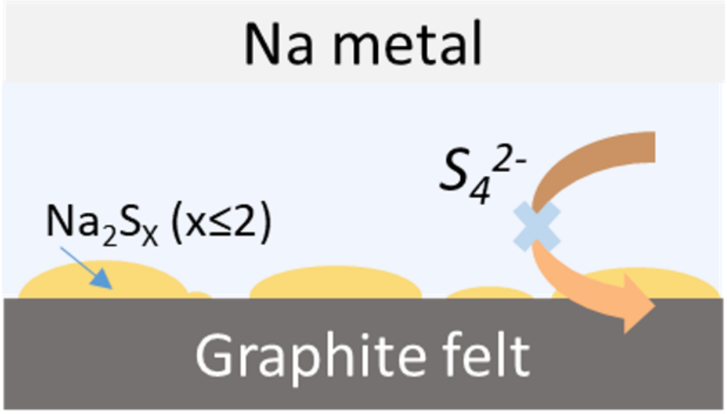

Figure 4.11 Proposed mechanism for the reduction of sodium polysulfides.

By performing the potentiostatic discharge at different voltages in tretaglyme electrolyte, the nucleation-growth rate constant could also be calculated at different voltages. To be more specific, the baseline Na-S cells were galvanostatically discharged to 1.70 V at a rate of C/24, and then potentiostatically discharged at 1.68 V, 1.67 V, 1.66 V, and 1.64 V in **Figure 4.12a**. It is clear that the reduction of current provides a greater overpotential for the electrodeposition process. Therefore, the deposition rate of Na_2S_x ($x \leq 2$) is significantly increased. In the meanwhile, potentiostatic discharge at different voltages using other two ether-based solvents were also performed in **Figure 4.12b** and **4.12c**. When the solvent is changed to triglyme or diglyme, the deposition rate of Na_2S_x ($x \leq 2$) increases significantly, which may be due to the chain lengths of triglyme and diglyme are significantly decrease compared with the tetraglyme. As the length decreases, the number of oxygen molecules decreases, as well as the viscosity. In addition, the viscosity of the solvent also affects the diffusion rate of sodium ions. CV curves of 1 M Na_2S_6 in three different solvents with different sweep speeds were obtained in **Figure 4.13**. We can see that the diffusion rate of sodium ion in three different solvents is diglyme > triglyme > tetraglyme. This shows that in solvent diglyme, sodium ions can be constantly replenished and react on the surface of the graphite felt. This increases the rate of subsequent deposition. It's worth noting that two current peaks were observed in diglyme electrolyte. The first peak is possibly due to the electrodeposition of Na_2S_x ($x \leq 2$) from higher-order polysulfides that has not been fully reduced to Na_2S_4 during the galvanostatic discharge process, which is assigned to significant reduction in viscosity (tetraglyme is about four times as viscous as diglyme) [207]. Therefore, the second current peak in the curve was used for fitting and calculating the nucleation-growth rate constant. **Figure 4.12d** shows the nucleation-growth rate constants at different voltages. The decrease of voltage provides a larger overpotential for the electrodeposition process and therefore increased nucleation-growth rate constants are observed. This increase is especially noticeable (even two orders of magnitude higher) when the voltage goes down to 1.64 V. This pattern is also consistent with the electrodeposition of Li_2S on carbon surfaces [204].

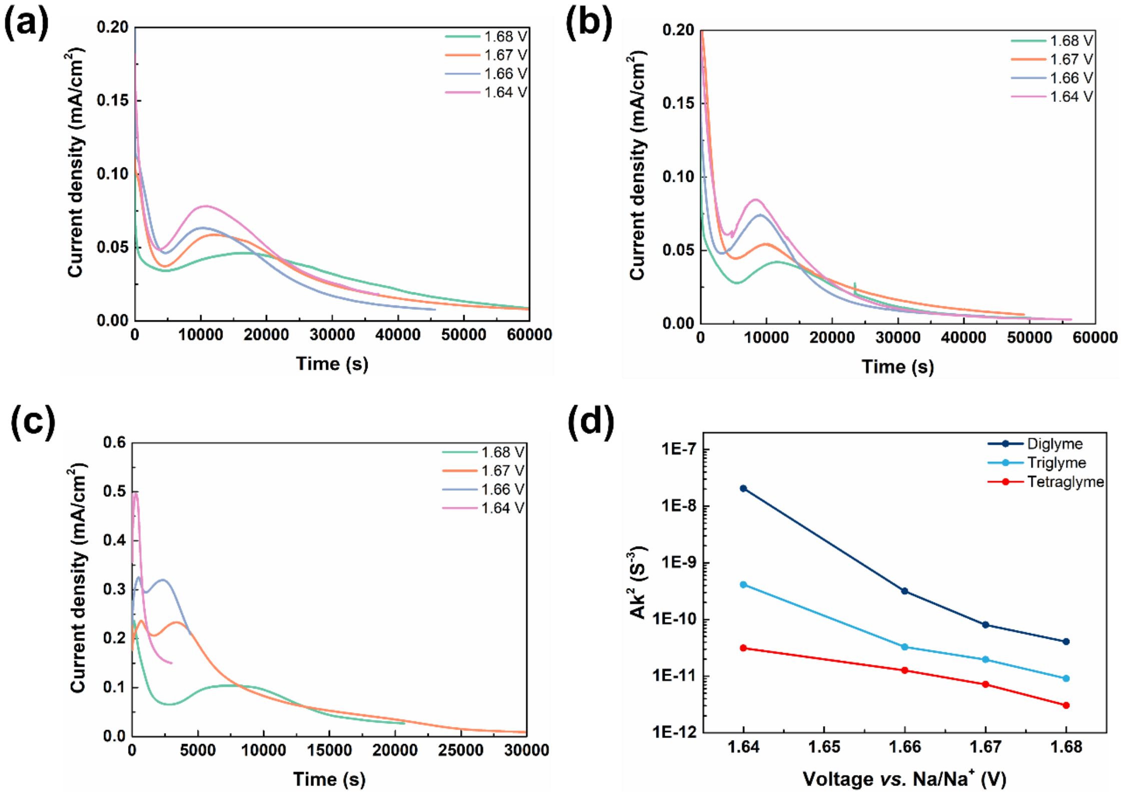

Figure 4.12 Potentiostatic discharge current-time curves in different solvents: (a) tetraglyme, (b) triglyme, and (c) diglyme. (d) Rate constants for nucleation and growth calculated from fitting the current peaks.

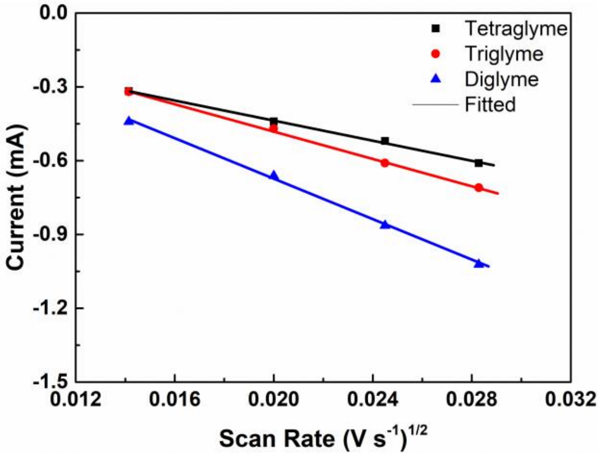

Figure 4.13 The diffusion coefficient for 1 M Na_2S_6 in three different electrolytes recorded from 0.2 to 0.8 mV s^{-1}.

Figure 4.14 illustrates the deposition kinetics of Na_2S_6 at different concentrations (1.5 M, 2.0 M, and 2.5 M) in three different ether-based electrolytes: diglyme, triglyme, and tetraglyme. **Figure 4.14a-c** shows the current density as a function of time during potentiostatic discharge for each electrolyte at varying Na_2S_6 concentrations. **Figure 4.14d** against the concentration of Na_2S_6 for each electrolyte.

As the concentration of sodium polysulfide in the tetraglyme electrolyte increases, the deposition rate also increases. This is likely due to the higher concentration leading to more frequent collisions between reactant species, accelerating the overall reaction process. Similarly, in triglyme, the increase in concentration also enhances the deposition rate, further confirming the influence of concentration on the kinetics.

However, diglyme shows a notable difference in behavior. Despite the increase in concentration, the deposition rate in diglyme does not significantly rise, as reflected in both the current density plots and the rate constant trend. This could be due to the distinct physicochemical properties of diglyme, such as its viscosity or its interaction with sodium polysulfides, which might limit the enhancement of deposition kinetics even at higher concentrations.

Therefore, while increasing the concentration of Na_2S_6 generally promotes faster deposition in tetraglyme and triglyme, the same effect is not observed in diglyme. This highlights the importance of selecting appropriate solvents for optimizing deposition processes in sodium-sulfur battery systems.

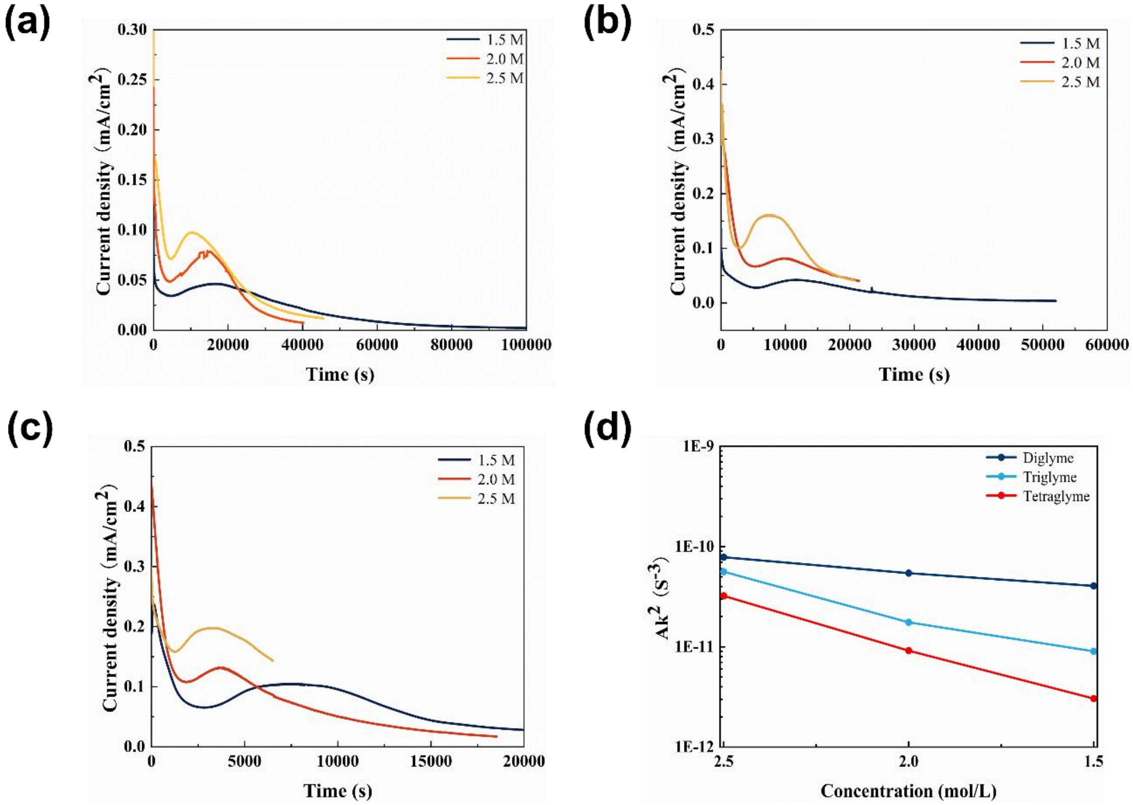

Figure 4.14 Potentiostatic discharge current-time profiles at different Na_2S_6 concentrations across solvents: (a) tetraglyme, (b) triglyme, and (c) diglyme. (d) Nucleation and growth rate constants derived from peak current fitting analysis.

The exchange current density measurement can be used independently to test the Butler-Volmer kinetics at the carbon-solution interfaces, helping us to understand the impedance contributions of various polysulfides and calculate overpotentials. **Figure 4.15** depicts the use of three-electrode cells in tetraglyme solvent to perform galvanostatic polarization at a glassy carbon macroelectrode in order to study the kinetics of Na_2S_6 at "model" carbon surfaces. By retracing the linear segment of the Tafel diagram back to the intercept at the equilibrium potential, one may calculate the exchange current density. The exchange current density of Na_2S_6 was calculated to be 0.019 mA cm^{-2} **(Figure 4.16)**.

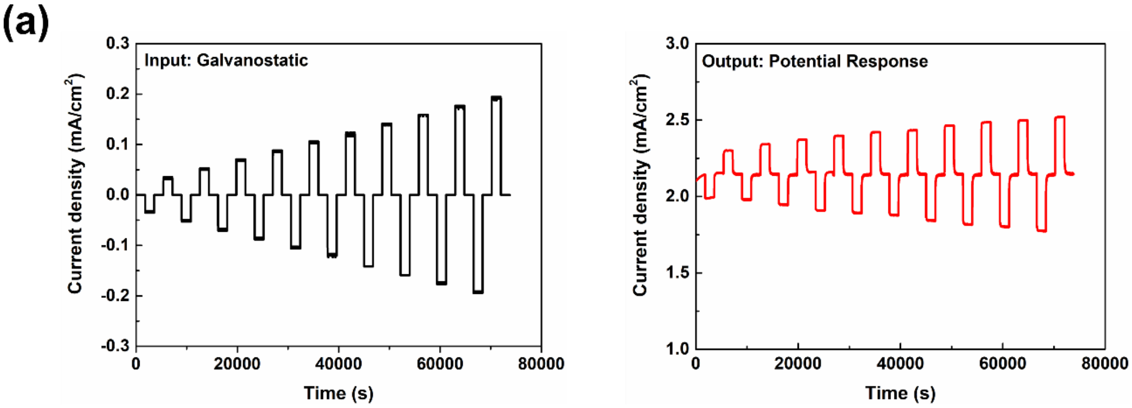

Figure 4.15 (a) In the galvanostatic polarization test, a 3 mm glassy carbon working electrode applied a constant current to the cell for 30 minutes. (b) The average potential over this 30-minute current step is recorded as the resulting potential.

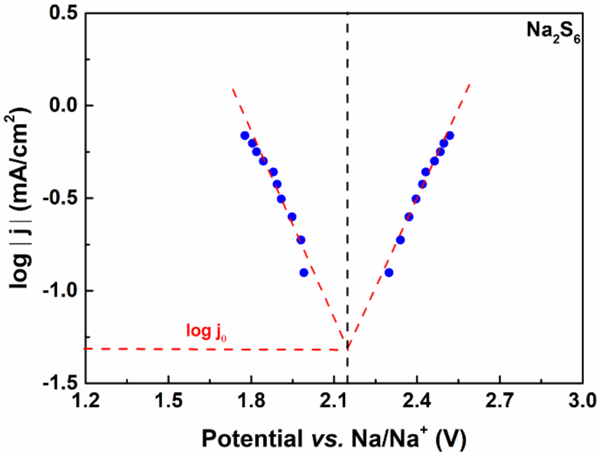

Figure 4.16 Tafel plot of galvanostatic polarization measurements showing electrochemical kinetics in a 1.5 M Na_2S_6 solution with a 0.5 M $NaSO_3CF_3$ supporting electrolyte in tetraglyme.

Dashed lines represent linear extrapolations, while the open-circuit voltage is marked by a dashed vertical line.

Figure 4.17 and **Table 4.1** summarize the exchange current densities measured from Na_2S_8 to Na_2S_4 solutions. The exchange current densities of Na_2S_8, Na_2S_7, Na_2S_6, Na_2S_5, and Na_2S_4 were 0.011 0.014, 0.019, 0.021, and 0.024 mA cm^{-2} respectively. An increasing exchange current indicates a rapid exchange of substances, which means that the reaction encounters little resistance as it changes.

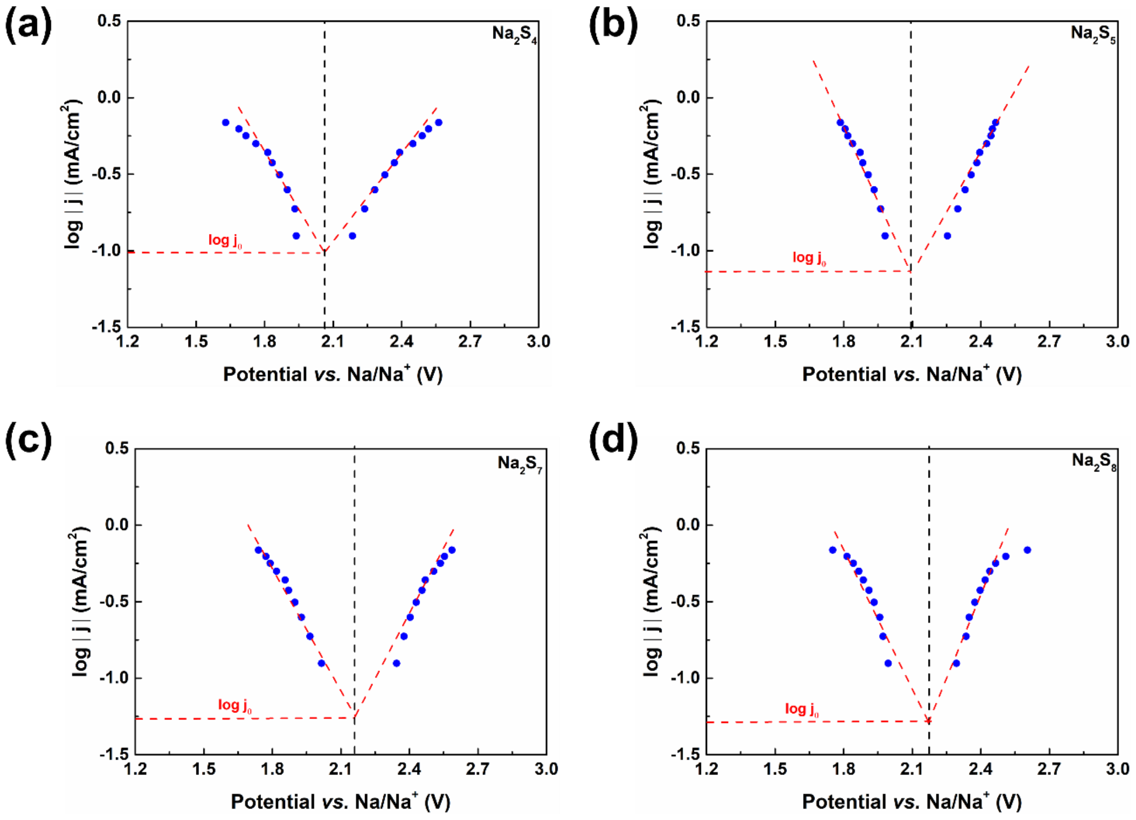

Figure 4.17 The Tafel plot of galvanostatic polarization measurements of electrochemical kinetics in (a) Na_2S_4 solutions, (b) Na_2S_5 solutions, (c) Na_2S_7 solutions, and (d) Na_2S_8 solutions.

Table 4.1 Summary of measured exchange current densities in Na-S systems

Composition	Exchange current density (mA cm^{-2})
1.5 M Na_2S_8	0.011
1.5 M Na_2S_7	0.014
1.5 M Na_2S_6	0.019
1.5 M Na_2S_5	0.021
1.5 M Na_2S_4	0.024

To verify the above interpretation, we performed EIS tests (**Figure 4.18**). It is clear that Na_2S_8 has the highest impedance and Na_2S_4 has the lowest, which is consistent with the result of exchanging current density measurements. At the same time, because Na_2S_8 involves more reaction steps than Na_2S_4, more reaction energy is required (the driving force of the reaction is the largest), so the exchange current density is the smallest.

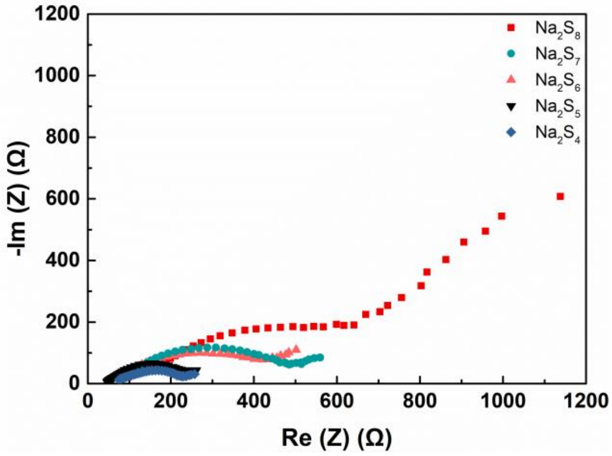

Figure 4.18 Electrochemical impedance spectroscopy (EIS) of different sodium polysulfide.

In addition, the galvanostatic intermittent titration technique (GITT) was employed to investigate the electrochemical reaction kinetics of various sodium polysulfides in a tetraglyme-based electrolyte. The GITT measurements were conducted using a pulse duration of 1800 s and a relaxation time of 600 s. As illustrated in **Figure 4.19a**, the voltage profile of Na_2S_8 shows the characteristic behavior during the GITT test. The study then extended to include other sodium polysulfides (Na_2S_4, Na_2S_5, Na_2S_6, Na_2S_7) in the same experimental setup to determine their diffusion coefficients, as shown in **Figure 4.19b**.

The results reveal that Na_2S_4 exhibits the highest diffusion coefficient throughout the entire discharge process, surpassing the other sodium polysulfides. Specifically, at a 10% depth of discharge (DOD), Na_2S_4 shows a diffusion coefficient of 3.38×10^{-9} cm^2 s^{-1}, while Na_2S_5, Na_2S_6, Na_2S_7, and Na_2S_8 display lower values of 3.13×10^{-9}, 2.94×10^{-9}, 2.73×10^{-9}, and 2.12×10^{-9} cm^2 s^{-1}, respectively. This suggests that Na_2S_4 encounters lower resistance during ion transport, in line with the results of the exchange current density measurements.

The observed trend is consistent with literature reports [208], confirming that Na_2S_4 has superior ionic mobility compared to other sodium polysulfides, further reinforcing its potential advantages in sodium-sulfur batteries. The enhanced diffusion coefficient of Na_2S_4 indicates its role in facilitating faster charge transfer and reducing polarization effects during the discharge process.

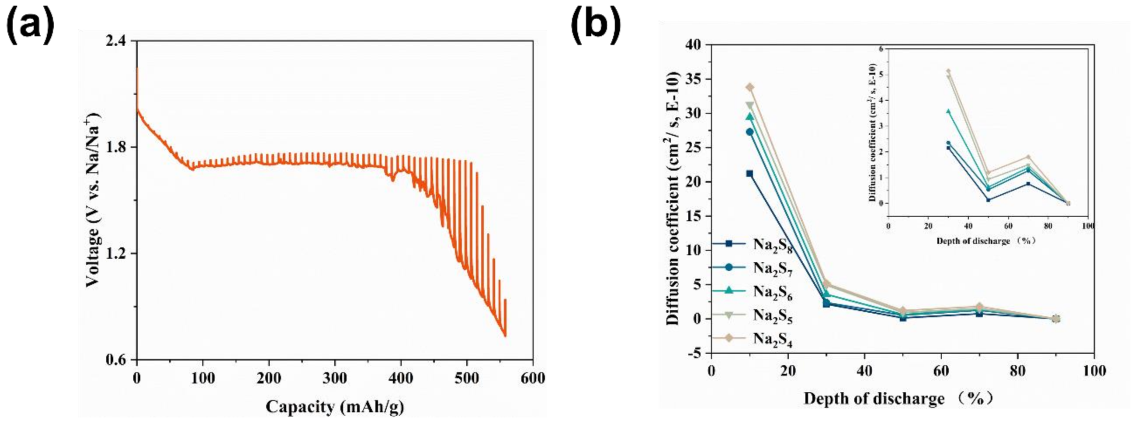

Figure 4.19 (a) GITT curve for a Na_2S_8 electrode solution dissolved in tetraglyme. (b) Diffusion coefficient and discharge profiles derived from GITT measurements.

4.4.3 Kinetics in Na/(O_2)-S systems

According to our previous research [196], NaO_2-Na_2S_n ($4<n\leqslant 8$) was formed through combining Na^+, O^{2-}, and S_n^{2-} ($4<n\leqslant 8$) at the stage of the discharge process when the oxygen is present, which may prevent the polysulfides from diffusing to the sodium side, improving the electrochemical performance. However, the kinetic study of the intermediate has not been explored. This part we investigate interfacial kinetics during the electrochemical reactions in the Na/(O_2)-S system using potentiostatic and exchange current density experiment. The results were shown in **Figure 4.20**. There is no significant difference in the shape of the curves at the same voltages, the biggest difference is in the deposition time and the magnitude of the current density. The deposition time and current intensity of Na/(O_2)-S systems are greater than those of Na-S system in different three solvents, indicating that the kinetics are elevated in the presence of oxygen (this is proved by calculating nucleation-growth rate constants at different voltages). It is also noted that the intermediate appears to be more dependent on viscosity, while it does not seem to be sensitive to the increase in voltages. For example, when we change the solution from triglyme to diglyme at 1.66 V, the value of the constant in Na/(O_2)-S system goes up by a factor of 100, compared to Na-S system, it only goes up by a factor of 10. When we increased voltage from 1.66 to 1.64 V at diglyme solution, we found no significant increase in the constant, but a 100-fold increase compared to the Na-S system.

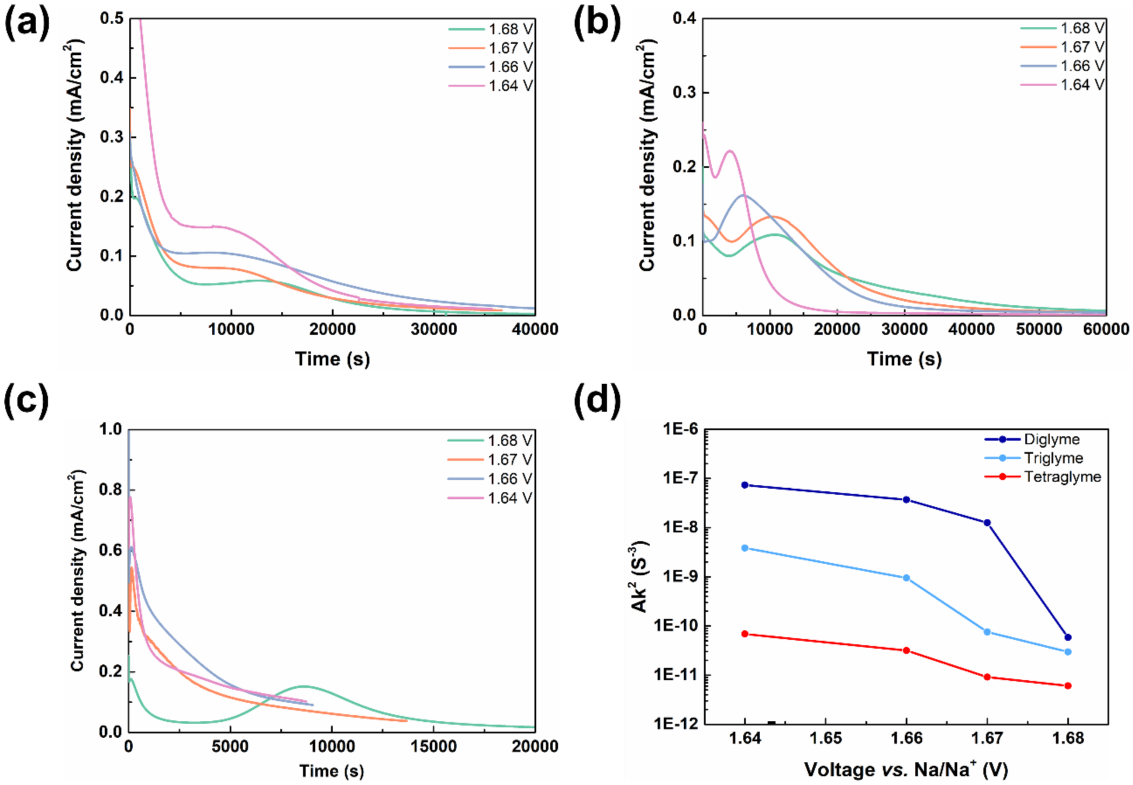

Figure 4.20 Current-time diagrams of potentiostatic discharge in different solvents in the Na/(O_2)-S system: (a) tetraglyme, (b) triglyme, and (c) diglyme. (d) Aggregate rate constants for nucleation and growth.

Exchange current density measurement was also conducted to understand estimate overpotentials. **Figure 4.21** shows the galvanostatic polarization of different sodium polysulfide are measured in tetraglyme solvent when the oxygen exists. The exchange current density is also calculated. **Table 4.2** summarizes the exchange current densities carried out from Na_2S_8 to Na_2S_6 species. The exchange current densities of Na_2S_8, Na_2S_7, and Na_2S_6 were 0.024 0.025, and 0.027 mA cm^{-2} respectively. Compared with Na-S system, the exchange current density is greater than the base one, which indicates a fast exchange of substances when NaO_2-Na_2S_n was formed, meaning that less resistance is required for the reaction. It is worth noting that the exchange current density changes very little when the sulfur source changes from Na_2S_8 to Na_2S_6, which means that the transformation of the intermediate from high-order (NaO_2-Na_2S_n, 4<n≤8) to low-order species (NaO_2-Na_2S_n, 1<n≤4) requires less impulse compared with the Na_2S_n in Na-S systems.

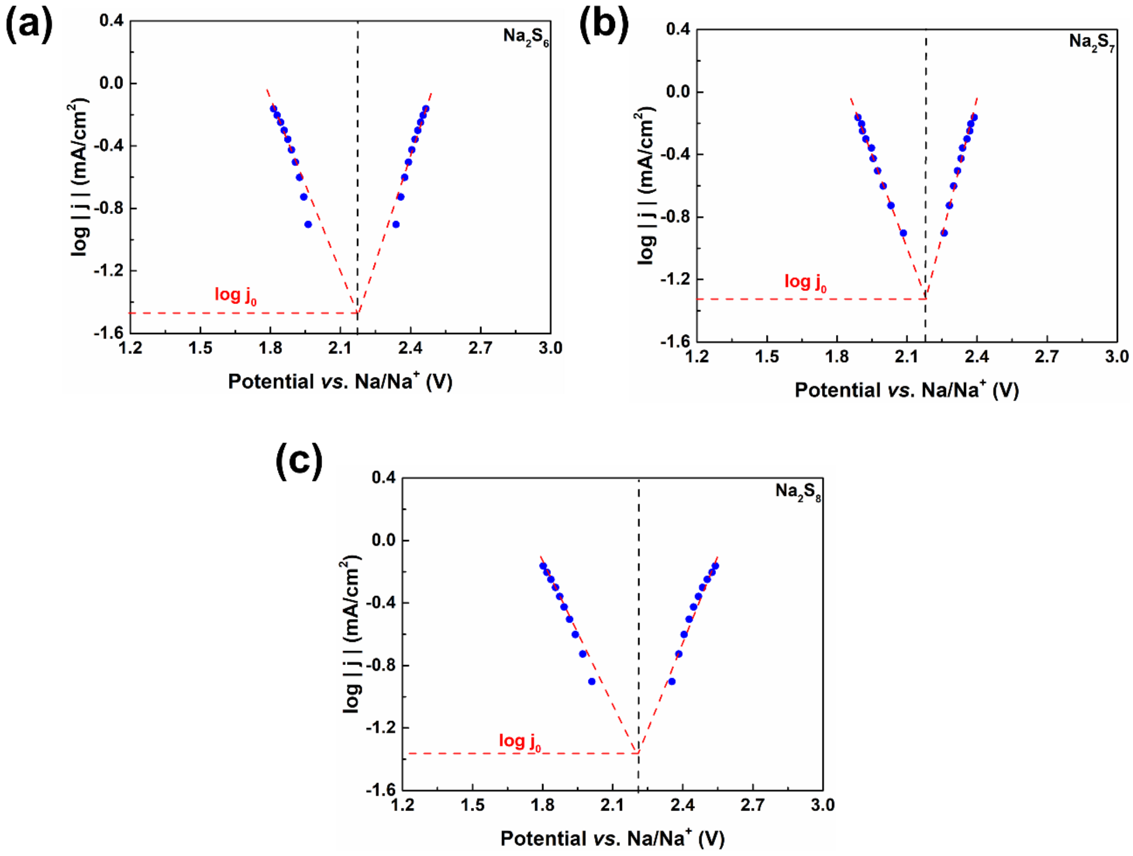

Figure 4.21 Tafel plot of galvanostatic polarization measurements illustrating the electrochemical kinetics in 1.5 M solutions of (a) Na_2S_6, (b) Na_2S_7, and (c) Na_2S_8 in tetraglyme.

Table 4.2 Summary of measured exchange current densities in Na/(O_2)-S systems

Composition	Exchange current density (mA cm^{-2})
1.5 M Na_2S_8	0.024
1.5 M Na_2S_7	0.025

1.5 M Na_2S_6	0.027

4.5 Conclusion

In summary, we studied the deposition of Na_2S_x ($x \leq 2$) in different potentials and solvents with/without oxygen. The results show that the deposit of Na_2S_x ($x \leq 2$) was mainly controlled by overpotential and solvent in Na-S system. The effect of the interface barrier regulated by overpotentials, and the larger sodium ion radius compared with lithium ion cause the electrochemical deposition to take the shape of a particle rather than film. For Na/(O_2)-S system, oxy-sulfur species are mainly affected by solvents. In addition, the effect of different sodium polysulfide on the exchange current density is also discussed. The results showed that the higher order sodium polysulfide had the lowest current density, meaning that it needed a greater push to react. Transformation of the intermediate from high-order oxy-sulfur to low-order oxy-sulfur components requires lesser driving force in Na/(O_2)-S than Na-S systems. This study provides an insight into the mechanism of Na_2S_x ($x \leq 2$) deposition and a new idea for the selection of suitable solvents and potentials.

Chapter 5 – Summary of Contributions and Future work

5.1 Summary and contributions

5.1.1 Chapter 2 - low-concentration electrolyte design for wide-temperature operation in sodium metal batteries

In this chapter, we propose a low-concentration, non-flammable electrolyte, consisting of 0.3 M $NaPF_6$ dissolved in a mixed-solvent system of propylene carbonate (PC), fluoroethylene carbonate (FEC), and 1,1,2,2-tetrafluoroethyl 2,2,3,3-tetrafluoropropyl ether (TTE). This composition is optimized for sodium metal batteries, with the goal of improving their cyclability and performance over a wide temperature range while maintaining safety and cost-efficiency.

Key Contributions: Through a combination of analytical characterization, MD simulations, and practical device testing, we demonstrate several critical advancements enabled by this electrolyte:

1. ***Improved cyclability and extreme-temperature performance:*** Our study shows that a Na||$FePO_4$ system employing the proposed electrolyte achieves a remarkable capacity retention of 92.8% at room temperature and 98.5% at 55 °C, with a Coulombic efficiency exceeding 99%. Moreover, the low viscosity, rapid ion diffusion, and enhanced wetting properties of L-PFT contributed to superior performance at low temperatures (-20 °C).
2. ***Enhanced safety and cost-effectiveness:*** The non-flammable nature of the electrolyte significantly improves the safety profile of sodium metal batteries, reducing risks of thermal runaway. Furthermore, the low concentration of $NaPF_6$ not only reduces the cost of materials but also helps in the scalability of sodium metal batteries technology for larger applications.

Impacts: The findings from this research provide a comprehensive solution to several major obstacles currently faced by sodium metal batteries. By addressing both performance and safety, our low-concentration electrolyte design represents a pivotal step forward in the commercialization of sodium metal batteries. Its ability to maintain superior electrochemical performance over a broad temperature range, coupled with its safety and cost advantages, makes it a promising candidate for future large-scale energy storage applications.

5.1.2 Chapter 3 - inhibiting shuttle effect and dendrite growth in sodium-sulfur batteries enabled by applying external acoustic field

This chapter explores the effects of applying an external acoustic field on the battery's performance. We utilized BTO nanoparticles coated on commercially available glass fiber separators and stimulated them via a controllable acoustic field. By leveraging the piezoelectric properties of BTO, the acoustic field generates surface charges that attract sodium polysulfides, thereby reducing their migration to the sodium anode. Additionally, the acoustic field creates streaming flows in the electrolyte, which enhances sodium ion dispersion and reduces dendrite formation. Our experiments and simulations provide a comprehensive analysis of how this approach mitigates both the shuttle effect and dendrite growth.

Key Contributions: Our work makes several contributions to the field of sodium-sulfur battery research:

1. ***Reduction of shuttle effect**:* The external acoustic field stimulates BTO nanoparticles, which polarize and attract more NaPSs, thereby mitigating the shuttle effect and enhancing battery stability.
2. ***Inhibition of dendrite growth**:* The acoustic field also promotes uniform sodium ion distribution, reducing the formation of sodium dendrites and improving battery cycle life.

3. ***Experimental and simulative validation**:* We combined electrochemical measurements, SEM, and finite element simulations to validate the effectiveness of the proposed method. The results demonstrate a clear improvement in battery performance, with Na-S cells showing a capacity retention of 300 mAh g^{-1} after 50 cycles under the influence of the acoustic field.

Impact: The method we propose offers a new approach to improve Na-S battery performance without requiring chemical additives or complex materials. By addressing both polysulfide shuttling and dendrite formation through the application of an acoustic field, this work opens new pathways for enhancing the cycle life, safety, and efficiency of Na-S batteries. This interdisciplinary method has the potential to significantly impact the development of sustainable energy storage technologies.

5.1.3 Chapter 4 - mechanism and kinetics of Na_2S_x (x⩽2) precipitation in sodium-sulfur and sodium/(Oxygen)-sulfur batteries

In this chapter, our study focuses on the fundamental behavior of Na_2S_x (x⩽2) precipitation in both Na-S and Na/(O_2)-S systems. Specifically, we investigate how different operating potentials, and solvent compositions influence the deposition of sodium polysulfides. The scope of our research includes potentiostatic discharge experiments and electrochemical analysis to determine the nucleation and growth characteristics of Na_2S_x (x⩽2) on carbon surfaces. By addressing both the Na-S system and the hybrid Na/(O_2)-S system, where oxygen is used to modify the reaction pathways, our work provides a comprehensive understanding of how to control sodium polysulfide deposition for enhanced battery performance.

Key Contributions: Our research makes several significant contributions to the field of energy storage, particularly in the development of RT Na-S batteries:

1. ***Mechanistic understanding:*** We reveal that the nucleation and growth of Na_2S_x ($x \leqslant 2$) are influenced by the interplay between solvent properties and overpotential, resulting in the formation of particle-like deposits rather than films. This mechanistic insight is crucial for designing better electrode materials and electrolyte systems.
2. ***Hybrid Na/(O₂)-S systems:*** We extend the understanding of sodium-sulfur chemistry by exploring how oxygen in Na/(O_2)-S systems affects polysulfide kinetics. Our findings show that the presence of oxygen significantly enhances the deposition kinetics of Na_2S_x ($x \leqslant 2$), offering a potential solution to mitigate the polysulfide shuttling effect and improve battery capacity.
3. ***Practical guidelines:*** Our results provide practical recommendations for choosing the optimal solvent and potential conditions in Na-S systems. These insights can directly contribute to the development of high-performance sodium sulfur batteries for large-scale applications.

Impact: The impact of this research lies in its potential to inform the next generation of sodium-based energy storage systems. By advancing the understanding of Na_2S_x ($x \leqslant 2$) deposition behavior, our study helps address one of the challenges facing Na-S battery technology: improving energy efficiency and cycle life. Moreover, the insights gained from our hybrid Na/(O_2)-S system could open new avenues for using oxygen as a redox mediator, further enhancing the electrochemical performance of these batteries. These findings have far-reaching implications for scaling up Na-S batteries in energy-intensive industries.

5.2 Future work

Optimization of low-concentration electrolytes for long-term stability: This study highlights the use of low-concentration electrolytes to improve battery performance, but there is room for deeper exploration into the formulation of these electrolytes. Future work could focus on optimizing the composition and concentration of the electrolyte to balance between maintaining high conductivity and interfacial stability. Additionally, investigating how different solvent systems and additives interact with the low-concentration electrolyte under long-term cycling conditions could provide valuable insights into improving the overall stability and lifespan of the battery. Understanding how these variables affect the electrolyte-sodium interface would be crucial for developing more efficient sodium metal battery systems.

Exploration of alternative materials with enhanced acoustic response: While BTO was utilized in Chapter 3 for its piezoelectric properties, future work could focus on identifying and testing other materials that also exhibit strong piezoelectric or ferroelectric effects. These alternative materials could potentially provide better control over NaPSs shuttling and sodium ion transport under varying acoustic field conditions. Further studies could investigate how different acoustic field frequencies, intensities, and waveforms impact the behavior of these materials. By optimizing these parameters, it may be possible to discover more effective methods to enhance battery performance, particularly in mitigating the shuttle effect and promoting uniform ion transport.

Development of advanced acoustic field designs for improved performance: The current study employs an external acoustic field to influence the behavior of BTO nanoparticles and the electrolyte flow. Future research could explore the development of more advanced or integrated acoustic field systems that are tailored to different battery architectures. This could include the miniaturization of acoustic field devices that could be integrated directly into the battery cell for more localized control over ion distribution and dendrite suppression. Furthermore, modeling the effects of acoustic streaming on a broader range of battery configurations and scaling the technology for larger cells could provide insights into commercializing this approach for grid-scale energy storage and electric vehicles.

Investigation into dendrite growth mechanisms in the presence of acoustic fields: While this study demonstrates the suppression of sodium dendrite growth through the application of an acoustic field, a deeper mechanistic understanding of how acoustic fields interact with the anode surface and influence dendrite formation is needed. Future studies could utilize in-situ microscopy and advanced imaging techniques to directly observe how dendrites grow and dissolve under various acoustic conditions. This could lead to the development of more targeted strategies for eliminating dendrites entirely or delaying their growth to extend the cycle life of sodium-sulfur batteries.

Integration with next-generation sodium-sulfur battery systems: Future work could also focus on integrating this acoustic field method with other emerging advancements in sodium-sulfur battery technology. For instance, combining acoustic field stimulation with new types of solid-state electrolytes or novel electrode materials could offer a more comprehensive solution to the challenges facing Na-S batteries. Additionally, exploring the scalability of this technique in full-cell configurations could provide valuable insights into the commercial feasibility of this approach for large-scale energy storage applications.

By focusing on these future works, we could continue to advance the development of high-performance sodium metal (sulfur) batteries, pushing the boundaries of what is possible in sustainable and scalable energy storage technologies.

References

1. Chu, S., and Majumdar, A. (2012). Opportunities and challenges for a sustainable energy future. Nature *488*, 294-303. 10.1038/nature11475.
2. Larcher, D., and Tarascon, J.-M. (2015). Towards greener and more sustainable batteries for electrical energy storage. Nature Chemistry *7*, 19-29. 10.1038/NCHEM.2085.
3. Usiskin, R., Lu, Y., Popovic, J., Law, M., Balaya, P., Hu, Y.-S., and Maier, J. (2021). Fundamentals, status and promise of sodium-based batteries. Nature Reviews Materials *6*, 1020-1035. 10.1038/s41578-021-00324-w.
4. Yabuuchi, N., Kubota, K., Dahbi, M., and Komaba, S. (2014). Research development on sodium-ion batteries. Chemical Reviews *114*, 11636-11682. 10.1021/cr500192f.
5. Dunn, B., Kamath, H., and Tarascon, J.-M. (2011). Electrical Energy Storage for the Grid: A Battery of Choices. Science *334*, 928-935. 10.1126/science.1212741.
6. Zubi, G., Dufo-López, R., Carvalho, M., and Pasaoglu, G. (2018). The lithium-ion battery: State of the art and future perspectives. Renewable and Sustainable Energy Reviews *89*, 292-308. 10.1016/j.rser.2018.03.002.
7. Manthiram, A. (2017). An Outlook on Lithium Ion Battery Technology. ACS Central Science *3*, 1063-1069. 10.1021/acscentsci.7b00288.
8. Albertus, P., Babinec, S., Litzelman, S., and Newman, A. (2017). Status and challenges in enabling the lithium metal electrode for high-energy and low-cost rechargeable batteries. Nature Energy *3*, 16-21. 10.1038/s41560-017-0047-2.
9. Yin, X., Sarkar, S., Shi, S., Huang, Q.A., Zhao, H., Yan, L., Zhao, Y., and Zhang, J. (2020). Recent Progress in Advanced Organic Electrode Materials for Sodium‐Ion Batteries: Synthesis, Mechanisms, Challenges and Perspectives. Advanced Functional Materials *30*, 1908445. 10.1002/adfm.201908445.
10. Fang, Y., Xiao, L., Chen, Z., Ai, X., Cao, Y., and Yang, H. (2018). Recent Advances in Sodium-Ion Battery Materials. Electrochemical Energy Reviews *1*, 294-323. 10.1007/s41918-018-0008-x.
11. Pu, X., Wang, H., Zhao, D., Yang, H., Ai, X., Cao, S., Chen, Z., and Cao, Y. (2019). Recent Progress in Rechargeable Sodium-Ion Batteries: toward High-Power Applications. Small

15, e1805427. 10.1002/smll.201805427.

12. Fang, Y., Yu, X.-Y., and Lou, X.W. (2019). Nanostructured Electrode Materials for Advanced Sodium-Ion Batteries. Matter *1*, 90-114. 10.1016/j.matt.2019.05.007.
13. Sirengo, K., Babu, A., Brennan, B., and Pillai, S.C. (2023). Ionic liquid electrolytes for sodium-ion batteries to control thermal runaway. Journal of Energy Chemistry *81*, 321-338. 10.1016/j.jechem.2023.02.046.
14. Adelhelm, P., Hartmann, P., Bender, C.L., Busche, M., Eufinger, C., and Janek, J. (2015). From lithium to sodium: cell chemistry of room temperature sodium-air and sodium-sulfur batteries. Beilstein Journal of Nanotechnology *6*, 1016-1055. 10.3762/bjnano.6.105.
15. Yang, J., Zhang, H., Zhou, Q., Qu, H., Dong, T., Zhang, M., Tang, B., Zhang, J., and Cui, G. (2019). Safety-Enhanced Polymer Electrolytes for Sodium Batteries: Recent Progress and Perspectives. ACS Applied Materials & Interfaces *11*, 17109-17127. 10.1021/acsami.9b01239.
16. Darjazi, H., Falco, M., Colo, F., Balducci, L., Piana, G., Bella, F., Meligrana, G., Nobili, F., Elia, G.A., and Gerbaldi, C. (2024). Electrolytes for Sodium Ion Batteries: The Current Transition from Liquid to Solid and Hybrid systems. Advanced Materials *36*, e2313572. 10.1002/adma.202313572.
17. Huang, Y., Zhao, L., Li, L., Xie, M., Wu, F., and Chen, R. (2019). Electrolytes and Electrolyte/Electrode Interfaces in Sodium-Ion Batteries: From Scientific Research to Practical Application. Advanced Materials *31*, e1808393. 10.1002/adma.201808393.
18. Xu, G.L., Amine, R., Abouimrane, A., Che, H., Dahbi, M., Ma, Z.F., Saadoune, I., Alami, J., Mattis, W.L., Pan, F., et al. (2018). Challenges in Developing Electrodes, Electrolytes, and Diagnostics Tools to Understand and Advance Sodium-Ion Batteries. Advanced Energy Materials *8*, 1702403. 10.1002/aenm.201702403.
19. Xu, K. (2014). Electrolytes and interphases in Li-ion batteries and beyond. Chemical Reviews *114*, 11503-11618. 10.1021/cr500003w.
20. Hernández, G., Mogensen, R., Younesi, R., and Mindemark, J. (2022). Fluorine-Free Electrolytes for Lithium and Sodium Batteries. Batteries & Supercaps *5*, e202100373. 10.1002/batt.202100373.
21. Zhang, J., Ma, S., Zhang, J., Zhang, J., Wang, X., Wen, L., Tang, G., Hu, M., Wang, E., and Chen, W. (2024). Critical review on cathode electrolyte interphase towards stabilization for

sodium-ion batteries. Nano Energy *128*, 109814. 10.1016/j.nanoen.2024.109814.

22. Hijazi, H., Desai, P., and Mariyappan, S. (2021). Non-Aqueous Electrolytes for Sodium-Ion Batteries: Challenges and Prospects Towards Commercialization. Batteries & Supercaps *4*, 881-896. 10.1002/batt.202000277.
23. Eshetu, G.G., Elia, G.A., Armand, M., Forsyth, M., Komaba, S., Rojo, T., and Passerini, S. (2020). Electrolytes and Interphases in Sodium-Based Rechargeable Batteries: Recent Advances and Perspectives. Advanced Energy Materials *10*, 2000093. 10.1002/aenm.202000093.
24. Liu, L., Xiao, L., Sun, Z., Bashir, S., Kasi, R., Gu, Y., and Subramaniam, R. (2024). Rational manipulation of electrolyte to induce homogeneous SEI on hard carbon anode for sodium-ion battery. Journal of Energy Chemistry *94*, 414-429. 10.1016/j.jechem.2024.02.055.
25. Rao, R., Chen, L., Su, J., Cai, S., Wang, S., and Chen, Z. (2023). Issues and challenges facing aqueous sodium-ion batteries toward practical applications. Battery Energy *3*, 20230036. 10.1002/bte2.20230036.
26. Wang, S., Peng, B., Lu, J., Jie, Y., Li, X., Pan, Y., Han, Y., Cao, R., Xu, D., and Jiao, S. (2023). Recent Progress in Rechargeable Sodium Metal Batteries: A Review. Chemistry-A European Journal *29*, e202202380. 10.1002/chem.202202380.
27. Lin, Z., Xia, Q., Wang, W., Li, W., and Chou, S. (2019). Recent research progresses in ether- and ester-based electrolytes for sodium-ion batteries. InfoMat *1*, 376-389. 10.1002/inf2.12023.
28. Wu, Y., Wu, L., Wu, S., Yao, Y., Feng, Y., and Yu, Y. (2021). Status and Challenges of Cathode Materials for Room-Temperature Sodium–Sulfur Batteries. Small Science *1*, 2100059. 10.1002/smsc.202100059.
29. Huang, Z., Jaumaux, P., Sun, B., Guo, X., Zhou, D., Shanmukaraj, D., Armand, M., Rojo, T., and Wang, G. (2023). High-Energy Room-Temperature Sodium–Sulfur and Sodium–Selenium Batteries for Sustainable Energy Storage. Electrochemical Energy Reviews *6*, 6:21. 10.1007/s41918-023-00182-w.
30. Qiu, Y., and Xu, J. (2023). Challenges and prospects for room temperature solid-state sodium-sulfur batteries. Nano Research *17*, 1402-1426. 10.1007/s12274-023-5993-3.

31. Ni, J., Liu, Y., and Zhu, S. (2023). Unconventional Designs for Functional Sodium-Sulfur Batteries. Energy & Environmental Materials *6*, e12589. 10.1002/eem2.12589.

32. Xin, S., Yin, Y.X., Guo, Y.G., and Wan, L.J. (2014). A high-energy room-temperature sodium-sulfur battery. Advanced Materials *26*, 1261-1265. 10.1002/adma.201304126.

33. Kousksou, T., Bruel, P., Jamil, A., El Rhafiki, T., and Zeraouli, Y. (2014). Energy storage: Applications and challenges. Solar Energy Materials and Solar Cells *120*, 59-80. 10.1016/j.solmat.2013.08.015.

34. Wang, Y.X., Lai, W.H., Wang, Y.X., Chou, S.L., Ai, X., Yang, H., and Cao, Y. (2019). Sulfur-Based Electrodes that Function via Multielectron Reactions for Room-Temperature Sodium-Ion Storage. Angewandte Chemie International Edition in English *58*, 18324-18337. 10.1002/anie.201902552.

35. Eng, A.Y.S., Kumar, V., Zhang, Y., Luo, J., Wang, W., Sun, Y., Li, W., and Seh, Z.W. (2021). Room-Temperature Sodium–Sulfur Batteries and Beyond: Realizing Practical High Energy Systems through Anode, Cathode, and Electrolyte Engineering. Advanced Energy Materials *11*, 2003493. 10.1002/aenm.202003493.

36. Gao, W., Lu, Y., Xiong, X., Luo, Z., Yu, Y., Lu, Y., Ullah, S., Wang, T., Ma, Y., Zhong, Y., et al. (2024). Review on suppressing the shuttle effect for room-temperature sodium-sulfur batteries. Chemical Engineering Journal *498*, 155230. 10.1016/j.cej.2024.155230.

37. Aslfattahi, N., Samylingam, L., Kiai, M.S., Kadirgama, K., Kulish, V., Schmirler, M., and Said, Z. (2023). State-of-the-art review on electrolytes for sodium-ion batteries: Potential recent progress and technical challenges. Journal of Energy Storage *72*, 108781. 10.1016/j.est.2023.108781..

38. Hueso, K.B., Palomares, V., Armand, M., and Rojo, T. (2017). Challenges and perspectives on high and intermediate-temperature sodium batteries. Nano Research *10*, 4082-4114. 10.1007/s12274-017-1602-7.

39. Sun, Y., Shi, P., Xiang, H., Liang, X., and Yu, Y. (2019). High-Safety Nonaqueous Electrolytes and Interphases for Sodium-Ion Batteries. Small *15*, e1805479. 10.1002/smll.201805479.

40. Xing, Z., Zhao, W., Yu, B., Wang, Y., Zhou, L., Xiong, P., Chen, M., and Zhu, J. (2024). Electrolyte Design Strategies for Aqueous Sodium-Ion Batteries: Progress and Prospects. Small *20*, e2405442. 10.1002/smll.202405442.

41. Xiao, L., Lu, H., Fang, Y., Sushko, M.L., Cao, Y., Ai, X., Yang, H., and Liu, J. (2018). Low-Defect and Low-Porosity Hard Carbon with High Coulombic Efficiency and High Capacity for Practical Sodium Ion Battery Anode. Advanced Energy Materials *8*, 1703238. 10.1002/aenm.201703238.

42. Xiao, Y., Zhu, Y.F., Yao, H.R., Wang, P.F., Zhang, X.D., Li, H., Yang, X., Gu, L., Li, Y.C., Wang, T., et al. (2019). A Stable Layered Oxide Cathode Material for High-Performance Sodium-Ion Battery. Advanced Energy Materials *9*, 1803978. 10.1002/aenm.201803978.

43. Xie, D., Zhang, M., Wu, Y., Xiang, L., and Tang, Y. (2019). A Flexible Dual-Ion Battery Based on Sodium-Ion Quasi-Solid-State Electrolyte with Long Cycling Life. Advanced Functional Materials *30*, 1906770. 10.1002/adfm.201906770.

44. Goodenough, J.B. (2018). How we made the Li-ion rechargeable battery. Nature Electronics *1*, 204-204. 10.1038/s41928-018-0048-6.

45. Jache, B., and Adelhelm, P. (2014). Use of graphite as a highly reversible electrode with superior cycle life for sodium-ion batteries by making use of co-intercalation phenomena. Angewandte Chemie International Edition in English *53*, 10169-10173. 10.1002/anie.201403734.

46. Hu, Y.-S., and Lu, Y. (2020). The Mystery of Electrolyte Concentration: From Superhigh to Ultralow. ACS Energy Letters *5*, 3633-3636. 10.1021/acsenergylett.0c02234.

47. McKinnon, W.R., and Dahn, J.R. (1985). How to Reduce the Cointercalation of Propylene Carbonate in Lix ZrS2 and Other Layered Compounds. Journal of The Electrochemical Society *132*, 364–366. 10.1149/1.2113839.

48. C. A. Angell, Liu, C., and Sanchez, E. (1993). Rubbery solid electrolytes with dominant cationic transport and high ambient conductivity. Nature *362*, 137–139. 10.1038/362137a0.

49. Jeong, S.-K., Inaba, M., Iriyama, Y., Abe, T., and Ogumib, Z. (2003). Electrochemical Intercalation of Lithium Ion within Graphite from Propylene Carbonate Solutions. Electrochemical and Solid-State Letters *6*, A13. 10.1149/1.1526781.

50. Hu, Y. (2004). Novel room temperature molten salt electrolyte based on LiTFSI and acetamide for lithium batteries. Electrochemistry Communications *6*, 28-32. 10.1016/j.elecom.2003.10.009.

51. Tamura, T., Hachida, T., Yoshida, K., Tachikawa, N., Dokko, K., and Watanabe, M. (2010).

New glyme–cyclic imide lithium salt complexes as thermally stable electrolytes for lithium batteries. Journal of Power Sources *195*, 6095-6100. 10.1016/j.jpowsour.2009.11.061.

52. Suo, L., Hu, Y.S., Li, H., Armand, M., and Chen, L. (2013). A new class of Solvent-in-Salt electrolyte for high-energy rechargeable metallic lithium batteries. Nature Communications *4*, 1481. 10.1038/ncomms2513.
53. Mandai, T., Yoshida, K., Ueno, K., Dokko, K., and Watanabe, M. (2014). Criteria for solvate ionic liquids. Physical Chemistry Chemical Physics *16*, 8761-8772. 10.1039/c4cp00461b.
54. Messaggi, F., Ruggeri, I., Genovese, D., Zaccheroni, N., Arbizzani, C., and Soavi, F. (2017). Oxygen Redox Reaction in Lithium-based Electrolytes: from Salt-in-Solvent to Solvent-in-Salt. Electrochimica Acta *245*, 296-302. 10.1016/j.electacta.2017.05.133.
55. Yamada, Y., Wang, J., Ko, S., Watanabe, E., and Yamada, A. (2019). Advances and issues in developing salt-concentrated battery electrolytes. Nature Energy *4*, 269-280. 10.1038/s41560-019-0336-z.
56. Li, M., Wang, C., Chen, Z., Xu, K., and Lu, J. (2020). New Concepts in Electrolytes. Chemical Reviews *120*, 6783-6819. 10.1021/acs.chemrev.9b00531.
57. Borodin, O., Self, J., Persson, K.A., Wang, C., and Xu, K. (2020). Uncharted Waters: Super-Concentrated Electrolytes. Joule *4*, 69-100. 10.1016/j.joule.2019.12.007.
58. Suo, L., Borodin, O., Gao, T., Olguin, M., Ho, J., Fan, X., Luo, C., Wang, C., and Xu, K. (2015). “Water-in-salt” electrolyte enables high-voltage aqueous lithium-ion chemistries. Science *350*, 938–943. 10.1126/science.aab1595.
59. Chen, S., Zheng, J., Mei, D., Han, K.S., Engelhard, M.H., Zhao, W., Xu, W., Liu, J., and Zhang, J.G. (2018). High-Voltage Lithium-Metal Batteries Enabled by Localized High-Concentration Electrolytes. Advanced Materials *30*, e1706102. 10.1002/adma.201706102.
60. Li, Y., Yang, Y., Lu, Y., Zhou, Q., Qi, X., Meng, Q., Rong, X., Chen, L., and Hu, Y.-S. (2020). Ultralow-Concentration Electrolyte for Na-Ion Batteries. ACS Energy Letters *5*, 1156-1158. 10.1021/acsenergylett.0c00337.
61. Yamada, Y., Furukawa, K., Sodeyama, K., Kikuchi, K., Yaegashi, M., Tateyama, Y., and Yamada, A. (2014). Unusual stability of acetonitrile-based superconcentrated electrolytes for fast-charging lithium-ion batteries. Journal of the American Chemical Society *136*, 5039-5046. 10.1021/ja412807w.

62. Wang, J., Yamada, Y., Sodeyama, K., Chiang, C.H., Tateyama, Y., and Yamada, A. (2016). Superconcentrated electrolytes for a high-voltage lithium-ion battery. Nature Communications *7*, 12032. 10.1038/ncomms12032.

63. Suo, L., Xue, W., Gobet, M., Greenbaum, S.G., Wang, C., Chen, Y., Yang, W., Li, Y., and Li, J. (2018). Fluorine-donating electrolytes enable highly reversible 5-V-class Li metal batteries. Proceedings of the National Academy of Sciences of the United States of America *115*, 1156-1161. 10.1073/pnas.1712895115.

64. Wang, J., Yamada, Y., Sodeyama, K., Watanabe, E., Takada, K., Tateyama, Y., and Yamada, A. (2017). Fire-extinguishing organic electrolytes for safe batteries. Nature Energy *3*, 22-29. 10.1038/s41560-017-0033-8.

65. Wu, F., Chu, F., Ferrero, G.A., Sevilla, M., Fuertes, A.B., Borodin, O., Yu, Y., and Yushin, G. (2020). Boosting High-Performance in Lithium-Sulfur Batteries via Dilute Electrolyte. Nano Letters *20*, 5391-5399. 10.1021/acs.nanolett.0c01778.

66. Liu, Q., Feng, Y.-H., Zhu, X., Liu, M., Yu, L., Wei, G.-X., Fan, X.-Y., Ji, X., Wang, P.-F., and Xin, H. (2024). Stabilizing cathode-electrolyte interphase by localized high-concentration electrolytes for high-voltage sodium-ion batteries. Nano Energy *123*, 109389. 10.1016/j.nanoen.2024.109389.

67. Jiang, L.L., Yan, C., Yao, Y.X., Cai, W., Huang, J.Q., and Zhang, Q. (2021). Inhibiting Solvent Co-Intercalation in a Graphite Anode by a Localized High-Concentration Electrolyte in Fast-Charging Batteries. Angewandte Chemie International Edition in English *60*, 3402-3406. 10.1002/anie.202009738.

68. Chu, F., Wang, M., Liu, J., Guan, Z., Yu, H., Liu, B., and Wu, F. (2022). Low Concentration Electrolyte Enabling Cryogenic Lithium–Sulfur Batteries. Advanced Functional Materials *32*, 2205393. 10.1002/adfm.202205393.

69. Deng, R., Chu, F., Kwofie, F., Guan, Z., Chen, J., and Wu, F. (2022). A Low-Concentration Electrolyte for High-Voltage Lithium-Metal Batteries: Fluorinated Solvation Shell and Low Salt Concentration Effect. Angewandte Chemie International Edition in English *61*, e202215866. 10.1002/anie.202215866.

70. Jin, Y., Xu, Y., Le, P.M.L., Vo, T.D., Zhou, Q., Qi, X., Engelhard, M.H., Matthews, B.E., Jia, H., Nie, Z., et al. (2020). Highly Reversible Sodium Ion Batteries Enabled by Stable Electrolyte-Electrode Interphases. ACS Energy Letters *5*, 3212-3220.

10.1021/acsenergylett.0c01712.

71. Zhang, H., Liu, X., Li, H., Hasa, I., and Passerini, S. (2021). Challenges and Strategies for High-Energy Aqueous Electrolyte Rechargeable Batteries. Angewandte Chemie International Edition in English *60*, 598-616. 10.1002/anie.202004433.

72. Zhou, Y., Su, M., Yu, X., Zhang, Y., Wang, J.G., Ren, X., Cao, R., Xu, W., Baer, D.R., Du, Y., et al. (2020). Real-time mass spectrometric characterization of the solid-electrolyte interphase of a lithium-ion battery. Nature Nanotechnology *15*, 224-230. 10.1038/s41565-019-0618-4.

73. Markevich, E., Salitra, G., Chesneau, F., Schmidt, M., and Aurbach, D. (2017). Very Stable Lithium Metal Stripping–Plating at a High Rate and High Areal Capacity in Fluoroethylene Carbonate-Based Organic Electrolyte Solution. ACS Energy Letters *2*, 1321-1326. 10.1021/acsenergylett.7b00300.

74. Yamada, Y., Usui, K., Sodeyama, K., Ko, S., Tateyama, Y., and Yamada, A. (2016). Hydrate-melt electrolytes for high-energy-density aqueous batteries. Nature Energy *1*, 16129. 10.1038/nenergy.2016.129.

75. Suo, L., Borodin, O., Wang, Y., Rong, X., Sun, W., Fan, X., Xu, S., Schroeder, M.A., Cresce, A.V., Wang, F., et al. (2017). "Water-in-Salt" Electrolyte Makes Aqueous Sodium-Ion Battery Safe, Green, and Long-Lasting. Advanced Energy Materials *7*, 1701189. 10.1002/aenm.201701189.

76. Chen, L., Zhang, J., Li, Q., Vatamanu, J., Ji, X., Pollard, T.P., Cui, C., Hou, S., Chen, J., Yang, C., et al. (2020). A 63 m Superconcentrated Aqueous Electrolyte for High-Energy Li-Ion Batteries. ACS Energy Letters *5*, 968-974. 10.1021/acsenergylett.0c00348.

77. Lee, M.H., Kim, S.J., Chang, D., Kim, J., Moon, S., Oh, K., Park, K.-Y., Seong, W.M., Park, H., Kwon, G., et al. (2019). Toward a low-cost high-voltage sodium aqueous rechargeable battery. Materials Today *29*, 26-36. 10.1016/j.mattod.2019.02.004.

78. Liu, D., Li, Z., Li, X., Cheng, Z., Yuan, L., and Huang, Y. (2019). Recent Advances in Cathode Materials for Room-Temperature Sodium-Sulfur Batteries. Chemphyschem *20*, 3164-3176. 10.1002/cphc.201900595.

79. Chen, P., Wang, C., and Wang, T. (2022). Review and prospects for room-temperature sodium-sulfur batteries. Materials Research Letters *10*, 691-719. 10.1080/21663831.2022.2092428.

80. Ye, C., Jiao, Y., Chao, D., Ling, T., Shan, J., Zhang, B., Gu, Q., Davey, K., Wang, H., and Qiao, S.Z. (2020). Electron-State Confinement of Polysulfides for Highly Stable Sodium-Sulfur Batteries. Advanced Materials *32*, e1907557. 10.1002/adma.201907557.
81. Luo, J., Lu, X., Matios, E., Wang, C., Wang, H., Zhang, Y., Hu, X., and Li, W. (2020). Tunable MXene-Derived 1D/2D Hybrid Nanoarchitectures as a Stable Matrix for Dendrite-Free and Ultrahigh Capacity Sodium Metal Anode. Nano Letters *20*, 7700-7708. 10.1021/acs.nanolett.0c03215.
82. Wang, Y., Shi, H., Niu, J., Mai, W., Liu, L., and Xu, Z. (2021). Self-healing Sn4P3@Hard carbon Co-storage anode for sodium-ion batteries. Journal of Alloys and Compounds *851*, 156746. 10.1016/j.jallcom.2020.156746.
83. Sun, B., Li, P., Zhang, J., Wang, D., Munroe, P., Wang, C., Notten, P.H.L., and Wang, G. (2018). Dendrite-Free Sodium-Metal Anodes for High-Energy Sodium-Metal Batteries. Advanced Materials *30*, e1801334. 10.1002/adma.201801334.
84. Park, K., Cho, J.H., Jang, J.-H., Yu, B.-C., De La Hoz, A.T., Miller, K.M., Ellison, C.J., and Goodenough, J.B. (2015). Trapping lithium polysulfides of a Li–S battery by forming lithium bonds in a polymer matrix. Energy & Environmental Science *8*, 2389-2395. 10.1039/c5ee01809a.
85. Wu, C., Lai, W.H., Cai, X., Chou, S.L., Liu, H.K., Wang, Y.X., and Dou, S.X. (2021). Carbonaceous Hosts for Sulfur Cathode in Alkali-Metal/S (Alkali Metal = Lithium, Sodium, Potassium) Batteries. Small *17*, e2006504. 10.1002/smll.202006504.
86. Kairies, K.-P., Figgener, J., Haberschusz, D., Wessels, O., Tepe, B., and Sauer, D.U. (2019). Market and technology development of PV home storage systems in Germany. Journal of Energy Storage *23*, 416-424. 10.1016/j.est.2019.02.023.
87. Liu, H., Lai, W.H., Lei, Y., Yang, H., Wang, N., Chou, S., Liu, H.K., Dou, S.X., and Wang, Y.X. (2022). Electrolytes/Interphases: Enabling Distinguishable Sulfur Redox Processes in Room-Temperature Sodium-Sulfur Batteries. Advanced Energy Materials *12*, 2103304. 10.1002/aenm.202103304.
88. Yu, X., and Manthiram, A. (2014). Capacity Enhancement and Discharge Mechanisms of Room-Temperature Sodium–Sulfur Batteries. ChemElectroChem *1*, 1275-1280. 10.1002/celc.201402112.
89. Zhang, H., Diemant, T., Qin, B., Li, H., Behm, R.J., and Passerini, S. (2020). Solvent-

Dictated Sodium Sulfur Redox Reactions: Investigation of Carbonate and Ether Electrolytes. Energies *13*, 836. 10.3390/en13040836.

90. Zhang, J., Wang, D.W., Lv, W., Qin, L., Niu, S., Zhang, S., Cao, T., Kang, F., and Yang, Q.H. (2018). Ethers Illume Sodium-Based Battery Chemistry: Uniqueness, Surprise, and Challenges. Advanced Energy Materials *8*, 1801361. 10.1002/aenm.201801361.

91. Wan, B., Xu, S., Yuan, X., Tang, H., Huang, D., Zhou, W., Wu, L., Zhang, J., and Gou, H. (2019). Diversities of stoichiometry and electrical conductivity in sodium sulfides. Journal of Materials Chemistry A *7*, 16472-16478. 10.1039/c9ta05907e.

92. Zhang, D., Li, B., Wang, S., and Yang, S. (2017). Simultaneous Formation of Artificial SEI Film and 3D Host for Stable Metallic Sodium Anodes. ACS Applied Materials & Interfaces *9*, 40265-40272. 10.1021/acsami.7b12568.

93. Zheng, M., Chi, Y., Hu, Q., Tang, H., Jiang, X., Zhang, L., Zhang, S., Pang, H., and Xu, Q. (2019). Carbon nanotube-based materials for lithium–sulfur batteries. Journal of Materials Chemistry A *7*, 17204-17241. 10.1039/c9ta05347f.

94. Yan, Z., Tian, Q., Liang, Y., Jing, L., Hu, Z., Hua, W., Tayal, A., Lai, W., Wang, W., Peng, J., et al. (2021). Electrochemical release of catalysts in nanoreactors for solid sulfur redox reactions in room-temperature sodium-sulfur batteries. Cell Reports Physical Science *2*, 100539. 10.1016/j.xcrp.2021.100539.

95. Sun, B., Xiong, P., Maitra, U., Langsdorf, D., Yan, K., Wang, C., Janek, J., Schroder, D., and Wang, G. (2020). Design Strategies to Enable the Efficient Use of Sodium Metal Anodes in High-Energy Batteries. Advanced Materials *32*, e1903891. 10.1002/adma.201903891.

96. Wu, X., Qian, C., Wu, H., Xu, L., Bu, L., Piao, Y., Diao, G., and Chen, M. (2020). Gestated uniform yolk-shell Sn@N-doped hollow mesoporous carbon spheres with buffer space for boosting lithium storage performance. Chemical Communications *56*, 7629-7632. 10.1039/d0cc02443k.

97. Eng, A.Y.S., Nguyen, D.-T., Kumar, V., Subramanian, G.S., Ng, M.-F., and Seh, Z.W. (2020). Tailoring binder–cathode interactions for long-life room-temperature sodium–sulfur batteries. Journal of Materials Chemistry A *8*, 22983-22997. 10.1039/d0ta07681c.

98. Kim, I., Kim, C.H., Choi, S.h., Ahn, J.-P., Ahn, J.-H., Kim, K.-W., Cairns, E.J., and Ahn, H.-J. (2016). A singular flexible cathode for room temperature sodium/sulfur battery.

Journal of Power Sources *307*, 31-37. 10.1016/j.jpowsour.2015.12.035.

99. Salama, M., Rosy, Attias, R., Yemini, R., Gofer, Y., Aurbach, D., and Noked, M. (2019). Metal–Sulfur Batteries: Overview and Research Methods. ACS Energy Letters *4*, 436-446. 10.1021/acsenergylett.8b02212.

100. Nersisyan, H.H., Joo, S.H., Yoo, B.U., Kim, D.Y., Lee, T.H., Eom, J.-Y., Kim, C., Lee, K.H., and Lee, J.-H. (2016). Combustion-mediated synthesis of hollow carbon nanospheres for high-performance cathode material in lithium-sulfur battery. Carbon *103*, 255-262. 10.1016/j.carbon.2016.03.022.

101. Tzadikov, J., Levy, N.R., Abisdris, L., Cohen, R., Weitman, M., Kaminker, I., Goldbourt, A., Ein‐Eli, Y., and Shalom, M. (2020). Bottom‐Up Synthesis of Advanced Carbonaceous Anode Materials Containing Sulfur for Na‐Ion Batteries. Advanced Functional Materials *30*, 2000592. 10.1002/adfm.202000592.

102. Wu, X.W., Xie, H., Deng, Q., Wang, H.X., Sheng, H., Yin, Y.X., Zhou, W.X., Li, R.L., and Guo, Y.G. (2017). Three-Dimensional Carbon Nanotubes Forest/Carbon Cloth as an Efficient Electrode for Lithium-Polysulfide Batteries. ACS Applied Materials & Interfaces *9*, 1553-1561. 10.1021/acsami.6b14687.

103. Wang, Y.X., Yang, J., Lai, W., Chou, S.L., Gu, Q.F., Liu, H.K., Zhao, D., and Dou, S.X. (2016). Achieving High-Performance Room-Temperature Sodium-Sulfur Batteries With S@Interconnected Mesoporous Carbon Hollow Nanospheres. Journal of the American Chemical Society *138*, 16576-16579. 10.1021/jacs.6b08685.

104. Guo, Q., Li, S., Liu, X., Lu, H., Chang, X., Zhang, H., Zhu, X., Xia, Q., Yan, C., and Xia, H. (2020). Ultrastable Sodium-Sulfur Batteries without Polysulfides Formation Using Slit Ultramicropore Carbon Carrier. Advanced Science *7*, 1903246. 10.1002/advs.201903246.

105. Wu, C., Lei, Y., Simonelli, L., Tonti, D., Black, A., Lu, X., Lai, W.H., Cai, X., Wang, Y.X., Gu, Q., et al. (2022). Continuous Carbon Channels Enable Full Na-Ion Accessibility for Superior Room-Temperature Na-S Batteries. Advanced Materials *34*, e2108363. 10.1002/adma.202108363.

106. Eng, A.Y.S., Wang, Y., Nguyen, D.T., Tee, S.Y., Lim, C.Y.J., Tan, X.Y., Ng, M.F., Xu, J., and Seh, Z.W. (2021). Tunable Nitrogen-Doping of Sulfur Host Nanostructures for Stable and Shuttle-Free Room-Temperature Sodium-Sulfur Batteries. Nano Letters *21*, 5401-5408. 10.1021/acs.nanolett.1c01763.

107. Ni, L., Wu, Z., Zhao, G., Sun, C., Zhou, C., Gong, X., and Diao, G. (2017). Core-Shell Structure and Interaction Mechanism of gamma-MnO(2) Coated Sulfur for Improved Lithium-Sulfur Batteries. Small *13*, 1603466. 10.1002/smll.201603466.

108. Zhang, L., Zhang, B., Dou, Y., Wang, Y., Al-Mamun, M., Hu, X., and Liu, H. (2018). Self-Assembling Hollow Carbon Nanobeads into Double-Shell Microspheres as a Hierarchical Sulfur Host for Sustainable Room-Temperature Sodium-Sulfur Batteries. ACS Applied Materials & Interfaces *10*, 20422-20428. 10.1021/acsami.8b03850.

109. Zhang, X., Zhao, R., Wu, Q., Li, W., Shen, C., Ni, L., Yan, H., Diao, G., and Chen, M. (2017). Petal-like MoS(2) Nanosheets Space-Confined in Hollow Mesoporous Carbon Spheres for Enhanced Lithium Storage Performance. ACS Nano *11*, 8429-8436. 10.1021/acsnano.7b04078.

110. Aslam, M.K., Seymour, I.D., Katyal, N., Li, S., Yang, T., Bao, S.J., Henkelman, G., and Xu, M. (2020). Metal chalcogenide hollow polar bipyramid prisms as efficient sulfur hosts for Na-S batteries. Nature Communications *11*, 5242. 10.1038/s41467-020-19078-0.

111. Bao, C., Wang, B., Liu, P., Wu, H., Zhou, Y., Wang, D., Liu, H., and Dou, S. (2020). Solid Electrolyte Interphases on Sodium Metal Anodes. Advanced Functional Materials *30*, 2004891. 10.1002/adfm.202004891.

112. Basile, A., Hilder, M., Makhlooghiazad, F., Pozo-Gonzalo, C., MacFarlane, D.R., Howlett, P.C., and Forsyth, M. (2018). Ionic Liquids and Organic Ionic Plastic Crystals: Advanced Electrolytes for Safer High Performance Sodium Energy Storage Technologies. Advanced Energy Materials *8*, 1703491. 10.1002/aenm.201703491.

113. Wang, Y.X., Lai, W.H., Chou, S.L., Liu, H.K., and Dou, S.X. (2020). Remedies for Polysulfide Dissolution in Room-Temperature Sodium-Sulfur Batteries. Advanced Materials *32*, e1903952. 10.1002/adma.201903952.

114. Fan, L., and Li, X. (2018). Recent advances in effective protection of sodium metal anode. Nano Energy *53*, 630-642. 10.1016/j.nanoen.2018.09.017.

115. Lee, B., Paek, E., Mitlin, D., and Lee, S.W. (2019). Sodium Metal Anodes: Emerging Solutions to Dendrite Growth. Chemical Reviews *119*, 5416-5460. 10.1021/acs.chemrev.8b00642.

116. Nayak, P.K., Yang, L., Brehm, W., and Adelhelm, P. (2018). From Lithium-Ion to Sodium-Ion Batteries: Advantages, Challenges, and Surprises. Angewandte Chemie International

Edition in English *57*, 102-120. 10.1002/anie.201703772.

117. Delmas, C. (2018). Sodium and Sodium-Ion Batteries: 50 Years of Research. Advanced Energy Materials *8*, 1703137. 10.1002/aenm.201703137.

118. Kim, S.-W., Seo, D.-H., Ma, X., Ceder, G., and Kang, K. (2012). Electrode Materials for Rechargeable Sodium-Ion Batteries: Potential Alternatives to Current Lithium-Ion Batteries. Advanced Energy Materials *2*, 710-721. 10.1002/aenm.201200026.

119. Deng, J., Luo, W.-B., Chou, S.-L., Liu, H.-K., and Dou, S.-X. (2018). Sodium-Ion Batteries: From Academic Research to Practical Commercialization. Advanced Energy Materials *8*, 1701428. 10.1002/aenm.201701428.

120. Slater, M.D., Kim, D., Lee, E., and Johnson, C.S. (2013). Sodium-Ion Batteries. Advanced Functional Materials *23*, 947-958. 10.1002/adfm.201200691.

121. Che, H., Chen, S., Xie, Y., Wang, H., Amine, K., Liao, X.-Z., and Ma, Z.-F. (2017). Electrolyte design strategies and research progress for room-temperature sodium-ion batteries. Energy & Environmental Science *10*, 1075-1101. 10.1039/c7ee00524e.

122. Sun, H., Zhu, G., Zhu, Y., Lin, M.C., Chen, H., Li, Y.Y., Hung, W.H., Zhou, B., Wang, X., Bai, Y., et al. (2020). High-Safety and High-Energy-Density Lithium Metal Batteries in a Novel Ionic-Liquid Electrolyte. Advanced Materials *32*, e2001741. 10.1002/adma.202001741.

123. Zheng, X., Gu, Z., Liu, X., Wang, Z., Wen, J., Wu, X., Luo, W., and Huang, Y. (2020). Bridging the immiscibility of an all-fluoride fire extinguishant with highly-fluorinated electrolytes toward safe sodium metal batteries. Energy & Environmental Science *13*, 1788-1798. 10.1039/d0ee00694g.

124. Wongittharom, N., Lee, T.-C., Wang, C.-H., Wang, Y.-C., and Chang, J.-K. (2014). Electrochemical performance of Na/NaFePO4 sodium-ion batteries with ionic liquid electrolytes. Journal of Materials Chemistry A *2*, 5655–5661. 10.1039/c3ta15273a.

125. Liu, Y., Lu, S., Wang, Z., Xu, J., Weng, S., Xue, J., Tu, H., Zhang, F., Liu, L., Gao, Y., et al. (2024). Weakly Polar Ether‐Aided Ionic Liquid Electrolyte Enables High‐Performance Sodium Metal Batteries over Wide Temperature Range. Advanced Functional Materials *34*, 2312295. 10.1002/adfm.202312295.

126. Chen, J., Yang, Z., Xu, X., Qiao, Y., Zhou, Z., Hao, Z., Chen, X., Liu, Y., Wu, X., Zhou, X., et al. (2024). Nonflammable Succinonitrile-Based Deep Eutectic Electrolyte for

Intrinsically Safe High-Voltage Sodium-Ion Batteries. Advanced Materials *36*, e2400169. 10.1002/adma.202400169.

127. Martinez, L., Andrade, R., Birgin, E.G., and Martinez, J.M. (2009). PACKMOL: a package for building initial configurations for molecular dynamics simulations. Journal of Computational Chemistry *30*, 2157-2164. 10.1002/jcc.21224.

128. Jorgensen, W.L., Maxwell, D.S., and Tirado-Rives, J. (1996). Development and Testing of the OPLS All-Atom Force Field on Conformational Energetics and Properties of Organic Liquids. Journal of the American Chemical Society *118*, 11225-11236. 10.1021/ja9621760.

129. Saito, S., Watanabe, H., Ueno, K., Mandai, T., Seki, S., Tsuzuki, S., Kameda, Y., Dokko, K., Watanabe, M., and Umebayashi, Y. (2016). Li(+) Local Structure in Hydrofluoroether Diluted Li-Glyme Solvate Ionic Liquid. Journal of Physical Chemistry B *120*, 3378-3387. 10.1021/acs.jpcb.5b12354.

130. Doherty, B., Zhong, X., Gathiaka, S., Li, B., and Acevedo, O. (2017). Revisiting OPLS Force Field Parameters for Ionic Liquid Simulations. Journal of Chemical Theory and Computation *13*, 6131-6145. 10.1021/acs.jctc.7b00520.

131. Sambasivarao, S.V., and Acevedo, O. (2009). Development of OPLS-AA Force Field Parameters for 68 Unique Ionic Liquids. Journal of Chemical Theory and Computation *5*, 1038-1050. 10.1021/ct900009a.

132. Abraham, M.J., Murtola, T., Schulz, R., Páll, S., Smith, J.C., Hess, B., and Lindahl, E. (2015). GROMACS: High performance molecular simulations through multi-level parallelism from laptops to supercomputers. SoftwareX *1-2*, 19-25. 10.1016/j.softx.2015.06.001.

133. Van Der Spoel, D., Lindahl, E., Hess, B., Groenhof, G., Mark, A.E., and Berendsen, H.J. (2005). GROMACS: fast, flexible, and free. Journal of Computational Chemistry *26*, 1701-1718. 10.1002/jcc.20291.

134. Zhang, X.Q., Cheng, X.B., Chen, X., Yan, C., and Zhang, Q. (2017). Fluoroethylene Carbonate Additives to Render Uniform Li Deposits in Lithium Metal Batteries. Advanced Functional Materials *27*, 1605989. 10.1002/adfm.201605989.

135. Jaumann, T., Balach, J., Langklotz, U., Sauchuk, V., Fritsch, M., Michaelis, A., Teltevskij, V., Mikhailova, D., Oswald, S., Klose, M., et al. (2017). Lifetime vs. rate capability: Understanding the role of FEC and VC in high-energy Li-ion batteries with nano-silicon

anodes. Energy Storage Materials *6*, 26-35. 10.1016/j.ensm.2016.08.002.

136. Holomb, R., Xu, W., Markusson, H., Johansson, P., and Jacobsson, P. (2006). Vibrational Spectroscopy and ab Initio Studies of Lithium Bis(oxalato)borate (LiBOB) in Different Solvents. Journal of Physical Chemistry A *110*, 11467-11472. 10.1021/jp0626824.
137. Zhang, Q., Zhang, N., Yu, T., Zhang, J., Wen, B., and Zhang, L. (2022). High-performance PEO-based solid-state LiCoO2 lithium metal battery enabled by poly(acrylic acid) artificial cathode electrolyte interface. Materials Today Energy *29*, 101128. 10.1016/j.mtener.2022.101128.
138. Su, L., Zhao, X., Yi, M., Charalambous, H., Celio, H., Liu, Y., and Manthiram, A. (2022). Uncovering the Solvation Structure of $LiPF_6$-Based Localized Saturated Electrolytes and Their Effect on $LiNiO_2$-Based Lithium-Metal Batteries. Advanced Energy Materials *12*, 2201911. 10.1002/aenm.202201911.
139. Moon, J., Kim, D.O., Bekaert, L., Song, M., Chung, J., Lee, D., Hubin, A., and Lim, J. (2022). Non-fluorinated non-solvating cosolvent enabling superior performance of lithium metal negative electrode battery. Nature Communications *13*, 4538. 10.1038/s41467-022-32192-5.
140. Hou, T., Fong, K.D., Wang, J., and Persson, K.A. (2021). The solvation structure, transport properties and reduction behavior of carbonate-based electrolytes of lithium-ion batteries. Chemical Science *12*, 14740-14751. 10.1039/d1sc04265c.
141. Zhu, Y., Xu, Y., Liu, Y., Luo, C., and Wang, C. (2013). Comparison of electrochemical performances of olivine NaFePO4 in sodium-ion batteries and olivine $LiFePO_4$ in lithium-ion batteries. Nanoscale *5*, 780-787. 10.1039/c2nr32758a.
142. Rahman, M.M., Sultana, I., Mateti, S., Liu, J., Sharma, N., and Chen, Y. (2017). Maricite NaFePO4/C/graphene: a novel hybrid cathode for sodium-ion batteries. Journal of Materials Chemistry A *5*, 16616-16621. 10.1039/c7ta04946c.
143. Fang, Y., Liu, Q., Xiao, L., Ai, X., Yang, H., and Cao, Y. (2015). High-Performance Olivine NaFePO4 Microsphere Cathode Synthesized by Aqueous Electrochemical Displacement Method for Sodium Ion Batteries. ACS Applied Materials & Interfaces *7*, 17977-17984. 10.1021/acsami.5b04691.
144. Oh, S.-M., Myung, S.-T., Hassoun, J., Scrosati, B., and Sun, Y.-K. (2012). Reversible NaFePO4 electrode for sodium secondary batteries. Electrochemistry Communications *22*,

149-152. 10.1016/j.elecom.2012.06.014.

145. Fang, Y., Xiao, L., Qian, J., Ai, X., Yang, H., and Cao, Y. (2014). Mesoporous amorphous FePO4 nanospheres as high-performance cathode material for sodium-ion batteries. Nano Letters *14*, 3539-3543. 10.1021/nl501152f.

146. Liu, Y., Xu, Y., Han, X., Pellegrinelli, C., Zhu, Y., Zhu, H., Wan, J., Chung, A.C., Vaaland, O., Wang, C., and Hu, L. (2012). Porous amorphous FePO4 nanoparticles connected by single-wall carbon nanotubes for sodium ion battery cathodes. Nano Letters *12*, 5664-5668. 10.1021/nl302819f.

147. Moradi, M., Li, Z., Qi, J., Xing, W., Xiang, K., Chiang, Y.M., and Belcher, A.M. (2015). Improving the capacity of sodium ion battery using a virus-templated nanostructured composite cathode. Nano Letters *15*, 2917-2921. 10.1021/nl504676v.

148. Wang, W., Wang, S., Jiao, H., Zhan, P., and Jiao, S. (2015). A sodium ion intercalation material: a comparative study of amorphous and crystalline $FePO_4$. Physical Chemistry Chemical Physics *17*, 4551-4557. 10.1039/c4cp05764c.

149. Zhang, Z., Du, Y., Wang, Q.C., Xu, J., Zhou, Y.N., Bao, J., Shen, J., and Zhou, X. (2020). A Yolk-Shell-Structured FePO(4) Cathode for High-Rate and Long-Cycling Sodium-Ion Batteries. Angewandte Chemie International Edition in English *59*, 17504-17510. 10.1002/anie.202008318.

150. Feng, J., Zhang, Z., Li, L., Yang, J., Xiong, S., and Qian, Y. (2015). Ether-based nonflammable electrolyte for room temperature sodium battery. Journal of Power Sources *284*, 222-226. 10.1016/j.jpowsour.2015.03.038.

151. Tang, W., Song, X., Du, Y., Peng, C., Lin, M., Xi, S., Tian, B., Zheng, J., Wu, Y., Pan, F., and Loh, K.P. (2016). High-performance NaFePO4formed by aqueous ion-exchange and its mechanism for advanced sodium ion batteries. Journal of Materials Chemistry A *4*, 4882-4892. 10.1039/c6ta01111j.

152. Liu, Y., Zhu, L., Wang, E., An, Y., Liu, Y., Shen, K., He, M., Jia, Y., Ye, G., Xiao, Z., et al. (2024). Electrolyte Engineering with Tamed Electrode Interphases for High-Voltage Sodium-Ion Batteries. Advanced Materials *36*, e2310051. 10.1002/adma.202310051.

153. Cheng, F., Cao, M., Li, Q., Fang, C., Han, J., and Huang, Y. (2023). Electrolyte Salts for Sodium-Ion Batteries: NaPF(6) or NaClO(4)? ACS Nano *17*, 18608-18615. 10.1021/acsnano.3c07474.

154. Li, Q., Cao, Z., Cheng, H., Zhang, J., Ma, Z., Wahyudi, W., Cavallo, L., Sun, Q., and Ming, J. (2022). Electrolyte Boosting Microdumbbell-Structured Alloy/Metal Oxide Anode for Fast-Charging Sodium-Ion Batteries. ACS Materials Letters *4*, 2469-2479. 10.1021/acsmaterialslett.2c00841.

155. Yan, G., Reeves, K., Foix, D., Li, Z., Cometto, C., Mariyappan, S., Salanne, M., and Tarascon, J.M. (2019). A New Electrolyte Formulation for Securing High Temperature Cycling and Storage Performances of Na‐Ion Batteries. Advanced Energy Materials *9*, 1901431. 10.1002/aenm.201901431.

156. Hu, C., Guo, S., Huang, F., Yang, Y., Yan, C., Zhao, C.Z., Liang, S., Fang, G., and Zhang, Q. (2024). Carbonate Ester-Based Sodium Metal Battery with High-Capacity Retention at -50 degrees C Enabled by Weak Solvents and Electrodeposited Anode. Angewandte Chemie International Edition in English *63*, e202407075. 10.1002/anie.202407075.

157. Wang, C., Thenuwara, A.C., Luo, J., Shetty, P.P., McDowell, M.T., Zhu, H., Posada-Perez, S., Xiong, H., Hautier, G., and Li, W. (2022). Extending the low-temperature operation of sodium metal batteries combining linear and cyclic ether-based electrolyte solutions. Nature Communications *13*, 4934. 10.1038/s41467-022-32606-4.

158. Huang, A., Ma, Z., Kumar, P., Liang, H., Cai, T., Zhao, F., Cao, Z., Cavallo, L., Li, Q., and Ming, J. (2024). Low-Temperature and Fast-Charging Lithium Metal Batteries Enabled by Solvent-Solvent Interaction Mediated Electrolyte. Nano Letters *24*, 7499-7507. 10.1021/acs.nanolett.4c01591.

159. Cheng, X.B., Zhang, R., Zhao, C.Z., and Zhang, Q. (2017). Toward Safe Lithium Metal Anode in Rechargeable Batteries: A Review. Chemical Reviews *117*, 10403-10473. 10.1021/acs.chemrev.7b00115.

160. Chen, W., Lei, T., Wu, C., Deng, M., Gong, C., Hu, K., Ma, Y., Dai, L., Lv, W., He, W., et al. (2018). Designing Safe Electrolyte Systems for a High-Stability Lithium-Sulfur Battery. Advanced Energy Materials *8*, 1702348. 10.1002/aenm.201702348.

161. Arumugam Manthiram, Fu, Y., and Su, Y.-S. (2013). Challenges and Prospects of LithiumSulfur Batteries. Accounts of Chemical Research *46*, 1125-1134. 10.1021/ar300179v.

162. Xu, X., Zhou, D., Qin, X., Lin, K., Kang, F., Li, B., Shanmukaraj, D., Rojo, T., Armand, M., and Wang, G. (2018). A room-temperature sodium-sulfur battery with high capacity

and stable cycling performance. Nature Communications *9*, 3870. 10.1038/s41467-018-06443-3.

163. Zhang, S., Yao, Y., and Yu, Y. (2021). Frontiers for Room-Temperature Sodium–Sulfur Batteries. ACS Energy Letters *6*, 529-536. 10.1021/acsenergylett.0c02488.

164. Zhang, Q., Yang, T., and Li, Z. (2024). Mechanism and Kinetics of Na_2S_x ($x \leqslant 2$) Precipitation in Sodium-Sulfur and Sodium/(Oxygen)-Sulfur Batteries. Journal of The Electrochemical Society *171*, 010503. 10.1149/1945-7111/ad14cb.

165. Ye, H., Wang, C.-Y., Zuo, T.-T., Wang, P.-F., Yin, Y.-X., Zheng, Z.-J., Wang, P., Cheng, J., Cao, F.-F., and Guo, Y.-G. (2018). Realizing a highly stable sodium battery with dendrite-free sodium metal composite anodes and O3-type cathodes. Nano Energy *48*, 369-376. 10.1016/j.nanoen.2018.03.069.

166. Wang, N., Wang, Y., Bai, Z., Fang, Z., Zhang, X., Xu, Z., Ding, Y., Xu, X., Du, Y., Dou, S., and Yu, G. (2020). High-performance room-temperature sodium–sulfur battery enabled by electrocatalytic sodium polysulfides full conversion. Energy & Environmental Science *13*, 562-570. 10.1039/c9ee03251g.

167. Zhang, B.W., Sheng, T., Liu, Y.D., Wang, Y.X., Zhang, L., Lai, W.H., Wang, L., Yang, J., Gu, Q.F., Chou, S.L., et al. (2018). Atomic cobalt as an efficient electrocatalyst in sulfur cathodes for superior room-temperature sodium-sulfur batteries. Nature Communications *9*, 4082. 10.1038/s41467-018-06144-x.

168. Xiong, X., Wang, G., Lin, Y., Wang, Y., Ou, X., Zheng, F., Yang, C., Wang, J.H., and Liu, M. (2016). Enhancing Sodium Ion Battery Performance by Strongly Binding Nanostructured Sb(2)S(3) on Sulfur-Doped Graphene Sheets. ACS Nano *10*, 10953-10959. 10.1021/acsnano.6b05653.

169. Li, W., Zhou, M., Li, H., Wang, K., Cheng, S., and Jiang, K. (2015). A high performance sulfur-doped disordered carbon anode for sodium ion batteries. Energy & Environmental Science *8*, 2916-2921. 10.1039/c5ee01985k.

170. Carter, R., Oakes, L., Douglas, A., Muralidharan, N., Cohn, A.P., and Pint, C.L. (2017). A Sugar-Derived Room-Temperature Sodium Sulfur Battery with Long Term Cycling Stability. Nano Letters *17*, 1863-1869. 10.1021/acs.nanolett.6b05172.

171. Xu, J., Lawson, T., Fan, H., Su, D., and Wang, G. (2018). Updated Metal Compounds (MOFs, S, OH, N, C) Used as Cathode Materials for Lithium–Sulfur Batteries.

Advanced Energy Materials *8*, 1702607. 10.1002/aenm.201702607.

172. Yuan, Z., Peng, H.J., Hou, T.Z., Huang, J.Q., Chen, C.M., Wang, D.W., Cheng, X.B., Wei, F., and Zhang, Q. (2016). Powering Lithium-Sulfur Battery Performance by Propelling Polysulfide Redox at Sulfiphilic Hosts. Nano Letters *16*, 519-527. 10.1021/acs.nanolett.5b04166.

173. Liang, X., Hart, C., Pang, Q., Garsuch, A., Weiss, T., and Nazar, L.F. (2015). A highly efficient polysulfide mediator for lithium-sulfur batteries. Nature Communications *6*, 5682. 10.1038/ncomms6682.

174. Zhang, H., Dai, R., Zhu, S., Zhou, L., Xu, Q., and Min, Y. (2022). Bimetallic nitride modified separator constructs internal electric field for high-performance lithium-sulfur battery. Chemical Engineering Journal *429*, 132454. 10.1016/j.cej.2021.132454..

175. Cai, D.Q., Gao, Y.T., Wang, X.Y., Yang, J.L., and Zhao, S.X. (2022). Built-In Electric Field on the Mott-Schottky Heterointerface-Enabled Fast Kinetics Lithium-Sulfur Batteries. ACS Applied Materials & Interfaces *14*, 38651-38659. 10.1021/acsami.2c06676.

176. Xie, K., You, Y., Yuan, K., Lu, W., Zhang, K., Xu, F., Ye, M., Ke, S., Shen, C., Zeng, X., et al. (2017). Ferroelectric-Enhanced Polysulfide Trapping for Lithium-Sulfur Battery Improvement. Advanced Materials *29*, 1604724. 10.1002/adma.201604724.

177. Zhao, Z., Li, G., Wang, Z., Feng, M., Sun, M., Xue, X., Liu, R., Jia, H., Wang, Z., Zhang, W., et al. (2019). Black BaTiO3 as multifunctional sulfur immobilizer for superior lithium sulfur batteries. Journal of Power Sources *434*, 226729. 10.1016/j.jpowsour.2019.226729.

178. Kim, I., Park, J.-Y., Kim, C., Park, J.-W., Ahn, J.-P., Ahn, J.-H., Kim, K.-W., and Ahn, H.-J. (2016). Sodium Polysulfides during Charge/Discharge of the Room-Temperature Na/S Battery Using TEGDME Electrolyte. Journal of The Electrochemical Society *163*, A611-A616. 10.1149/2.0201605jes.

179. Gao, X., Yu, Z., Wang, J., Zheng, X., Ye, Y., Gong, H., Xiao, X., Yang, Y., Chen, Y., Bone, S.E., et al. (2023). Electrolytes with moderate lithium polysulfide solubility for high-performance long-calendar-life lithium-sulfur batteries. Proceedings of the National Academy of Sciences of the United States of America *120*, e2301260120. 10.1073/pnas.2301260120.

180. Adams, B.D., Zheng, J., Ren, X., Xu, W., and Zhang, J.G. (2017). Accurate Determination of Coulombic Efficiency for Lithium Metal Anodes and Lithium Metal Batteries.

Advanced Energy Materials *8*, 1702097. 10.1002/aenm.201702097.

181. Shen, C., Lu, S., Tian, Z., Yang, S., Cardenas, J.A., Li, J., Peng, X., Huang, T.J., Franklin, A.D., and Cummer, S.A. (2021). Electrically Tunable Surface Acoustic Wave Propagation at MHz Frequencies Based on Carbon Nanotube Thin-Film Transistors. Advanced Functional Materials *31*, 2010744. 10.1002/adfm.202010744.

182. Giurgiutiu, V. (2007). Structural Health Monitoring with Piezoelectric Wafer Active Sensors (Elsevier).

183. Qingsong Zhang, Cagin, T., and Goddard, W.A. (2006). The ferroelectric and cubic phases in BaTiO3 ferroelectrics are also antiferroelectric. Proceedings of the National Academy of Sciences of the United States of America *103*, 14695-14700. 10.1073/pnas.0606612103.

184. Wu, J., Tian, Y., Gao, Y., Gao, Z., Meng, Y., Wang, Y., Wang, X., Zhou, D., Kang, F., Li, B., and Wang, G. (2022). Rational Electrolyte Design toward Cyclability Remedy for Room-Temperature Sodium-Sulfur Batteries. Angewandte Chemie International Edition in English *61*, e202205416. 10.1002/anie.202205416.

185. Du, P., Li, B., Mao, Z., Nan, Y., Guo, D., and Wu, S. (2022). Regulating lithium-ion flow by piezoelectric effect of the poled-BaTiO3 film for dendrite-free lithium metal anode. Journal of Electroanalytical Chemistry *919*, 116538. 10.1016/j.jelechem.2022.116538.

186. Hagopian, A., Doublet, M.-L., and Filhol, J.-S. (2020). Thermodynamic origin of dendrite growth in metal anode batteries. Energy & Environmental Science *13*, 5186-5197. 10.1039/d0ee02665d.

187. Alghane, M., Chen, B.X., Fu, Y.Q., Li, Y., Luo, J.K., and Walton, A.J. (2011). Experimental and numerical investigation of acoustic streaming excited by using a surface acoustic wave device on a 128° YX-LiNbO3substrate. Journal of Micromechanics and Microengineering *21*, 015005. 10.1088/0960-1317/21/1/015005.

188. Lighthill, S.J. (1978). Acoustic streaming. Journal of Sound and Vibration *61*, 391–418. 10.1016/0022-460X(78)90388-7.

189. R. Skov, N., S. Bach, J., G. Winckelmann, B., and Bruus, H. (2019). 3D modeling of acoustofluidics in a liquid-filled cavity including streaming, viscous boundary layers, surrounding solids, and a piezoelectric transducer. AIMS Mathematics *4*, 99-111. 10.3934/Math.2019.1.99.

190. Rouabah, H.A., Park, B.Y., Zaouk, R., Madou, M.J., Morgan, H., and Green, N.G. (2010).

Increasing the fluid flow velocity in a microchannel using 3D non-metallic electrodes. 14th International Conference on Miniaturized Systems for Chemistry and Life Sciences, Groningen, The Netherlands, October 3−7, 2010, EPFL.

191. Shi, H., Qin, J., Lu, P., Dong, C., He, J., Chou, X., Das, P., Wang, J., Zhang, L., and Wu, Z.S. (2021). Interfacial Engineering of Bifunctional Niobium (V)-Based Heterostructure Nanosheet Toward High Efficiency Lean-Electrolyte Lithium–Sulfur Full Batteries. Advanced Functional Materials *31*, 2102314. 10.1002/adfm.202102314.

192. Boyjoo, Y., Shi, H., Olsson, E., Cai, Q., Wu, Z.S., Liu, J., and Lu, G.Q. (2020). Molecular-Level Design of Pyrrhotite Electrocatalyst Decorated Hierarchical Porous Carbon Spheres as Nanoreactors for Lithium–Sulfur Batteries. Advanced Energy Materials *10*, 2000651. 10.1002/aenm.202000651.

193. Boyjoo, Y., Shi, H., Tian, Q., Liu, S., Liang, J., Wu, Z.-S., Jaroniec, M., and Liu, J. (2021). Engineering nanoreactors for metal–chalcogen batteries. Energy & Environmental Science *14*, 540-575. 10.1039/d0ee03316b.

194. Yang, F., Mousavie, S.M.A., Oh, T.K., Yang, T., Lu, Y., Farley, C., Bodnar, R.J., Niu, L., Qiao, R., and Li, Z. (2018). Sodium-Sulfur Flow Battery for Low-Cost Electrical Storage. Advanced Energy Materials *8*, 1701991. 10.1002/aenm.201701991.

195. Wang, Y.X., Zhang, B., Lai, W., Xu, Y., Chou, S.L., Liu, H.K., and Dou, S.X. (2017). Room-Temperature Sodium-Sulfur Batteries: A Comprehensive Review on Research Progress and Cell Chemistry. Advanced Energy Materials *7*, 1602829. 10.1002/aenm.201602829.

196. Zhang, S., Pollard, T.P., Feng, X., Borodin, O., Xu, K., and Li, Z. (2020). Altering the Electrochemical Pathway of Sulfur Chemistry with Oxygen for High Energy Density and Low Shuttling in a Na/S Battery. ACS Energy Letters *5*, 1070-1076. 10.1021/acsenergylett.9b02746.

197. Gallant, B.M., Kwabi, D.G., Mitchell, R.R., Zhou, J., Thompson, C.V., and Shao-Horn, Y. (2013). Influence of Li2O2 morphology on oxygen reduction and evolution kinetics in Li–O2 batteries. Energy & Environmental Science *6*, 2518–2528. 10.1039/c3ee40998h.

198. Wang, Y., Luo, Z., Liu, D., and Li, Y. (2022). Immobilization of mercury in tailings originating from the historical artisanal and small-scale gold mining using sodium

polysulfide. Environmental Science and Pollution Research *29*, 56562-56578. 10.1007/s11356-022-19569-1.

199. Wang, C., Zhang, Y., Zhang, Y., Luo, J., Hu, X., Matios, E., Crane, J., Xu, R., Wang, H., and Li, W. (2021). Stable sodium-sulfur electrochemistry enabled by phosphorus-based complexation. Proceedings of the National Academy of Sciences of the United States of America *118*, e2116184118. 10.1073/pnas.2116184118.

200. Guo, L., Oskam, G., Radisic, A., Hoffmann, P.M., and Searson, P.C. (2011). Island growth in electrodeposition. Journal of Physics D: Applied Physics *44*, 443001. 10.1088/0022-3727/44/44/443001.

201. Yang, J., McCoy, B.J., and Madras, G. (2005). Distribution kinetics of polymer crystallization and the Avrami equation. Journal of Chemical Physics *122*, 064901. 10.1063/1.1844373.

202. A. Bewick, M. Fleischmann, and Thirsk, H.R. (1962). Kinetics of the Electrocrystallization of Thin Films of Calomel. Transactions of the Faraday Society. *58*, 2200. 10.1039/TF9625802200.

203. Allen, S.M., R.W. Balluffi, and W.C. Carter (2005). Kinetics of materials (Wiley-VCH).

204. Fan, F.Y., Carter, W.C., and Chiang, Y.M. (2015). Mechanism and Kinetics of Li2S Precipitation in Lithium-Sulfur Batteries. Advanced Materials *27*, 5203-5209. 10.1002/adma.201501559.

205. Ren, Y.X., Jiang, H.R., Zhao, T.S., Zeng, L., and Xiong, C. (2018). Remedies of capacity fading in room-temperature sodium-sulfur batteries. Journal of Power Sources *396*, 304-313. 10.1016/j.jpowsour.2018.06.056.

206. Ren, Y.X., Zhao, T.S., Liu, M., Tan, P., and Zeng, Y.K. (2016). Modeling of lithium-sulfur batteries incorporating the effect of Li2S precipitation. Journal of Power Sources *336*, 115-125. 10.1016/j.jpowsour.2016.10.063.

207. Carter, R., NewRingeisen, A., Reed, D., Atkinson, R.W., Mukherjee, P.P., and Love, C.T. (2020). Optical Microscopy Reveals the Ambient Sodium–Sulfur Discharge Mechanism. ACS Sustainable Chemistry & Engineering *9*, 92-100. 10.1021/acssuschemeng.0c07180.

208. Thompson, S.D., and Newman, J. (1989). Differential Diffusion Coefficients of Sodium Polysulfide Melts. Journal of The Electrochemical Society *136*, 3362. 10.1149/1.2096451.